

The doping-driven evolution of the superconducting state of a doped Mott insulator: a key for the high temperature superconductivity.

M. Civelli¹

¹ *Theory Group, Institute Laue Langevin, Grenoble, France*

(Dated: February 2, 2022)

High-temperature superconductors at zero doping can be considered strongly correlated two-dimensional Mott insulators. The understanding of the connection between the superconductor and the Mott insulator hits at the heart of the high-temperature superconducting mechanism. In this paper we investigate the zero-temperature doping-driven evolution of a superconductor towards the Mott insulator in a two dimensional electron model, relevant for high temperature superconductivity. To this purpose we use a cluster extension of dynamical mean field theory. Our results show that a standard (BCS) d-wave superconductor, realized at high doping, is driven into the Mott insulator via an intermediate state displaying non-standard physical properties. By restoring the translational invariance of the lattice, we give an interpretation of these findings in momentum space. In particular, we show that at a finite doping a strong momentum-space differentiation takes place: non-Fermi liquid and insulating-like (pseudogap) character rises in some regions (antinodes), while Fermi liquid quasiparticles survive in other regions (nodes) of momentum space. We describe the consequence of these happenings on the spectral properties, stressing in particular the behavior of the superconducting gap, which reveals two distinct nodal and antinodal energy scales as a function of doping. We propose a description of the evolution of the electronic structure while approaching the Mott transition and compare our results with tunneling experiments, photoemission and magnetotransport on cuprate materials.

PACS numbers: 71.10.-w, 71.10.Fd, 74.20.-z, 74.72.-h

I. INTRODUCTION

Since the discovery in 1986 of the high temperature (H-TC) superconductivity in copper oxide based materials¹, much effort has been devoted by the scientific community to understand the physics of this phenomenon, but its key-ingredients remain still unknown. On the experimental side, the complexity of these materials, which present a rich phase diagram with many competing instabilities, has made impossible to perform resolute experiments. On the theoretical side, many theories have been proposed, but a general consensus has not been achieved yet because of the lack of tools capable of perform reliable calculations. The strongly-interacting many-body nature of these systems makes in fact standard techniques hardly applicable. The recent discovery of high-temperature superconductivity in a new family of materials² (for a perspective see e.g. ref.³), with a general composition $\text{LaFeAsO}_{1-x}\text{F}_x$, different from the typical Cu-O plane structure of all known H-TC compounds, has revitalized the attention on the origin of the H-TC mechanism.

In early times, P.W. Anderson⁴ suggested that H-TC superconductivity is the result of doping a Mott insulator with a small number of carriers. The understanding of the way a superconductor can transform into a Mott insulator has been a longstanding open problem and its connection with a strongly-interacting superconductivity has been long sought. The aim of this article is to investigate the doping-driven evolution of the superconducting state of a doped Mott insulator in a two dimensional lattice model of strongly correlated electrons. To this purpose we employ a cluster extension of Dynamical Mean

Field Theory (DMFT) (for a review see ref.⁵).

1. *Dynamical Mean Field Theory and its Cluster extensions to study H-TC superconductivity*

DMFT has in recent years proved very successful in revealing the physics of the Mott transition in three dimensional compounds, like e.g. Vanadium Oxide. DMFT is a self-consistent mean field method, which maps a lattice problem onto a single-impurity embedded in a bath of free electrons. It is exact in the limit of infinite dimension, where the physics is purely local and DMFT virtually provides the complete solution. Its strength stands in the ability of treating on the same footing high and low energy physics, capturing in one framework both the Mott insulating state as well as the metallic state, and hence allowing a non-perturbative investigations. A good summary of the physics captured by DMFT is described in the DMFT phase diagram. For example, single-site DMFT in conjunction with electronic structure methods has provided results in excellent agreement with experiments on numerous three dimensional compounds (with valence electrons in the sp shell⁶, 3d shell, 4d shell⁷, 4f shell^{8,9} and 5f shell¹⁰). For some recent reviews of this field see e.g. ref.¹¹.

In spite of these successes in genuine strongly correlated materials, DMFT has also well understood limitations, mainly due to its purely local character. It does not capture for example the feedback of collective modes, such as magnetic fluctuations on the single particle quantities. One consequence of this shortcoming is that the effective mass diverges as the Mott transition is

approached, while in finite dimensions exchange effects should remove this enhancement in the region where the renormalized kinetic energy is of the order of the super-exchange-interaction or the temperature. These effects are negligible whenever strong frustration, finite temperature or orbital degeneracy help justifying a local approximation. The DMFT approach, however, breaks down in the cuprate-based superconductors, whose physics is two-dimensional and which have a large super-exchange. As the Mott transition is approached in fact, experimental evidence shows that the effective mass remains finite and that physical properties are strongly momentum dependent (see for example Angle Resolved Photoemission Spectroscopy ARPES results^{12,13}). Being a local theory, DMFT is not able by construction to describe a strong momentum dependence, hence it is not suitable to study real finite-dimensional H-TC superconductors.

Recently, extensions of DMFT capable to go beyond the local approximation have been developed. For a review of different cluster extensions of DMFT see e.g. ref.^{14,15,16,17,18}. The Cellular Dynamical Mean Field Theory (CDMFT¹⁹) is a cluster method which retains the real space interpretation of single-site DMFT but incorporates non-perturbative momentum-dependence. It replaces the single site of DMFT by a cluster of impurities, offering the possibility of well describing short-ranged spatial correlation and providing a first correction to momentum-dependent properties. It also allows to naturally describe phases characterized by a spatially dependent order parameter, like for example antiferromagnetism (AF) or d-wave superconductivity (dSC). The first cluster-DMFT studies of the Hubbard model in two dimensions were carried out on a 2×2 plaquette in ref.^{16,17}. These groups have shown the existence of antiferromagnetism, pseudogap and superconductivity, focusing on relatively small values of the on-site interaction (mostly $U = 4t$), for which the Fye-Hirsch Quantum Monte Carlo (QMC)^{20,21} method is applicable in implementing the cluster DMFT. One school of thought, for example in ref.^{22,23,24}, advocates the study of large clusters, at present possible for relatively small interactions. In this latter case, however, it is not yet known what aspects of the Mott physics are captured. Cluster DMFT implemented on the 2×2 plaquette for stronger values of U (the Mott regime) were the subject of several publications^{25,26,27,28} on the Hubbard Model.

2. A 2×2 plaquette Cellular DMFT study

Following the cluster DMFT studies mentioned above, we focus in this paper on a two-dimensional 2×2 cluster-plaquette. According to our viewpoint, elucidating the physical content of the mean field theory on a plaquette is a very important step to accomplish before proceeding to realistic studies of the actual instabilities that govern the phase diagram of the model. The work in references^{29,30,31,32} on small clusters have in fact shown

that there are several competing phases and possible phase-separation, which could lead to complicate patterns in real space depending on the boundary conditions or on various terms not explicitly included in the Hamiltonian. A proper investigation of those states in the framework of DMFT-based methods, requires therefore an understanding of the pure phases of the simple cluster-plaquette.

Implementation of CDMFT on a 2×2 plaquette for large values of the interaction has already revealed several interesting effects not present in single-site DMFT, indicative of a very rich physics. For example, publications^{25,26} reveal that the approach to the Mott transition as a function of doping occur in a very anisotropic way in momentum space. In the Hubbard model (relevant for the description of hole-doped cuprates), the spectral weight disappears much more rapidly in the antinodal than in the nodal region of momentum space, where quasiparticles survive close to the Mott transition at a fixed temperature. Evidence for the formation of a pseudogap in the one electron spectra can be seen in other cluster-DMFT studies^{32,33,34}. CDMFT allows a natural interpolation of the nodal and antinodal spectral function, and it opens the way to study the k -dependence of the one-electron spectra in the Mott insulator²⁷. The origin of the pseudogap can be traced to the growth of the self energy in certain parts of k -space, where eventually at zero temperature lines of poles of the self-energy (i.e. zeroes of the one-particle Green's function) appear^{35,36,37}. In this latter case, the Fermi arcs observed in ARPES are interpreted as the result of a binding of segments of Fermi surface and of a lines of zeros of the Green's function. Results along those lines beyond mean field theory can be found in ref.³⁸. Within CDMFT not only the under-doped regime is anomalous. At optimal doping, where the maximum of the critical temperature occurs, a maximum in the one electron scattering rate and the presence of power laws in the optical conductivity are found³⁹.

In this paper we study the superconducting state which arises upon doping a Mott insulator by implementing the 2×2 plaquette CDMFT with exact diagonalization⁴⁰ (ED-CDMFT) at zero temperature (Lanczos method). Our work is complementary to the 2×2 plaquette CDMFT study of ref.⁴¹, where the continuous time quantum Monte Carlo (CTQMC) at finite temperature was used as impurity solver. As compared with QMC methods, ED allows to extract in an unbiased way real frequency quantities, which can be more easily physically interpreted. This will turn out to be fundamental in interpreting our CDMFT results and making important connection with experiments (as we will widely present throughout the paper). The Lanczos method, on the other hand, is limited by the finite size of the system used to describe an effective impurity model, associated with the original lattice model (see the following discussion on the ED-CDMFT procedure). If rightly implemented, however, it is able to well capture the difficult physics of

the finite dimensional Mott transition (see for example references^{11,42,43}). We will in fact show that the physics described by our results well compares (at least at the qualitative level) with the CTQMC-CDMFT results of reference⁴¹, where finite size limitations are absent.

Earlier studies²⁸ with ED-CDMFT have compared the phase diagram of the two dimensional Hubbard Model with the one of cuprate-based materials, studying the interplay between the superconducting and antiferromagnetic instabilities, either in the hole and electron doped sides. Here we complete the work presented in a previous short publication⁴⁴, and we focus on doping-driven evolution of the superconductor towards the Mott insulator. In particular we show that, in a small region around optimal doping, novel properties appear in the superconducting state which are not ascribable to the standard Bardeen Cooper Schrieffer (BCS) theory of superconductivity. The most striking phenomenon, as widely presented in publication⁴⁴, is the rising of two distinct doping-dependent energy scales, which do not fit neither into the framework of BCS approaches nor within the most popular theories of H-TC superconductivity, like for instance the resonating valence bond theories (RVB⁴, for a recent review see e.g.⁴⁵). We interpret our cluster results extracting the momentum-dependence (i.e. restoring the translational invariance of the lattice) of the electronic structure as a function of doping. According to our physical picture, the Fermi liquid description holds at low energies in the nodal region of momentum space, where the d-wave superconducting gap is zero. We show that this fact is best described in momentum space introducing a periodizing scheme based on the local (within cluster) self-energy^{25,46}. On the other hand, in the antinodal region, where the d-wave gap is maximal, besides the superconducting contribution, a further contribution to the one-particle gap appears also in the normal component at the finite critical doping. In this case we show that the periodization of another local quantity, the irreducible two-point cumulant, offers a more adequate description^{36,47}. We introduce therefore a mixed-periodization scheme, which was foreshadowed in a phenomenological approach to the transport properties of cuprate materials in the normal state⁴⁸ and in a previous CDMFT publication⁴⁴, and confront the resulting picture of the electronic evolution as a function doping with photo-emission, scanning tunneling experiments and magnetotransport on cuprate materials.

3. Set-up of the paper

The paper consists of two main parts. The first comprises sections I-IV. In section I, after this introduction, we present the model and briefly explain the ED-CDMFT method. In section II we present the raw cluster DMFT results, mainly stressing their evolution with doping and showing the appearance (at small doping) of two distinct energy scales. It is not however straightforward to inter-

pret these cluster quantities in terms of physical observables. Therefore, in section III, we cope with the problem of extracting lattice quantities (which can be more easily compared with experimental results) from the corresponding cluster ones, i.e. we present and justify different periodization-methods. We show that nodal and antinodal regions of momentum space turn out having different physical properties which require different periodization schemes to be rightly described. In section IV we characterize the different properties in the nodal and antinodal regions, according to the periodization schemes introduced, clearly linking them with spectroscopy experiments.

The second part starts from section V, where, in order to be able to compare our results with experiments resolved in momentum space, we introduce a more general mixed-periodization scheme. This latter, interlacing the nodal and antinodal properties in all the momentum space, allows us to propose a description of the evolution of quasiparticle spectra in approaching the Mott transition. Spectra, which are directly comparable with photo-emission on the cuprates, are presented in detail in section VI. In section VII we present peculiar characteristics of the spectra, the so called "kink" feature, also comparing with photoemission results. Finally, in section VIII, by applying a phenomenological Boltzmann approach on our CDMFT mixed-periodization result, we derive the Hall resistivity, which is a direct probe of the charge carries in the system. We compare its evolution as a function of doping with magnetotransport experiments and draw conclusions on a topological phase transition of the Fermi surface, which takes place at low doping within the mixed-periodization scheme introduced in section V. We finally derive our conclusions in section IX.

A. The Model

We consider the one-band two dimensional Hubbard Model on a square lattice:

$$\mathcal{H} = - \sum_{\langle i,j \rangle, \sigma} t_{ij} (c_{i,\sigma}^\dagger c_{j,\sigma} + h.c.) + U \sum_i n_{i\uparrow} n_{i\downarrow} - \mu \sum_i n_i, \quad (1)$$

which is universally considered a minimal description of cuprate-based materials⁴⁹. Here $c_{i,\sigma}$ ($c_{i,\sigma}^\dagger$) are destruction (creation) operators for electrons of spin σ , $n_{i\sigma} = c_{i\sigma}^\dagger c_{i\sigma}$ is the density of electrons, μ is the chemical potential tuning doping and t_{ij} are the orbital hopping integrals. For convenience's sake we consider only the nearest neighbor amplitude $t = 1$, and a next nearest neighbor hopping $t' = -0.3t$. We set the on-site repulsion $U = 12t$, larger than the band-width $8t$, to be in the Mott regime.

B. ED-CDMFT procedure

Similarly to single-site DMFT⁵, in CDMFT the original model (eq. 1) is described in terms of an effective action containing a Weiss dynamical field $\hat{\mathcal{G}}_0(\tau)$ describing the degrees of freedom outside the cluster (in the bath) as a time dependent hopping within the cluster

$$S_{\text{eff}} = \int_0^\beta d\tau d\tau' \Psi_\tau^\dagger \left[\hat{\mathcal{G}}_{0\tau-\tau'}^{-1} \right] \Psi_{\tau'} + U \sum_\mu \int_0^\beta n_{\mu\uparrow} n_{\mu\downarrow} d\tau. \quad (2)$$

$\mu = 1 \dots N_c$ ($N_c = 4$ in the 2×2 plaquette) labels the degrees of freedom inside the cluster. For the case of a 2×2 plaquette considered in this paper, a convenient Nambu-spinor notation has been introduced:

$$\Psi^\dagger \equiv (c_{1\uparrow}^\dagger, \dots, c_{4\uparrow}^\dagger, c_{1\downarrow}, \dots, c_{4\downarrow}) \quad (3)$$

With this notation the Weiss field $\hat{\mathcal{G}}_0$ is a 8×8 matrix with both normal (particle-hole) and anomalous (particle-particle) components²⁸. Physically, this action describes a cluster embedded in a self-consistent bath of free electrons with dSC correlations. In the CDMFT procedure, a starting guess of the Weiss field $\hat{\mathcal{G}}_0$ is given as input. Then the cluster single-particle propagator \hat{G}_c is computed through the effective action eq. (2) and the cluster self-energy is determined through the Dyson's equation

$$\hat{\Sigma}_c = \hat{\mathcal{G}}_0^{-1} - \hat{G}_c^{-1} \quad (4)$$

Here,

$$\hat{G}_c(\tau, \tau') = \begin{pmatrix} \hat{G}_\uparrow(\tau, \tau') & \hat{F}(\tau, \tau') \\ \hat{F}^\dagger(\tau, \tau') & -\hat{G}_\downarrow(\tau', \tau) \end{pmatrix} \quad (5)$$

is an 8×8 matrix, $G_{\mu\nu, \sigma} \equiv \langle -T c_{\mu\sigma}(\tau) c_{\nu\sigma}^\dagger(0) \rangle$ and $F_{\mu\nu} \equiv \langle -T c_{\mu\downarrow}(\tau) c_{\nu\uparrow}(0) \rangle$, ($\mu, \nu = 1 \dots N_c$ label sites of the cluster) are the normal and anomalous cluster-Green's functions respectively. From the cluster self-energy $\hat{\Sigma}_c$, we use the CDMFT self-consistency condition to re-compute the local cluster Green's function $\hat{G}_{loc}(i\omega_n) = \sum_K \hat{G}(K, i\omega_n)$, where

$$\hat{G}(K, i\omega_n) = \left[i\omega_n + \mu - \hat{t}(K) - \hat{\Sigma}_c(i\omega_n) \right]^{-1} \quad (6)$$

In eq.(6) $\hat{t}(K)$ is the Fourier transform of the hopping matrix defined on the lattice formed by the clusters and the sum over K is therefore performed over the Brillouin zone reduced by the partition in clusters of the lattice⁵⁰. We finally re-derive a new Weiss field

$$\hat{\mathcal{G}}_0^{new}(i\omega_n)^{-1} = \hat{G}_{loc}^{-1}(i\omega_n) + \hat{\Sigma}_c(i\omega_n) \quad (7)$$

and iterate until convergence is reached.

In practice, as we mentioned in the introduction, in order to solve the cluster impurity problem, in this work (as in ref.^{28,44}) we use the Exact Diagonalization method⁴⁰. A

parametrized Anderson-impurity Hamiltonian describes the action eq.(2) and couples the cluster impurity with a discrete number N_b of bath orbitals (we have fix throughout this work $N_b = 8$, which is the limit in practice accessible with standard computational resources) :

$$\begin{aligned} \mathcal{H}_{\text{imp}} = & \sum_{\mu\nu\sigma} E_{\mu\nu\sigma} c_{\mu\sigma}^\dagger c_{\nu\sigma} + U \sum_\mu n_{\mu\uparrow} n_{\mu\downarrow} + \\ & + \sum_{k\sigma} \epsilon_{k\sigma} a_{k\sigma}^\dagger a_{k\sigma} + \sum_{k\mu\sigma} V_{k\mu\sigma} a_{k\sigma}^\dagger c_{\mu\sigma} + \text{h.c.} + \\ & + \sum_{k\mu\sigma} V_{k\mu\sigma}^{\text{sup}} a_{k\sigma}^\dagger c_{\mu\bar{\sigma}}^\dagger + \sum_{k\mu\sigma} V_{k\mu\sigma}^{\text{sup}} c_{\mu\bar{\sigma}} a_{k\sigma} \end{aligned} \quad (8)$$

Here $E_{\mu\nu\sigma} = -\mu\delta_{\mu\nu}$, $E_{\mu\nu\sigma} = -t\delta_{\mu, \nu \pm 1}$. Under the self-consistency constrain eq.(6) and (7), the bath-parameters $\epsilon_{k\sigma}$, $V_{k\mu\sigma}$ and $V_{k\mu\sigma}^{\text{sup}}$ are determined at each CDMFT-iteration by fitting the Anderson-impurity Weiss field (eq. 7) with a N_b -pole bath function $\hat{\mathcal{G}}_{N_b}^{new}(i\omega_n) = i\mathbf{1}\omega - \hat{E} - \hat{\Delta}$

$$\hat{\Delta} = \sum_k^{N_b} \mathbf{V}_k^\dagger (i\mathbf{1}\omega - \hat{\epsilon}_k)^{-1} \mathbf{V}_k \quad (9)$$

$$\mathbf{V}_k(2 \times 8) = \begin{pmatrix} V_{k\mu\uparrow} & V_{k\mu\uparrow}^{\text{sup}} \\ -V_{k\mu\downarrow}^{\text{sup}} & -V_{k\mu\downarrow} \end{pmatrix}_{\mu=1, N_c} \quad (10)$$

$$\mathbf{E}_k(2 \times 2) = \begin{pmatrix} \epsilon_{k\uparrow} & 0 \\ 0 & -\epsilon_{k\downarrow} \end{pmatrix} \quad (11)$$

The fitting is obtained via a conjugate gradient minimization algorithm, which uses a distance function⁴²

$$f = \sum_{\mu\nu} \left| \hat{\mathcal{G}}_0^{new}(i\omega_n) - \hat{\mathcal{G}}_{N_b}^{new}(i\omega_n) \right|_{\mu\nu} / \omega_n \quad (12)$$

that emphasizes the lowest frequencies and it is computed on the imaginary frequency axis $\omega_n = (2n-1)\pi/\beta$. This introduces an effective inverse temperature, which is a fitting parameter (it is not the real temperature which is $T = 0$ in our study) and is set $\beta = 300t$ (much higher than the $\beta = 50t$ used in publication of ref.²⁸) throughout the whole paper. This parameter determines the energy resolution accessed in this work (see also appendix A). On a practical level, to start the ED-CDMFT procedure it is most useful to introduce a reduced parameterization of the bath, which enlightens the symmetries of the input-guess $\hat{\mathcal{G}}_0(i\omega_n)$. The constrain on the bath parameters can be then relaxed in a second step. Further details are given in appendix B.

II. CLUSTER RESULTS

We start this section by considering raw cluster quantities, which directly output from the cluster-impurity solution.

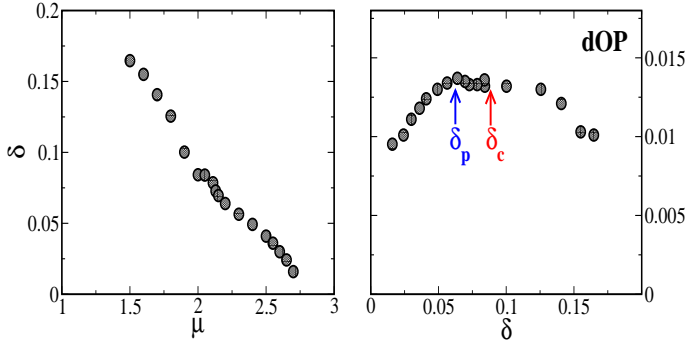


FIG. 1: (Color online). Left panel: doping $\delta = 1 - \langle n \rangle$ versus chemical potential μ . Right panel: cluster d-wave order parameter $\text{dOP} = \langle\langle c_{\mu\uparrow}c_{\mu+1\downarrow} \rangle\rangle_{(\tau=0)}$ as a function of doping δ .

A. A d-wave Superconducting state

As we explained above, within CDMFT a superconducting state can be studied by allowing particle-particle pairing terms $V_{k\mu\sigma}^{\text{sup}} a_{k\uparrow} c_{q\downarrow}$ in the impurity Hamiltonian eq.(8) (or equivalently upon a unitary rotation, pairing bath terms $a_{\mu\uparrow} a_{k\downarrow}$, see Appendix B). CDMFT-self-consistency condition may accept non-zero values of the $V_{k\mu\sigma}^{\text{sup}}$ terms, resulting in a non-zero superconducting-pair Green's function $F_{\mu,\nu}(\tau) = T_\tau \langle c_{\mu\uparrow}(\tau) c_{\nu\downarrow} \rangle$. In drawing a parallel with the classical mean field example of the Ising Model⁵, this is equivalent to assume a non-zero on-site magnetization $m = \langle S_i^z \rangle$ as starting hypothesis in building an effective Hamiltonian, and to determine then m self-consistently. As reported in previous work²⁸, CDMFT supports indeed a d-wave superconducting state in a region of doping that precedes the Mott transition. This is shown in Fig. 1, where we show the doping $\delta = 1 - \langle n_i \rangle$ versus the chemical potential μ and the d-wave order parameter (dOP), defined as $F_{\mu,\mu\pm 1}(\tau = 0)$, also as a function of δ . As expected, δ versus μ is monotonically decreasing. The dOP has a dome-like shape and its sign is alternating by exchange of the x - y bonds on the cluster plaquette. We can locate the maximum only with some degree of uncertainty around $\delta_p \sim 0.06 < \delta < \delta_c \sim 0.08$. The two doping values $\delta_p \sim 0.06$ and $\delta_c \sim 0.08$ present as two special points, which mark changes in the physical properties of the system. We will come back on these two points in throughout the paper. Here we stress that at δ_c in particular, our dynamical mean field result seems to branch two different lines of solution. This is evident either in the $\delta - \mu$ and the dOP plots. In mean field approaches this behavior may be the signature of a phase transition. It is therefore intriguing that we find such a behavior close to the maximum of the dOP dome.

Following the nomenclature typical for cuprate materials, we will call hereafter the region $\delta < \delta_p$ under-doped, $\delta > \delta_c$ over-doped and $\delta_p \sim 0.06 < \delta < \delta_c \sim 0.08$

optimal doping region. It is clear we do not intend to draw a quantitative parallel with cuprate-based system, where the typical optimal doping (unambiguously defined as the maximum of critical temperature T_C) is around $\delta_c \sim 0.15$, but we rather follow the qualitative aspects of the physics of these material, marking a correspondences with our CDMFT results on the Hubbard Model in two dimensions.

B. Cluster self-energies

It is worth to investigate in detail the cluster-outputs. The typical output of the CDMFT-scheme is a cluster-self-energy $\Sigma_{\mu\nu}$ (eq. 4), which can be expressed as a $2 \times N_c \times N_c$ ($N_c = 4$ for the 2×2 plaquette) matrix with normal and anomalous components in the Nambu notation introduced in eq. (3). We first look at the normal components, which are shown on the Matsubara-frequency axis in Fig. 2. The real parts are displayed on the left

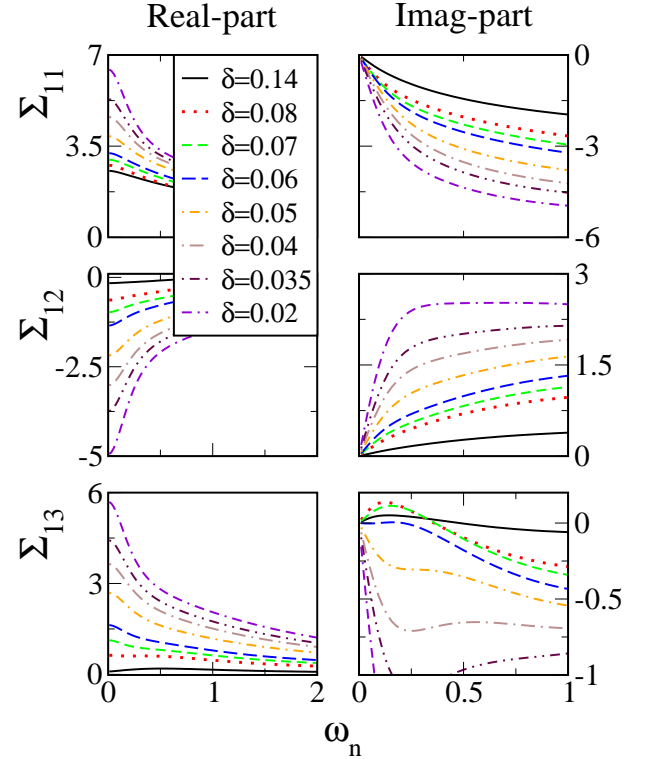


FIG. 2: (Color online). Normal components of the cluster self-energy $\Sigma_{\mu\nu}$ vs the Matsubara frequency ω_n as a function of doping δ . In the left column the real parts are displayed, in the right column the imaginary parts. From the top row to the bottom we show the local Σ_{11} , the next neighbor Σ_{12} , and nearest next neighbor Σ_{13} self-energies.

and the imaginary parts on the right column from high (in our solution) doping $\delta = 0.14$ (the over-doped side) until close to the Mott transition for $\delta = 0.02$ (in the under-doped side). From the top row to the bottom we

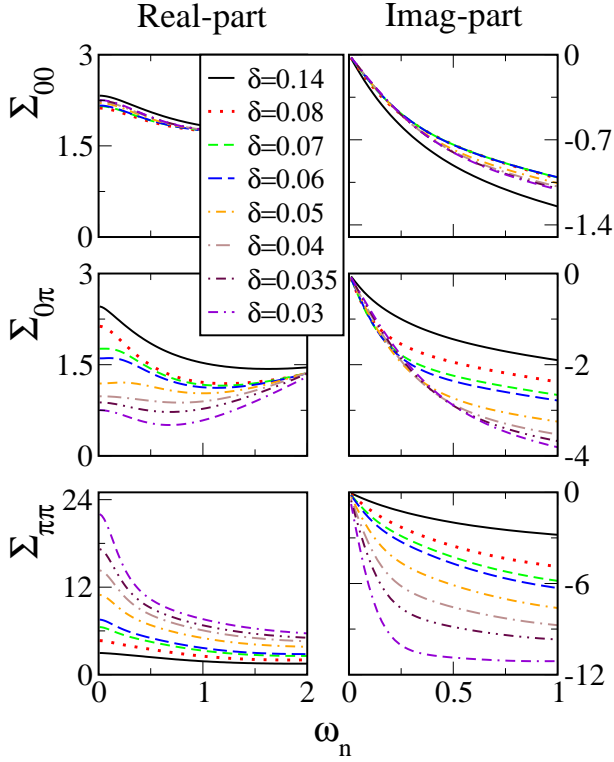


FIG. 3: (Color online). Eigenvalues of the normal component of the cluster self-energy $\Sigma_{\mu\nu}$ vs the Matsubara frequency ω_n as a function of doping δ . In the left column the real parts are displayed, in the right column the imaginary parts. From the top row to the bottom we show the self-energy corresponding to the points $k = (0, 0)$, $(0, \pi)$ and (π, π) in the first quadrant of the Brillouin Zone (see section III).

have the local self-energy Σ_{11} , the next neighbor Σ_{12} and the nearest next neighbor Σ_{13} . At high doping, the local components is dominant. We expect in this region that the single site DMFT is already a good approximation. By decreasing δ , however, also the non-local components Σ_{12} and Σ_{13} grow considerably, becoming comparable with the local one. This effect is totally missed by single site DMFT and it is only captured by using a cluster extension. The growing of the non local components of $\Sigma_{\mu\nu}$ determines the physical properties of the system in approaching the Mott transition in a fundamental way, as we explain in the following. The imaginary parts (right column) display a low-energy Fermi-liquid-like behaviour $\text{Im}\Sigma \sim \alpha\omega_n$. The slope α is connected with the quasiparticle residuum (see the following). Here we notice that, with respect to the other components, the energy range of linear behavior in the nearest next neighbor $\text{Im}\Sigma_{13}$ is narrower and that its slope α also changes behavior in passing through the doping $\delta_c \sim 0.08$ (it grows for $\delta < \delta_c$, decreases until becoming negative for $\delta > \delta_c$), while it also changes sign at $\delta_c \sim 0.06$. This behavior is the only mark we find in the cluster self-energy of the special nature of the points δ_c and δ_p that we identified

in the Fig. 1. The local and next neighbor components show instead a smooth continuous behavior as a function of doping δ .

As in ref.^{26,47}, it is convenient to look at the eigenvalues of the cluster-self-energy matrix, which can be directly related to the corner points of the quadrant of the Brillouin Zone (as we will explain in more detail in the following section). A convenient way is to re-express the Nambu-spinor notation eq.(3) by grouping two by two the up and down spin construction/destruction operators on each cluster-site:

$$\Psi^\dagger \equiv [(c_{1\uparrow}^\dagger, c_{1\downarrow}) \dots, (c_{4\uparrow}^\dagger, c_{4\downarrow})] \quad (13)$$

The cluster self-energy matrix assumes the form:

$$\Sigma_c = \begin{pmatrix} \hat{\Sigma}_0 & \hat{\Sigma}_{1x} & \hat{\Sigma}_2 & \hat{\Sigma}_{1y} \\ \hat{\Sigma}_{1x} & \hat{\Sigma}_0 & \hat{\Sigma}_{1y} & \hat{\Sigma}_2 \\ \hat{\Sigma}_2 & \hat{\Sigma}_{1y} & \hat{\Sigma}_0 & \hat{\Sigma}_{1x} \\ \hat{\Sigma}_{1y} & \hat{\Sigma}_2 & \hat{\Sigma}_{1x} & \hat{\Sigma}_0 \end{pmatrix} \quad (14)$$

where the 2×2 matrices are function of cluster elements $\Sigma_{\mu\nu, \sigma} = \Sigma_{|\mu-\nu|, \sigma}$:

$$\begin{aligned} \hat{\Sigma}_0 &= \begin{pmatrix} \Sigma_{0\uparrow} & 0 \\ 0 & -\Sigma_{0\downarrow} \end{pmatrix} & \hat{\Sigma}_{1x} &= \begin{pmatrix} \Sigma_{1\uparrow} & \Sigma_{ano} \\ \Sigma_{ano} & -\Sigma_{1\downarrow} \end{pmatrix} \\ \hat{\Sigma}_2 &= \begin{pmatrix} \Sigma_{2\uparrow} & 0 \\ 0 & -\Sigma_{2\downarrow} \end{pmatrix} & \hat{\Sigma}_{1y} &= \begin{pmatrix} \Sigma_{1\uparrow} & -\Sigma_{ano} \\ -\Sigma_{ano} & -\Sigma_{1\downarrow} \end{pmatrix} \end{aligned} \quad (15)$$

We follow the procedure used to diagonalize the cluster-self-energy matrix in ref.⁵¹:

$$\Sigma_c = \begin{pmatrix} \hat{\Sigma}_{00} & 0 & 0 & 0 \\ 0 & \hat{\Sigma}_{\pi\pi} & 0 & 0 \\ 0 & 0 & \hat{\Sigma}_{0\pi} & 0 \\ 0 & 0 & 0 & \hat{\Sigma}_{\pi 0} \end{pmatrix} \quad (16)$$

The diagonal elements are linear combination of the original cluster self-energies matrices:

$$\begin{aligned} \hat{\Sigma}_{00} &= \hat{\Sigma}_0 + \tilde{\Sigma}_1 + \tilde{\Sigma}_2 \\ \hat{\Sigma}_{0\pi} &= \hat{\Sigma}_0 + \tilde{\Sigma}_a - \tilde{\Sigma}_2 \\ \hat{\Sigma}_{\pi 0} &= \hat{\Sigma}_0 - \tilde{\Sigma}_a - \tilde{\Sigma}_2 \\ \hat{\Sigma}_{\pi\pi} &= \hat{\Sigma}_0 - \tilde{\Sigma}_1 - \tilde{\Sigma}_2 \end{aligned} \quad (17)$$

For convenience's sake we have defined :

$$\tilde{\Sigma}_1 = 2 \begin{pmatrix} \Sigma_{1\uparrow} & 0 \\ 0 & -\Sigma_{1\downarrow} \end{pmatrix} \quad \tilde{\Sigma}_a = 2 \begin{pmatrix} 0 & \Sigma_{ano} \\ \Sigma_{ano} & 0 \end{pmatrix} \quad (18)$$

Notice that from eq. (17) the anomalous self-energy appears only in the $(0, \pi)$ and $(\pi, 0)$ components, where the dSC gap is expected to open. The 2×2 eigenvalue-matrices of the cluster-self-energy are interpreted as describing the four momentum-space points $(0, 0)$, $(0, \pi)$, $(\pi, 0)$ and (π, π) (hence the choice of the labels), as we will explain in detail in the following section III.

The normal components of the eigenvalues of $\hat{\Sigma}_c$ are shown in Fig. 3, in a fashion similar to Fig. 2. The

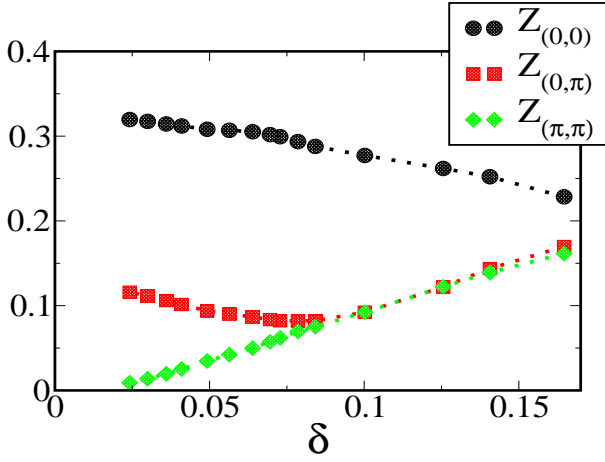


FIG. 4: (Color online). Cluster quasiparticle residua, associated with the eigenvalues of the cluster self-energy matrix, as a function of doping δ .

first striking difference with respect to the Fig. 2 is that the eigenvalue Σ_{00} changes little as a function of doping (either the real and the imaginary parts). $\Sigma_{0\pi}$ and $\Sigma_{\pi\pi}$ both grow in reducing doping δ , but the growth in $\Sigma_{\pi\pi}$ is on order of magnitude bigger. This eigenvalue is indeed the one that drives the system into the Mott insulating state as $\delta \rightarrow 0$, as evident from the big values of both the real part and of the slope of the imaginary part at small doping. This behavior are very similar (i.e. it appears as a smooth continuation) to the one displayed by the self-energy of the normal state ED-CDMFT study published in ref.²⁶. With respect to this latter study however, here we display the *normal components of a superconducting solution* (while in ref.²⁶ no superconductivity is allowed) and the energy resolution achieved ($\beta t = 300$) is an order of magnitude smaller than in ref.²⁶ ($\beta t = 32$). This allows us to extract the very low-energy properties. In particular, as expected by the fact that Σ has to be negative in order to respect causality, we can observe in Fig. 3 that the slope α of the $\text{Im}\Sigma \sim \alpha\omega_n$ is always negative. The fact then the $\omega_n \rightarrow 0$ behavior of $\text{Im}\Sigma$ is linear indicates that these eigenvalues components have Fermi liquid properties. Following a standard Fermi liquid approach, it is instructive to define cluster quasiparticle residua $Z_X = (1 - \partial\Sigma_X/\partial\omega_n)$ with $X = (0,0), (0,\pi), (\pi,\pi)$, even if these quantities have a real physical meaning only in correspondence of a real Fermi surface (i.e. Z_X has to be interpreted here as renormalized cluster quantity). In the standard picture of the Mott transition⁵, the quasiparticle residuum $Z \rightarrow 0$ as doping is reduced $\delta \rightarrow 0$. From Fig. 4 we see that only $Z_{(\pi,\pi)}$ appears to display this behavior, while $Z_{(0,0)}$ and $Z_{(0,\pi)}$ clearly extrapolate to a non-zero value. A last remark concerns once again the special critical doping δ_c , where remarkably the $Z_{(0,\pi)}$ shows a clear change in behavior. For $\delta > \delta_c$ it closely follows $Z_{(\pi,\pi)}$, decreasing with doping as expected in the standard Mott transi-

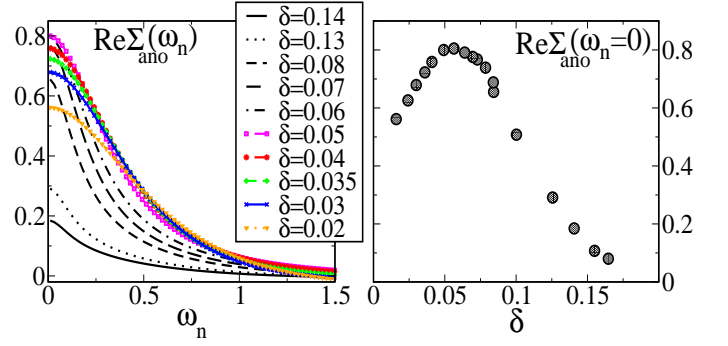


FIG. 5: (Color online). Left panel: real part of the anomalous component of the cluster-self-energy Σ_{ano} (the imaginary part is negligible) vs Matsubara frequency ω_n for different doping δ . Right panel: $\text{Re}\Sigma_{ano}(\omega_n \rightarrow 0)$ versus doping δ .

tion picture. At δ_c , however, $Z_{(0,\pi)}$ departs from $Z_{(\pi,\pi)}$, and shows a behavior more similarly to $Z_{(0,0)}$. This once again indicates a quick change in the physical properties of the system in correspondence of δ_c . We will come back later to discussing the physical interpretation of these observations on the cluster quasiparticle residua (see section IV).

We now turn to the anomalous component of $\hat{\Sigma}_c$, which we show in the left side of Fig. 5 on the Matsubara frequency ω_n . As resulting output of our CDMFT solution, only the real part of the nearest-neighbor component is appreciably non-zero on the Matsubara axis, and it assumes a d-wave sign bond-alternating value on the cluster-plaquette. $\text{Re}\Sigma_{ano}$ starts assuming appreciably non-zero values in the over-doped side $\delta = 0.14$, and grows for decreasing doping, until $\delta_c \sim 0.08$ is reached. In the under-doped side however at $\delta < \delta_p \sim 0.06$ the curves change tendency, and they decrease by further decreasing doping. The qualitative change in the behavior is better enlightened by looking at the $\omega \rightarrow 0$ limit: in the under-doped side the curves reach $\omega = 0$ with a finite slope, while in the under-doped side (after $\delta \leq 0.08$) the slope has a smaller value. In right side of Fig. 5 we show the $\omega_n \rightarrow 0$ extrapolated value of $\text{Re}\Sigma_{ano}$ as a function of doping δ . In first approximation this value can be related to the superconducting gap (as we will explain in detail in the section III, see eq. 30). The behavior of the $\text{Re}\Sigma_{ano}$ as a function of doping shows therefore to be non-monotonic and roughly tracks the behavior of the order parameter (see Fig. 1), similarly to standard BCS theory. This result is fundamental and it is in striking contrast with slave-boson resonating valence bond theories^{4,45,52}, where the amplitude associated to a particle-particle pairing channel is a monotonically decreasing function with doping and it has its maximum close to the insulating transition. In section IV we will better discuss the physical consequences of these results, making connection with recent spectroscopy experiments on cuprate-based materials.

With the ED-CDMFT procedure it is straightforward to analytically continue on the real axis⁵ (differently from other computational methods like e.g. Quantum Monte Carlo, which require further approximate methods). The cluster Green's function $\mathbf{G}_c(\omega_n)$ and the cluster self-energy $\Sigma_c(\omega_n)$ (via the Dyson's equation 4), are expressed in a pole expansion form containing terms of the form $b/(\omega_n - a)$. To go from the Matsubara to the real axis it is then enough to substitute $i\omega_n \rightarrow \omega + i\eta$, where η is a small broadening introduced to display poles (for more details see appendix A). The price to pay comes from the discreteness introduced by truncating the bath in the impurity model (eq. 8) with a finite number N_b of orbitals. This reproduces continuous functions, like $\mathbf{G}_c(\omega_n)$ and $\Sigma_c(\omega_n)$, through a finite number of poles.

In Fig. 6 we display on the real axes the local density of states $N(\omega) = \frac{1}{\pi} [G_c(\omega)]_{11}$, obtained from the cluster-impurity output (see eq. 4), for different doping δ (from top to bottom), using a small imaginary broadening $i\eta = 7i \times 10^{-3}$. As we will explain in detail in the following section, in a d-wave superconducting state a linear in ω "V" shaped density of states is expected for $\omega \rightarrow 0$. This behavior cannot be captured by the discreteness of our ED-CDMFT solution for small ω , hence we have rather a "U" shape for $\omega \rightarrow 0$ given by the broadening η . The shape of $N(\omega)$ and the energy scales of the superconducting gap can however be estimated by the location and intensities of the peaks. So, in looking at $N(\omega)$ from the over-doped side (top row, left panel for $\delta = 0.16$) to the under-doped side (bottom row, left panel for $\delta = 0.02$) of the phase diagram, we can make interesting observations:

1. $N(\omega)$ is asymmetric function around $\omega = 0$ at low doping ($\delta < \delta_c$). A rather symmetric shape is instead observed around optimal doping $\delta_c \sim 0.08 > \delta > \delta \sim 0.06$ (in agreement with previous cluster DMFT results of ref.⁴¹).
2. the total superconducting gap, which can be evaluated by measuring the distance of the spectral peaks from $\omega = 0$, is increasing by reducing doping δ .

To better elucidate these observations, we have measured the distance from the Fermi level of the left (red circle) and right peaks (green square), and displayed them as a function of doping δ (bottom row, right panel). In the over-doped side ($\delta > \delta_c$) the peaks are equally distant from $\omega = 0$, i.e. the superconducting d-wave gap is symmetric at low frequency, as expected in a standard d-wave BCS theory. At optimal doping $\delta_p < \delta < \delta_c$, however, the asymmetry in the gap strikes in, and it is present in all the under-doped side. This is in agreement with the cluster DMFT results obtained in ref.⁴¹ and it is in nicely agreement with Scanning Tunneling experiments (STM⁵³) on cuprate materials. The fact that $N(\omega)$ is most symmetric at optimal doping $\delta_p < \delta < \delta_c$ (as evident from the red circles which display a change

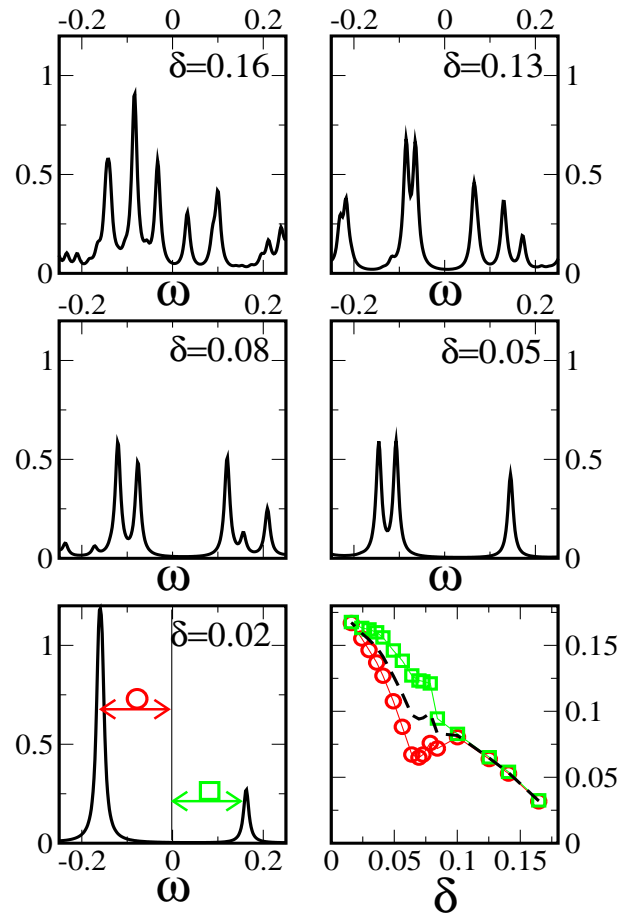


FIG. 6: (Color online). Local density of state $-\frac{1}{\pi}G_{11}(\omega)$ obtained from the cluster-impurity solution (eq. 8) for various doping δ (from top to bottom). The broadening used for display is $\eta = 7 \times 10^{-3}$. A measure of the energy scale associated with the one-particle gap (always present in the superconducting state) is given by the left (red circle) and right (green square) distances of the ED poles from the Fermi level $\omega = 0$. These are displayed as a function of doping δ in the right bottom panel.

in the slope as a function of δ) is in line with the observation carried in Fig. 1 on the special nature of this region (consistently e.g with the avoided-quantum-critical-point scenario proposed in the CDMFT study of ref.³⁹). The black dashed line is the average of the right and left gaps, and the fact that it is increasing by reducing doping (similarly to the predictions of resonating valence bond slave boson theories^{4,45,52}) shows the important result on the presence in our solution of another energy scale, different from the energy scale marked by the behavior of $\text{Re}\Sigma_{ano}(\omega_n \rightarrow 0)$ (which is instead decreasing at low doping ($\delta < \delta_p$), see right panel Fig. 5). The interpretation of these two energy scales brings to interesting physical insights, which can be put in relation with recent experiments on the cuprate materials^{54,55,56,57,58,59,60,61}. This has been presented in a previous short publication⁴⁴ and

it will be re-proposed more in detail in the following sections.

III. MOMENTUM DEPENDENT QUANTITIES: PERIODIZATION PROCEDURES

We want now to interpret the cluster results we presented in the previous section in terms of physical observables, which could be possible related to experiments. The relevant information is typically embodied in the one-particle Green's function, which in a superconducting state can be conveniently written in a Nambu-matrix notation:

$$\mathbf{G}_\sigma^{-1}(k, \omega) = \begin{pmatrix} \omega - \xi_k - \Sigma_k(\omega) & -\Sigma_{ano}(k, \omega) \\ -\Sigma_{ano}(k, \omega) & \omega + \xi_k + \Sigma_k^*(-\omega) \end{pmatrix} \quad (19)$$

Here $\xi_k = t_k - \mu$ is the free band dispersion of our model (see equation 1). In order to determine the Green's function we need therefore to determine the momentum dependent self-energy from the cluster solution, i.e. we need a periodization scheme. In previous work^{25,26,27} various periodization schemes have been proposed. The idea consists in determining the most local quantity W_r , which can be captured within the dimension of the cluster-impurity, and construct its truncated Fourier expansion¹⁵:

$$W_\sigma(k) = \frac{1}{N_c} \sum_{\mu\nu} e^{-ik\mu} W_\sigma(|\mu - \nu|) e^{ik\nu} \quad (20)$$

Smaller the neglected Fourier coefficients are (for $|\mu - \nu| > \sqrt{N_c}$), compared to the cluster $W_\sigma(|\mu - \nu|)$, more the k -dependent quantity $W_\sigma(k)$ is well approximated. In the following we present two possible cluster-quantities that can be adopted to construct the k -dependent self-energy, showing in which cases they can be considered good local quantities.

A. Self-energy Σ -periodization

The cluster self-energy (eq. 14) is a natural candidate. It is convenient, for the discussions in the following sections, to recast formula (20) in terms of the cluster eigenvalues (eq. 16):

$$\hat{\Sigma}_\sigma(k) = \sum_X \hat{\Sigma}_{X\sigma} \gamma_X(k) \quad (21)$$

where $\hat{\Sigma}_\sigma(k)$ is a 2×2 matrix containing normal and anomalous components:

$$\hat{\Sigma}_\sigma(k) = \begin{pmatrix} \Sigma_{k\uparrow}^{nor}(\omega) & \Sigma_{ano}(\omega) \\ \Sigma_{ano}(\omega) & -\Sigma_{k\downarrow}^{nor}(-\omega) \end{pmatrix} \quad (22)$$

We notice that with this formula the cluster eigenvalues $\hat{\Sigma}_X$ are directly related to the corner points in first quadrant of the Brillouin Zone $X = (0, 0)$, $(0, \pi)$, $(\pi, 0)$ and (π, π) (and we justify the notation introduced in eq. 16). $\gamma_X(k)$ are positive functions, such $\sum_X \gamma_X(k) = 1 \forall k$ ^{36,47}:

$$\begin{aligned} \gamma_{00} &= \frac{1}{4} (1 + \cos k_x + \cos k_y + \cos k_x \cos k_y) \\ \gamma_{\pi\pi} &= \frac{1}{4} (1 - \cos k_x - \cos k_y + \cos k_x \cos k_y) \\ \gamma_{0\pi} &= \frac{1}{4} (1 + \cos k_x - \cos k_y - \cos k_x \cos k_y) \\ \gamma_{\pi 0} &= \frac{1}{4} (1 - \cos k_x + \cos k_y - \cos k_x \cos k_y) \end{aligned} \quad (23)$$

We remark that, by construction, with this procedure we assume that the system is a simple Fermi liquid. We have in fact shown in Fig. 2 that the normal components of the eigenvalues of the cluster self-energy have Fermi-liquid behavior ($\text{Im}\Sigma_X \rightarrow 0$ for $\omega \rightarrow 0$). Their simple linear combination extends this property to all the k -space. The anomalous component of the lattice self-energy $\Sigma_{ano}(k)$ turns out to have a d-wave shape

$$\Sigma_{ano}(k) = 2\Sigma_{ano} (\cos k_x - \cos k_y) \quad (24)$$

in agreement with the symmetry of the superconductive gap measured in experiments on cuprates^{12,13}.

B. Cumulant \mathcal{M} -periodization

In a normal state study of the two-dimensional Hubbard Model of ref.^{36,47}, it has been shown that a more suitable local quantity to describe the Mott transition is the two point irreducible cumulant \mathcal{M} , which arises from the atomic limit by perturbatively expanding the hopping term t in Hamiltonian (1). It is simply related to the normal-component lattice self-energy Σ_k^{nor} by:

$$\mathcal{M}_k^{nor}(\omega) = \frac{1}{i\omega + \mu - \Sigma_k^{nor}} \quad (25)$$

In the cluster-impurity we have $2N_c \times N_c$ cumulant relations (2 is for the spin degeneracy), conveniently represented by a $N_c \times N_c$ cumulant-cluster-matrix $\hat{\mathcal{M}}_{\sigma c}$:

$$\hat{\mathcal{M}}_{\sigma c}^{nor}(\omega) = \left[(i\omega + \mu)\mathbf{1} - \hat{\Sigma}_{\sigma c}^{nor} \right]^{-1} \quad (26)$$

where $\mathbf{1}$ is the $N_c \times N_c$ identity matrix. The eigenvalue of the cumulant matrices are straightforwardly related to the eigenvalues of the self-energy matrices (eq. 16):

$$\mathcal{M}_X^{nor} = (i\omega + \mu - \Sigma_X^{nor})^{-1} \quad (27)$$

where the notation is again $X = (0, 0)$, $(0, \pi)$, $(\pi, 0)$ and (π, π) . As in the eq. (21), we obtain the lattice cumulant \mathcal{M}_k^{nor} by periodizing the eigenvalues of the cluster

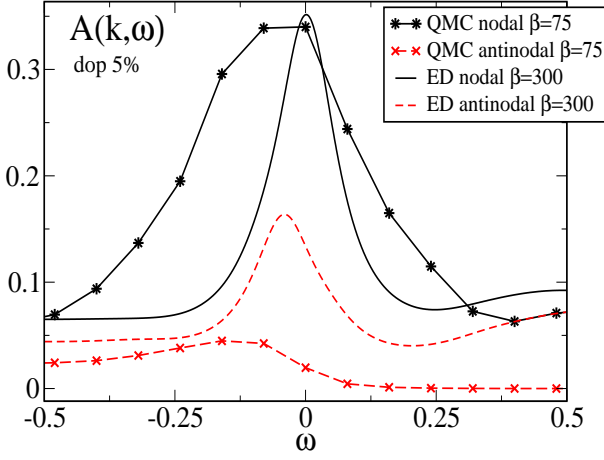


FIG. 7: (Color online). We compare the nodal and antinodal quasiparticle peaks obtained from the normal component of the superconductive ED-CDMFT-solution at zero temperature and the QMC-CDMFT normal state solution at much higher temperature ($1/T = 75$). The functions on the real axis with QMC are obtained with the maximum entropy method. To display the ED-CDMFT curves the slightly ω -dependent broadening $\eta(\omega) = 0.075 + \omega^2$ was used (see discussion in appendix A).

cumulants:

$$\mathcal{M}_k^{nor} = \sum_X \mathcal{M}_X^{nor} \gamma_X(k) \quad (28)$$

Inverting eq. (25), we finally obtained the normal-component lattice self-energy Σ_k^{nor} in the \mathcal{M} -periodization.

C. Nodal and Antinodal dichotomy: Σ -vs \mathcal{M} -periodization

It is not trivial to decide whether it is better to periodize the self-energy Σ or the cumulant \mathcal{M} . The choice could be strongly dependent on the physical properties of the system, which are not *a priori* well known. And it is not trivial either understanding *a priori* to which extend the two approximated schemes could be able to describe such properties. In this case, we rely on experimental results on cuprate materials, like e.g. the already mentioned ARPES^{12,13}, to fix a physically reasonable starting hypothesis. It is a well established experimental fact that approaching the Mott insulator the normal state Fermi surface (measured at temperatures above T_C) breaks up, displaying well defined quasiparticles in the regions (nodes) close to the centers of the quadrants of the Brillouin Zone $k \sim (\pm\frac{\pi}{2}, \pm\frac{\pi}{2})$, while quasiparticle disappear in the strong scattering regions (anti-nodes) close to the corners of the quadrants $k \sim (0, \pm\pi)$ and $(\pm\pi, 0)$. Besides photo-emission experiments, measures of transport properties show anomalous (non Fermi liquid) power-low

exponents in the temperature-dependence, especially in the under-doped regime of cuprate materials. In this case, a series of phenomenological approaches, which try to explain these experimental observations in the framework of Boltzmann theory^{48,62,63,64}, have been based on dividing the momentum space in regions of high quasiparticle scattering rate, *hot spots* around the antinodal points, and regions of low quasiparticle scattering rate, *cold spots* around the nodal point, where quasiparticles have a much longer lifetime. The simple idea underlying this choice is that the nodal region behaves as a standard Fermi liquid, while the system in the antinodal region is like an insulating state.

This *nodal/antinodal dichotomy* fits into the CDMFT frame as the natural path taken by the system to approach the doping-driven Mott transition^{26,27,36,47}. This is a general property independent of the periodizing scheme adopted. Some important differences however hold between the Σ and the cumulant \mathcal{M} periodizations, which we will illustrate in the following.

In Fig. 7 we show for example the spectral functions $A(k, \omega) = -\frac{1}{\pi} \text{Im} G_k^{nor}(\omega)$ in the nodal $k \sim (\frac{\pi}{2}, \frac{\pi}{2})$ (black continuous line) and antinodal $k \sim (0, \pi)$ (red dashed line) points of momentum space, obtained via \mathcal{M} -periodization for the case $U/t = 12$, $t' = -0.3t$ and 5% doping. We confront our zero temperature ED-CDMFT result with a QMC-CDMFT^{25,65} at much higher temperature ($T = 1/75t$), where the system is in the normal state. In the ED case we have extracted the normal part of the superconducting solution (setting $\Sigma_{ano} = 0$ in eq. 19), interpreting it as a low-temperature normal state parent of the high-temperature QMC-solution. This is far from being a trivial statement, as the normal component of a superconducting solution is not generally a normal state solution. Our aim in this picture is however to present a qualitative comparison between two very different impurity-solving methods in two very different regimes to show the generality and solidity of the nodal/antinodal dichotomy concept. This figure serves also to compare results of maxent analytic continuation of Fye-Hirsch QMC scheme with the ED results at low temperatures. The qualitative agreement is reasonably good, supporting the observation we made above on experimental results and the dichotomy nature of the physical properties in this system.

We observe in particular in Fig. 7 that the antinodal quasiparticle peak is very broad in the high-temperature QMC solution, denoting a short lifetime of quasiparticles, while it is sharper in the low-temperature ED solution, much more than the narrowing due to the different temperature (we have scaled the heights of the peaks taking the high of the nodal quasiparticle peak as reference to fix the scale between the ED and QMC curves). This goes in the direction of ARPES experimental observations, which show a sharpening of the antinodal quasiparticle in going from the normal to the superconductive state⁶⁶ by decreasing temperature. We finally point out that with the \mathcal{M} -periodization used in Fig. 7, in the

antinodal point the quasiparticle peak shifts to negative energies, opening a pseudogap. This is also in line with the above mentioned ARPES observations. On the contrary, by using the Σ -periodization the antinodal peak remains always (for all dopings) at the Fermi level, but with reduced spectral weight compared to the nodal point²⁶.

All these observations, either from experimental facts and from the output of our method, point towards a dichotomy of the nodal and antinodal regions of momentum space, which show different coherence energies. The nodal region has the highest coherence scale and sharp quasiparticles. In the antinodal region a pseudogap opens in the spectrum, and quasiparticles, if present at the gap-edge, are more broad and incoherent. It is therefore natural to assume that the Fermi-liquid nodal region is better portrayed by the Σ -periodization (which as we mentioned above describes a Fermi liquid by construction), while the antinodal insulating region is better described by the \mathcal{M} -periodization (as shown in Fig. 7).

Taking this last assumption as starting point, we compare the results of the Σ and \mathcal{M} -periodization, stressing virtues and defaults in the frame of the physical observations carried over above. A stringent test is given by reconstructing the local density of states $N(\omega) = -\frac{1}{\pi} \sum_k \text{Im} G_k(\omega)_{11}$ (where $G_k(\omega)$ is obtained by eq. 19), which can be compared with the local Green's function $G_{imp} = (\hat{G}_c)_{11}$, obtained directly in the cluster-impurity solution. This test is presented in Fig. 8. First, it is once again instructive to separately study the normal component of the superconducting state by setting $\Sigma_{ano} = 0$ in eq. (19). We focus the attention on a small-doping case $\delta = 0.05$ close to the Mott transition point. The top panel displays a full energy range which includes the lower and upper Hubbard bands. The cluster-impurity density of states $N(\omega)$ is represented by the continuous black line, the \mathcal{M} -periodization result by a red dot-dash line and the Σ -periodization result by a green dash line. Already at small doping, in the region labeled (A), the formation of a Mott gap is visible in the cluster-solution. The \mathcal{M} -periodization is capable to describe this part of the spectrum quite well (matching the continuous black line of the impurity result). On the contrary, the Σ -periodization creates artificial states in the Mott gap. This is true also at low energy (region labeled B). A close up on the Fermi level ($-t < \omega < t$) is displayed in the middle panel (with again $\Sigma_{ano} = 0$). The \mathcal{M} -periodization reproduces the formation of a low-energy pseudogap in the normal component of the spectra, as already remarked in previous normal-state studies^{36,47}, while, once again, the Σ -periodization introduces artificial states that fill the pseudogap. This simple test therefore evidences the failure of the Σ -periodization in well describing the high and low energy normal-component of Green's function, in the regions of momentum space where a pseudogap is present, like in the antinodal k -point of Fig. 7. The scenario is different if we look at the low-energy *superconducting* density of states $N(\omega)$ by restoring $\Sigma_{ano} \neq 0$ in eq. (19), as presented in the bot-

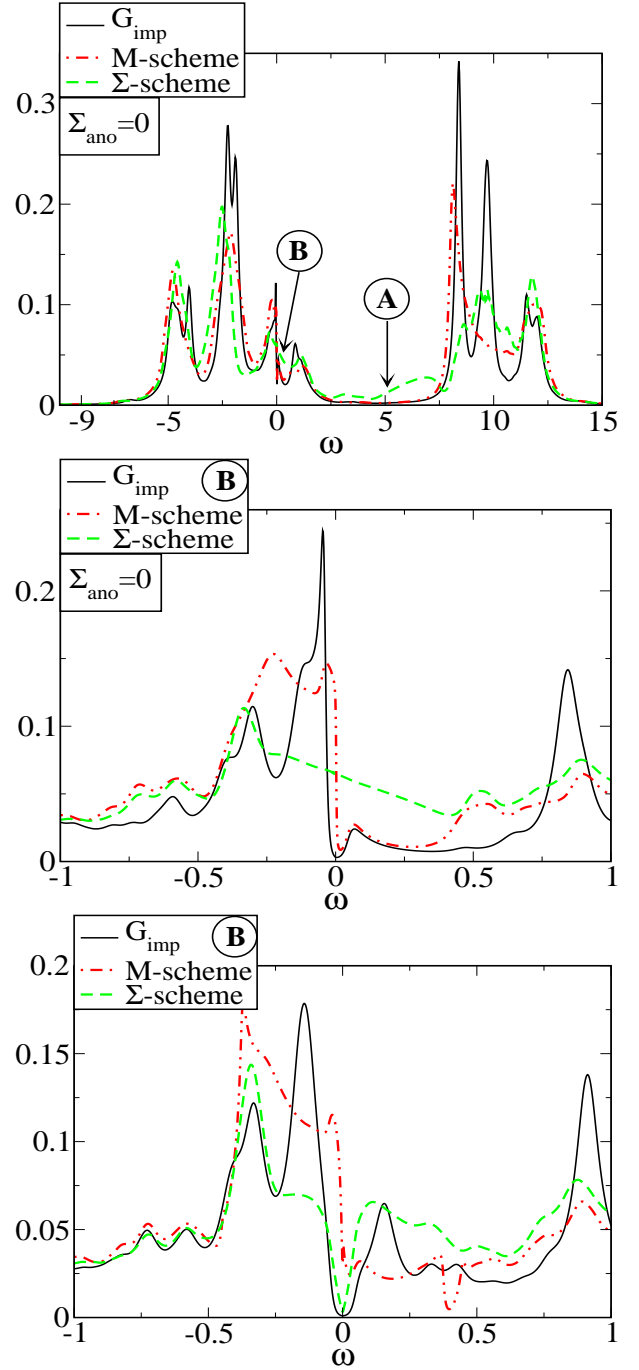


FIG. 8: (Color online). **Top panel:** reconstructed local density of states $-\frac{1}{\pi} \sum_k G_k^{nor}(\omega)$ for the normal component ($\Sigma_{ano} = 0$) of the Green's function at small doping ($\delta = 0.05$). $G_k^{nor}(\omega)$ has been obtained by either the cumulant \mathcal{M} -periodization (red point-dash line labeled \mathcal{M} -scheme) and by the Σ -periodization (green dash line labeled Σ -scheme), and confronted with the local density of states of the cluster-impurity solution (black continuous line). **Middle panel:** close-up at the Fermi level. **Bottom panel:** the local density of states of full superconducting solution ($\Sigma_{ano} \neq 0$) selects in the k -summation only the nodal points. A low-energy confronting with the cluster-impurity solution shows a different matching of the cumulant and self-energy periodizations with the cluster-impurity result. The display on the real axis of the Green's function has been obtained by introducing a ω -dependent broadening $i\eta(\omega)$ (see appendix A for details).

tom panel of Fig. 8. Here it is the Σ -periodization line (green dash line) which better portrays the cluster spectrum (black continuous line). The \mathcal{M} -periodization this time introduces spurious states close to the Fermi level ($\omega = 0$). This is not contradictory with respects to the result presented above on the normal component of the system (top and middle panels). By adding the d-wave superconducting gap in fact, we select at low energies ($\omega \rightarrow 0$) only the region of momentum space close to the nodal points, where the gap is zero. These points dominate in fact the sum $-\frac{1}{\pi} \sum_k \text{Im} G_k(\omega)_{11}$. $N(\omega)$ for $\omega \rightarrow 0$ is therefore a direct probe of the nodal point behavior only (while without superconducting gap, i.e. $\Sigma_{ano} = 0$, all k -points eventually contribute in the summation at low energies).

We clarify this last statement. Let's assume as starting point that at the nodes quasiparticles are well defined on the full range of doping. We can extract from eq. (19) the low energy ($\omega_n \rightarrow 0$) Green's function:

$$\begin{aligned} \text{Re} \Sigma_k(\omega_n) &\sim \text{Re} \Sigma_k(0) \\ \text{Im} \Sigma_k(\omega_n) &\sim (1 - Z_k^{-1}) \omega_n \end{aligned}$$

and

$$G(k, \omega_n) \sim \frac{\frac{Z_k}{2}(1 - \tilde{\xi}_k/E_k)}{\omega_n + E_k} + \frac{\frac{Z_k}{2}(1 + \tilde{\xi}_k/E_k)}{\omega_n - E_k} \quad (29)$$

For convenience's sake, we have enlighten the quasiparticle dispersion

$$\begin{aligned} \tilde{\xi}_k &= Z_k [\xi_k + \text{Re} \Sigma_k(0)] \\ E_k &= \sqrt{|\tilde{\xi}_k|^2 + |Z_k \Sigma_{ano}(k, 0)|^2} \end{aligned} \quad (30)$$

The nodal point is the only one gapless at low energies and the quasiparticle spectrum can be linearized (eq. 30):

$$\begin{aligned} E_{k_{nod}} &= \sqrt{|\tilde{\xi}_{k_{nod}}|^2 + |Z_{k_{nod}} \Sigma_{ano}(k_{nod})|^2} \\ &= \sqrt{v_{nod}^2 k_{\perp}^2 + v_{ano}^2 k_{\parallel}^2} \end{aligned} \quad (31)$$

$v_{nod} = |\nabla_k \tilde{\xi}_k|$ is the quasiparticle Fermi velocity perpendicular to the Fermi surface, $v_{ano} = Z_{nod} |\nabla_k \Sigma_{ano}(k)|$ is parallel to the Fermi surface. After analytic continuation $\omega_n \rightarrow \omega + i\delta$, it is now easy to calculate the low energy behavior of the one-particle density $N(\omega) = \frac{1}{\pi} \sum_k \text{Im} G_k(\omega)$

$$N(\omega) \sim \frac{1}{\pi} \sum_j^{\text{nodes}} \frac{Z_{nod_j}}{v_{nod_j} v_{ano_j}} \omega \quad (32)$$

i.e. $N(\omega)$ is linear in frequency close to the Fermi energy and the slope is uniquely determined by the quasiparticle nodal velocity v_{nod} , by the nodal derivative of the superconducting gap v_{ano} and by the nodal quasiparticle residuum $Z_{k_{nod}}$. In other words, the low-energy density of states in the d-wave superconductor is a direct measure of the spectra at the nodes. This result explains

the low-energy spectrum of the cluster density of states (black-continuous line in Fig. 8), which is roughly linear for $\omega \rightarrow 0$, in the limit of the energy-resolution given by ED impurity solver.

The fact that here the Σ -periodization better portrays the cluster result is consistent with the hypothesis of Fermi-liquid behaviour at the nodal points of momentum space, well described by the self-energy. The results of the normal component of the system suggest instead that in other regions of momentum space (at least close to the Mott transition point), a pseudogap opens in the spectrum and quasiparticles die in the anti-nodes. In the latter regions a cumulant \mathcal{M} -periodization is more appropriate than the Σ -periodization.

IV. PROPERTIES OF THE NODAL AND ANTINODAL POINTS

In this section we follow the observations presented above on the nodal/antinodal dichotomy and study the physical properties of the system in the nodal and antinodal points, completing in detail the work presented in ref.⁴⁴. In order to be able to make contact with the experiments, we need to extract the fully momentum dependent Green's function $\hat{G}_k(\omega)$ (see equation 19), which can be generally related to the response functions. We employ therefore a periodizing procedure to extract the k -dependent normal and anomalous components $\Sigma_k(\omega)$ and $\Sigma_{ano}(k, \omega)$ of the k -dependent self-energy. As discussed above, it is reasonable to start by assuming a d-wave shape of the superconducting gap, which is naturally obtained in our scheme by periodizing the anomalous component of the cluster self-energy via eq. (24). At the nodes, we periodize also the normal component of the self-energy via eq. (21). This guarantees in particular Fermi liquid properties in the nodal region of momentum space. At the anti-nodes instead the insulating properties of the normal component of the system (like the formation of a pseudogap at low energy and of the Mott gap at higher energies, see Fig. 8) are better portrayed by periodizing the cumulant \mathcal{M}^{nor} , according to eq. (28).

By adopting this procedure we can first obtain quasiparticle spectra in the *nodal and antinodal points of momentum space*, as it is shown in Fig. 9. In order to define the k vectors in the nodes and in the anti-nodes, we follow an operative definition, similar to the one used in the ARPES experiments of ref.⁵⁵. The nodal point k_{nod} [antinodal point k_{anod}] is chosen as the one having the sharpest quasiparticle peak in moving on the path $(0, 0) \rightarrow (\pi, \pi)$ [$(0, \pi) \rightarrow (\pi, \pi)$] of momentum space. The vectors k_{nod} and k_{anod} as a function of doping δ are shown in panel A of Fig. 9. We notice that k_{anod} is a monotonic decreasing function of the δ . This is intuitively expected in a standard Fermi liquid, where the approach to the Mott transition at $\delta = 0$ is accompanied by an increase of the volume enclosed by the Fermi surface in momentum space, which is proportional to the density $n = 1 - \delta$

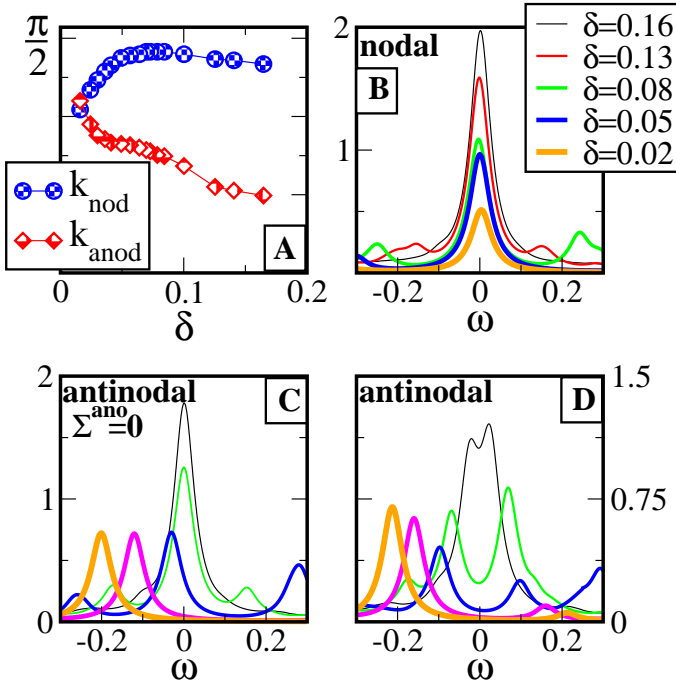


FIG. 9: (Color online). **Panel A:** nodal k_{nod} and antinodal k_{anod} positions of the quasiparticle peaks in the first quadrant of the Brillouin Zone as a function of doping δ . **Panel B:** Nodal peaks are found always at the Fermi level and decrease with doping δ in approaching the insulator. **Panel C:** At high doping ($\delta > \delta_c \sim 0.08$) antinodal peaks are also found at the Fermi level in the normal component of the system (set $\Sigma_{ano} = 0$ in eq. 19). For ($\delta < \delta_p \sim 0.06$) however they shift to negative energy opening a pseudogap. **Panel D:** The actual antinodal spectra ($\Sigma_{ano} \neq 0$ in eq. 19) show to become asymmetric for $\delta > \delta_c$, when the pseudogap starts opening in the normal component (see panel C, and bottom right panel of Fig. 6).

of the system (Luttinger theorem⁶⁷). The k_{nod} vector on the contrary displays a non-monotonic behavior, showing to decrease by reducing doping in correspondence of the special doping $\delta_c \sim 0.08$, which appears in our study as a critical point marking a change in the physical properties of the system. In the following section we will show that we can relate this behavior of the nodal and antinodal k points to a topology change in the Fermi surface.

In the remaining panels of Fig. 9, we show the spectral function $\text{Im}[\tilde{G}_k(\omega)]_{11}$ (from eq. 19). As previously explained (see also appendix A), within the ED-CDMFT method it is possible to display Green's functions on the real frequency axis ω by expressing them in a pole expansion, displayed by adding in the denominator a small imaginary part $i\eta$ (here we adopted $\eta = 0.03t$). At the nodal point (panel B) the d-wave superconducting gap is zero, and a Fermi liquid quasi-particle peak is always found at the Fermi level ($\omega = 0$) for different doping δ . The approach to the Mott insulator ($\delta \rightarrow 0$) is marked by a progressive reduction of the quasi-particle peaks. This

behavior is reminiscent of the Mott transition described in the standard infinite dimensional Hubbard Model. At the antinodal point the superconducting gap is maximal, a gap in the spectra is therefore expected. Before looking at the full antinodal spectrum, however, it is instructive to look at the contribution coming from the normal component, which can provide information on the physical properties of the liquid underlying the superconducting state. The normal-component spectra can be simply obtained in our scheme by zeroing the anomalous component of the self-energy $\Sigma_{ano}(k, \omega)$ in eq. 19. These spectra are displayed in panel C of Fig. 9. At doping $\delta > \delta_c$, a Fermi liquid quasi-particle peak is also found at the Fermi level ($\omega = 0$). In this region of the phase diagram, the normal properties of the system are therefore Fermi-liquid-like (and also k_{nod} and k_{anod} are monotonically decreasing with δ , as described above). In correspondence of the critical doping δ_c however, a pseudogap opens and a quasi-particle peak is found at the gap edge at negative energy ($\omega < 0$). The pseudogap increases in approaching the Mott transition ($\delta \rightarrow 0$), while, differently from the nodal point, the peaks show a roughly constant height. This behavior at the anti-nodes of the normal component of this superconducting solution can be smoothly connected to results previously obtained in CDMFT studies of the normal state^{36,47}. For $\delta < \delta_c$ therefore, the normal component of the system is not a Fermi liquid in the strict sense, at least in the region of momentum space close to the antinodal points (but a behavior unusual for a Fermi liquid is also detected by the decreasing value of k_{nod} in panel A). This behavior appears also in the total antinodal spectra (upon restoring the superconducting gap $\Sigma_{ano} \neq 0$ in eq. 19), which we show in panel D. At doping $\delta > \delta_c$, the quasi-particle peaks present in the normal component are parted into two bands by the opening of a superconducting gap, resulting in the typical BCS symmetric spectra. For $\delta < \delta_c$, however, the pseudogap already present in the normal component super-impose to the superconducting gap, resulting in asymmetric spectra. This antinodal spectra nicely explain Fig. 6, where the local density of states $N(\omega)$, directly obtained from the cluster-impurity solution, is displayed. The appearance of the asymmetry for $\delta < \delta_c$ is therefore interpreted by our k -momentum analysis as the appearance of the pseudogap phase, which marks a departure from a Fermi liquid based BCS superconductor, once again at the critical doping δ_c . And these observations must be directly linked to experimental spectra, either in the anti-nodes of momentum space, obtained for example with angle resolved photo-emission^{12,13}, and locally in real space, with for example scanning tunneling spectroscopy⁵³.

In order to characterize the Mott transition, it is useful to extract the quasi-particle residuum, which is defined as

$$Z_k = \left(1 - \frac{\partial \text{Re}\Sigma^{nor}(k, \omega)}{\partial \omega} \right)^{-1}_{\omega \rightarrow 0, k=k_F} \quad (33)$$

with $k_F = k_{nod}$ or k_{anod} in our case. This quantity corre-

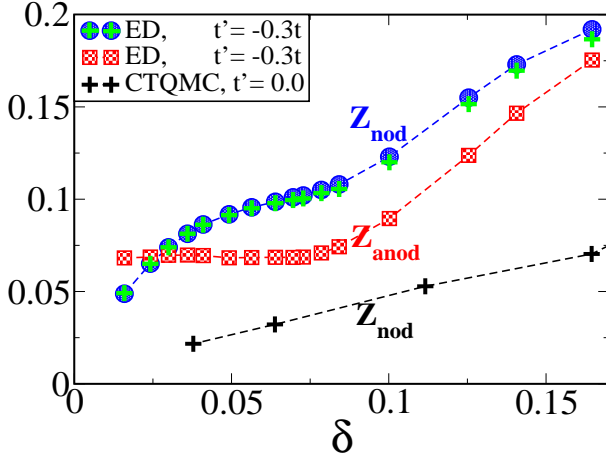


FIG. 10: (Color online). Quasiparticle residuum at the nodal point Z_{nod} and antinodal points Z_{anod} as a function of the doping δ , evaluated as area of the quasiparticles peaks shown in Fig. 9 (as a crosscheck, Z_{nod} is also evaluated as the slope of the imaginary part of the self-energy on the Matsubara axis, green cross). While Z_{nod} monotonically decrease with doping, as in the standard picture of the Mott transition, the antinodal Z_{anod} shows to stay constant upon opening of the pseudogap ($\delta > \delta_c \sim 0.08$). For comparison's sake, we display the nodal Z_{nod} obtained by CTQMC⁴¹ on the two dimensional Hubbard Model with similar parameters ($U = 12t, t' = 0.0, \beta = 200$). These quasiparticle residua should be compared with their cluster counter-parts in Fig. 4.

sponds to the area of the quasiparticle peaks (e.g. panel A of Fig. 9), it is unity in the non-interacting case, less than unity in an interacting Fermi liquid. In the standard description of the Mott transition (i.e. the infinite dimensional Hubbard Model) $Z \rightarrow 0$ linearly as $\delta \rightarrow 0$ (see ref.⁵). It is interesting therefore to observe how this quantity behave in the nodal and antinodal k -points by varying doping δ , as we show in Fig. 10. We can give in this way a momentum space interpretation of the corresponding cluster Z_X that we have discussed in Fig. 4. As we already said, at the nodes well defined quasiparticle peaks are observed at every doping δ at the Fermi level. The residuum Z_{nod} is therefore well defined according to the expression given above (which is strictly valid at $\omega = 0$), as in a typical Fermi liquid. This is confirmed by the good numerical accord between the blue circles (calculated by integrating the area of the peaks, which are displayed by introducing the artificial broadening parameter $\eta = 0.03t$) and the green crosses (calculated more precise within our method by using eq. 33 on the Matsubara axis). For comparison's sake, we present also the nodal quasi-particle residuum extracted in a CDMFT-study implemented with a different impurity solver, the CTQMC⁴¹, in the two dimensional Hubbard model with Hamiltonian parameters $U = 12t$ and $t' = 0t$. The comparison is only qualitative and it is aimed to get insight into the physical trends. We indeed observe a monotonically decreasing Z_{nod} as a function of

the doping δ , similarly to the standard infinite dimensional Hubbard Model. We cannot however state within our numerical resolution if $Z_{nod} \rightarrow 0$ exactly at the Mott point $\delta = 0$ (as it seems also to suggest the CTQMC result), or rather it extrapolates to a finite but very small ($Z_{nod} < 0.02t$) value. In the antinodal point more attention has to be paid in defining a quasi-particle residuum Z_{anod} . As stressed above, for $\delta > \delta_c \sim 0.08$ quasiparticle peaks are present at the Fermi level (panel C of Fig. 9), and Z_{anod} can be well defined by eq. 33. For $\delta < \delta_c \sim 0.08$ however a pseudogap opens. Even if a peak can be identified at the gap-edge, it is not strictly speaking a Landau-Fermi liquid quasiparticle, as the imaginary part of the self-energy is non-zero (even if small), i.e. the quasiparticle has a finite lifetime. Formula 33 cannot be directly employed. However we can still calculate the area of the peak, and display its behavior as a function of the doping δ . We find in our result that for $\delta < \delta_c$, once the pseudogap opens and the peaks move to negative frequency, the weight Z_{anod} stays constant up to the Mott transition point. The behavior of Z_{nod} and Z_{anod} here presented has to be connected with the effective cluster correspondents Z_X (Fig. 4). According to eq. 23, these are interpreted in momentum space as the quasiparticle residua in the corner points of the first quadrant of the Brillouin Zone (therefore far from the Fermi surface), while Z_{nod} and Z_{anod} , which are instead calculated on the Fermi surface, have a real physical meaning. In spite of this however, the cluster Z s already embody the physical properties (a Z going to zero and another non decreasing for $\delta \rightarrow 0$) characteristic of the Mott transition in this two-dimensional system.

We stress that the description of the Mott transition we find in this study of the two dimensional Hubbard Model is very different from the standard Mott transition picture in infinite dimension⁵. In our system different regions of momentum space behave very differently in approaching the transition point. In this way we can go from a Fermi-liquid-based superconductor (realized for $\delta > \delta_c$) into the Mott insulator (at $\delta = 0$) by passing through a phase $0 < \delta < \delta_p$, where the system is at the same time insulating in the antinodal region and Fermi liquid in the nodal region of momentum space. This latter appears to approach the Mott point in the standard (infinite dimensional Hubbard Model) way, with a quasiparticle residuum $Z_{nod} \rightarrow 0$ (at least within our numerical precision). In the antinodal region instead the quasiparticle peak (which underlies the superconducting gap) stops reducing at $\delta = \delta_c$ and shifts to negative energies opening a pseudogap. This behavior is reminiscent of the *orbital selective Mott transition*, found e.g. in two band Hubbard-like models^{68,69,70}, where the spectral weight is not transferred from the low energy ($\omega = 0$) to the Hubbard bands (located at a energy scale of order $\sim U$), as in the standard Mott transition, but rather onto a smaller energy scale of the order of an exchange coupling $J \sim 1/U^2$, inside the Mott gap. In spite our model is a one band one, different regions of momentum space ap-

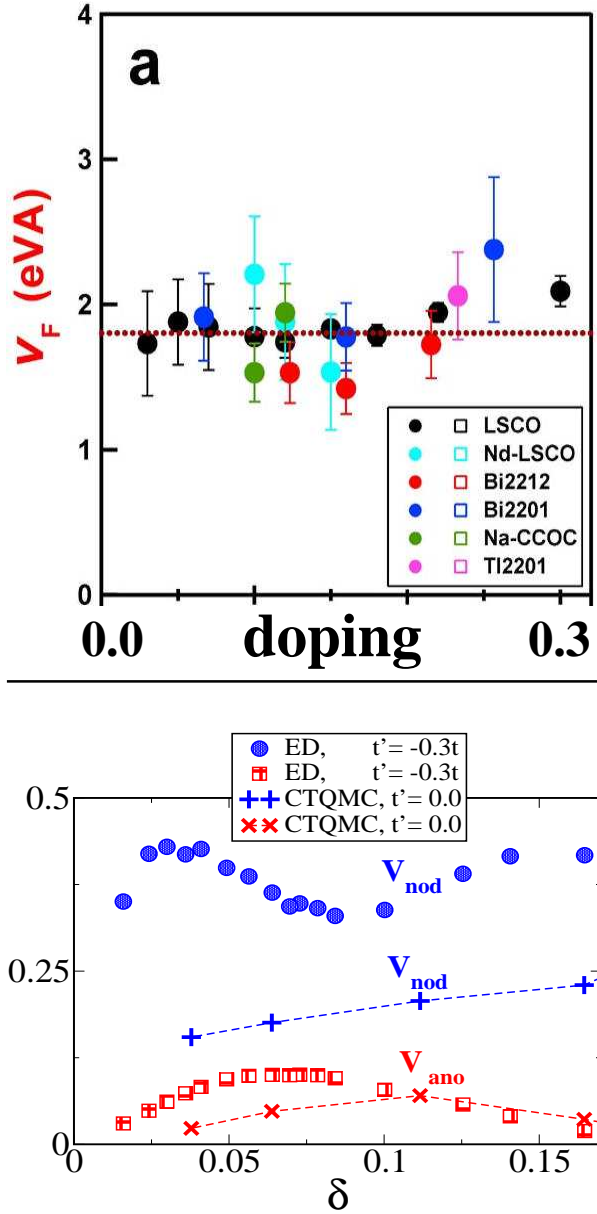


FIG. 11: (Color online). **Top:** Nodal velocity as a function of doping measured from the quasiparticle dispersion of different materials (figure taken from ref.⁷¹). To be confronted with the nodal component of the velocity v_{nod} calculated in our work and displayed in the bottom. **Bottom:** Nodal anomalous velocity $v_{ano} = Z\Sigma_{ano}(k_{nod})$ (tangent component of the nodal velocity) and nodal quasiparticle velocity $v_{nod} = Z|\nabla_k \xi_k|$ (component of the nodal velocity perpendicular to the Fermi surface) as a function of doping δ (units are $a_o t$, where a_o is the square lattice spacing). The trends are compared with CTQMC⁴¹ calculations on the two dimensional Hubbard Model with similar parameters ($U = 12t, t' = 0.0, \beta = 200$).

pear to behave as different bands. By decreasing doping δ , a first "orbital selective Mott transition" takes place at δ_c in the antinodal regions, and a full Mott transition takes finally place at $\delta = 0$.

Useful information on the nodal point can be extracted by performing a low energy expansion of the Green's function (see eq. 29 and 31), taking advantage of the Fermi liquid properties of the nodal point. In particular the nodal velocity has two components, one coming from the normal part $v_{nod} = |\nabla_k \xi_k|$ parallel to the Fermi surface, and the other related to the superconducting gap $v_{nod} = Z_{nod}|\nabla_k \Sigma_{ano}(k)|$, perpendicular to the Fermi surface. v_{nod} can be experimentally extracted, e.g. from the ARPES quasiparticle dispersion at the node⁷¹, while v_{ano} can be determined e.g. as the slope of the superconducting gap at the node⁵⁵. In Fig. 11 v_{nod} and v_{ano} are displayed as a function of doping δ . For comparison's sake, in the top panel we show experimental nodal velocity extracted from different materials (the figure has been taken from the supplementary material of ref.⁷¹). In the bottom panel we show our result, and also insert for a qualitative comparison the CTQMC-CDMFT result of ref.⁴¹. v_{nod} shows to be greater than v_{ano} , in agreement with experimental observation (see e.g. ref.¹²). In ED-CDMFT it slightly oscillates around a constant value from the over-doped to the under-doped ($\delta < \delta_c$) side of the phase diagram, while in the CTQMC case it is slightly decreasing with decreasing doping. This behavior is in good qualitative agreement with experimental results reported in the top panel (a quantitative comparison would roughly hold, for a lattice spacing $a_o \sim 4\text{\AA}$ and a $t \sim 0.5$ eV, $v_{nod} \sim 1$ eVÅ, which is of the order of magnitude of experiments). Remarkably, either with ED and with CTQMC, v_{ano} displays a dome-like shape, with a maximum around optimal doping $\delta_p < \delta < \delta_c$ (notice that in the ED case $t' = -0.3t$ $\delta_c \sim 0.08$ while in the CTQMC case $t' = 0$ $\delta_c \sim 0.12$). This is an important result: as shown in formula 30 and discussed in ref.⁴⁴, the anomalous velocity $v_{ano} = \sqrt{2}Z_{nod}\Sigma_{ano}(\omega = 0)\sin k_{nod}$ can be interpreted as a direct measure of the superconducting gap in the nodal region, which reveals non-monotonic, in agreement with some recent experimental spectroscopy results^{54,55}. The agreement of the trend of v_{ano} between the ED and CTQMC solutions shows that this result is solid from the theoretical side too. We will come back to discuss the nodal and antinodal gap more in detail at the end of this section.

At the nodal point, the combination of the quasiparticle residuum Z_{nod} and nodal velocities can give further information, which can be confronted with experimental observable quantities and which can further support the physical description drawn from our CDMFT result. Basing on the Fermi liquid assumption at the nodes, in eq. (32) we have for example extracted the low energy ($\omega \rightarrow 0$) behavior of the local density of states $N(\omega) \sim \frac{Z_{nod}}{v_{nod}v_{ano}}\omega$. This value is displayed as a function of doping δ in Fig. 12, comparing once again the ED-CDMFT results of this work (with $t' = -0.3t$) with the CTQMC-CDMFT results of ref.⁴¹ (with $t' = 0$). Once again it is the trend we want to compare rather than the quantitative values. Starting from the over-doped side, the slope of $N(\omega)$ is decreasing monotonically by decreas-

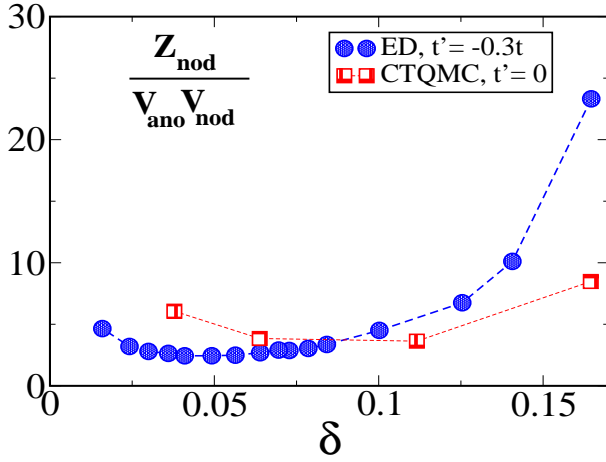


FIG. 12: (Color online). The slope of the low energy local density of states $N(\omega) \sim \frac{Z_{nod}}{v_{\Delta} v_{nod}} \omega$ is displayed as a function of doping δ . Trends are compared with CTQMC⁴¹ calculations on the two dimensional Hubbard Model with similar parameters ($U = 12t$, $t' = 0.0$, $\beta = 200$).

ing doping, until showing a slight up-turn close to the Mott transition (observable both in the ED and CTQMC cases). While the linearity of $N(\omega)$ it is well established in scanning tunneling experiments⁵³, the behavior of the slope as a function of doping is at the moment very difficult to extract (as it is not possible to obtain absolute values for different densities). Our result (in particular the up-turn tendency at small doping) has to be therefore considered a theoretical prediction.

A further ratio of experimental relevance can be connected at first order to the low energy ($\omega \rightarrow 0$) linear behavior of the B_{2g} Raman response function $\chi_{B_{2g}} \sim \frac{Z_{nod}^2}{v_{nod} v_{ano}} \omega$ (see ref.⁵⁴) and the low temperature ($T \rightarrow 0$) behavior of the superfluid stiffness $\rho_s(T) - \rho_s(0) \sim \frac{Z_{nod}^2}{v_{nod} v_{ano}} \omega$, which can be extracted from measures of the penetration depth^{72,73}. Our results (together with the CTQMC results of Ref.⁴¹) are shown on the bottom panel of Fig. 13 and compared with the aforementioned Raman and penetration depth data presented in the top panel (the figure has been taken from ref.⁵⁴). The remarkable feature, found in experiments and supported in our calculation, is the constant value displayed by this ratio in the under-doped region ($\delta < \delta_c$). While in the experimental results a sum rule is assumed, in order to being able to compare measures from different doping/samples, our theoretical results are derived from a bare strongly correlated electron model, where other kind of assumptions and approximations (as explained in the previous sections) are implied. The convergence of experimental and theoretical results therefore strongly supports these findings, presenting them as distinctive feature of the cuprate superconductor nodal dispersion.

The behavior of the spectra presented in Fig. 9 can be directly connected to spectroscopy experiments. In

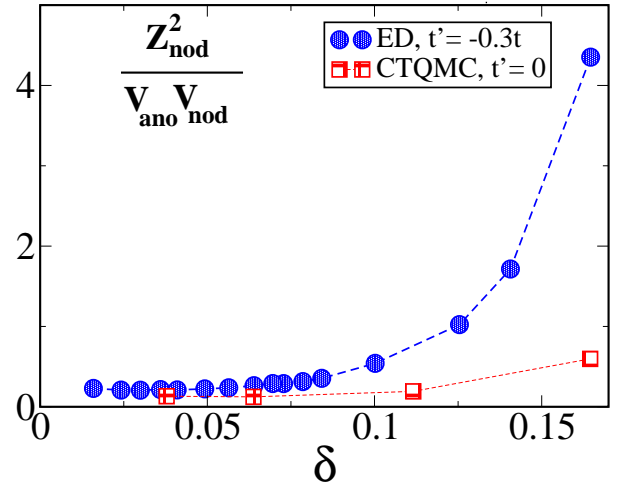
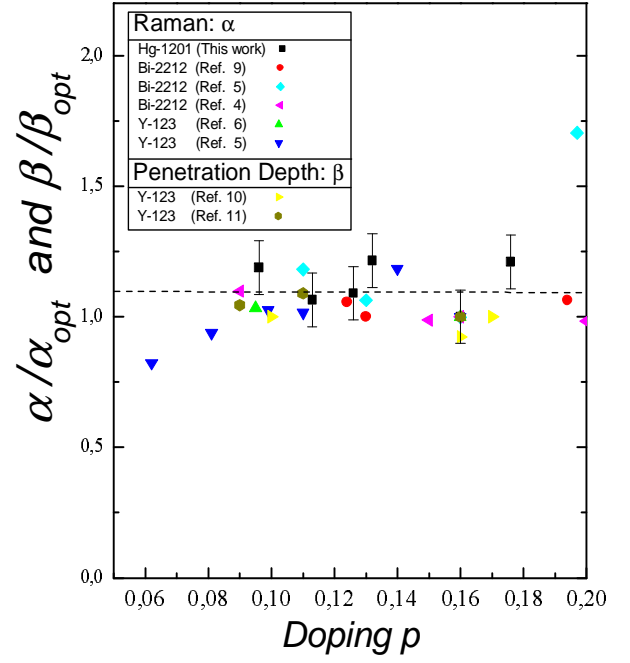


FIG. 13: (Color online). **Top**: the linear coefficient of the low energy Raman response $\chi_{B_{2g}}(\omega) \sim \alpha \omega$ and the low temperature superfluid stiffness (from penetration depth) $\rho_s(T) - \rho_s(0) \sim \beta T$, extracted from various experiments (figure taken from ref.⁵⁴). Quantities are normalized at the optimal doping value. **Bottom**: The linear coefficient of the Raman response and superfluid stiffness (see top panel) as extracted from our calculation $\frac{Z_{nod}^2}{v_{\Delta} v_{nod}}$ and displayed as a function of doping δ . Trends are compared with CTQMC⁴¹ calculations on the two dimensional Hubbard Model with similar parameters ($U = 12t$, $t' = 0.0$, $\beta = 200$).

particular, recently a lively debate has risen on the momentum resolved structure of the superconducting gap^{56,57,58,59,74,75,76,77}. We proceed as in ARPES experiments (see e.g.⁵⁵), and extract the quasiparticle gap in

the nodal and antinodal points of momentum space, taking advantage of the periodizing scheme we have introduced. To this purpose, it is convenient to use the low energy ($\omega \rightarrow 0$) expansion carried out in eq. 29. In particular we have seen that quasiparticle peaks are always found in our result, even if not in a strict sense (in the pseudogap region $\delta < \delta_c$ quasiparticle peaks are located at the gap-edge and have finite lifetime), and therefore we expect the expansion to be reasonably good at small frequency (i.e. $\omega \leq$ the superconducting gap). We can in this case write the total gap $\Delta_{tot}(k, \omega)$ as the quadratic sum of two contributions (see eq. 30):

$$\Delta_{tot}^2(k, \omega) = \Delta_{nor}^2(k, \omega) + \Delta_{sc}^2(k, \omega) \quad (34)$$

where $\Delta_{sc}(k, \omega) = Z_k \Sigma_{ano}(k, \omega)$ is the usual d-wave superconducting gap (notice that it is directly connected, except for constant factors, to the anomalous component of the nodal velocity $v_{ano} \sim Z_{k_{nod}} \Sigma_{ano}(\omega = 0)$ discussed in Fig. 11), $\Delta_{nor}(k, \omega) = \tilde{\xi}_k(\omega) = Z_k [\xi_k + \text{Re}\Sigma_k(\omega)]$ is a normal contribution to the gap which can arise only if, for some k and $\omega \rightarrow 0$, the normal component of the self-energy $\Sigma_k(\omega)$ grows enough so that the band equation $\tilde{\xi}_k = 0$ cannot be satisfied, i.e. there is not Fermi surface. Now, this does not take place at the nodes, where quasiparticles are found for all dopings (panel B of Fig. 9), $\tilde{\xi}_k = 0$, the system presents standard Fermi liquid properties, and the total spectral gap coincides with the superconducting gap $\Delta_{tot} \equiv \Delta_{sc}$. (This already suggests that in looking for the “real” superconducting gap of the system one should look at the nodal region gap. Recent theoretical⁴¹ and experimental Raman spectroscopy studies⁷⁸ point at this direction.) In the antinodal region, instead, we have observed that a pseudogap opens in the normal component for $\delta < 0.08$ (panel C of Fig. 9), and this fact is associated in our calculation with the appearance of lines in k -space close to the antinodal region where the self-energy is diverging (see ref.^{36,47}). It is not possible therefore to satisfy the equation $\tilde{\xi}_k = 0$, and a Fermi surface does not exist anymore. The normal contribution Δ_{nor} kicks in, and determines the properties of the total antinodal gap Δ_{tot} , originating the asymmetric spectra we already described in panel D of Fig. 9.

We can extract, like in ARPES experiments (e.g. ref.⁵⁵), the antinodal gap Δ_{tot} from the spectra of panel D of Fig. 9 by measuring the distance of the quasiparticle peaks at the gap-edge from the Fermi level $\omega = 0$. In the same way, from panel C of Fig. 9, we can measure the normal contribution Δ_{nor} , and display them as a function of doping δ . We can compare directly with experimental results, which are shown in the top panel of Fig. 14 (for convenience’s sake we extract the picture from the Raman results of ref.⁵⁴, but ARPES points are also displayed), while in the bottom panel we show the results of our calculation. The antinodal gap Δ_{tot} is a monotonic decreasing function of doping (curve labeled “Anti Nodal B_{1g} ” in the top panel of Fig. 14), as it has been known from experiments since a long time (see e.g. ref.^{12,13}) and predicted in the most popular theories

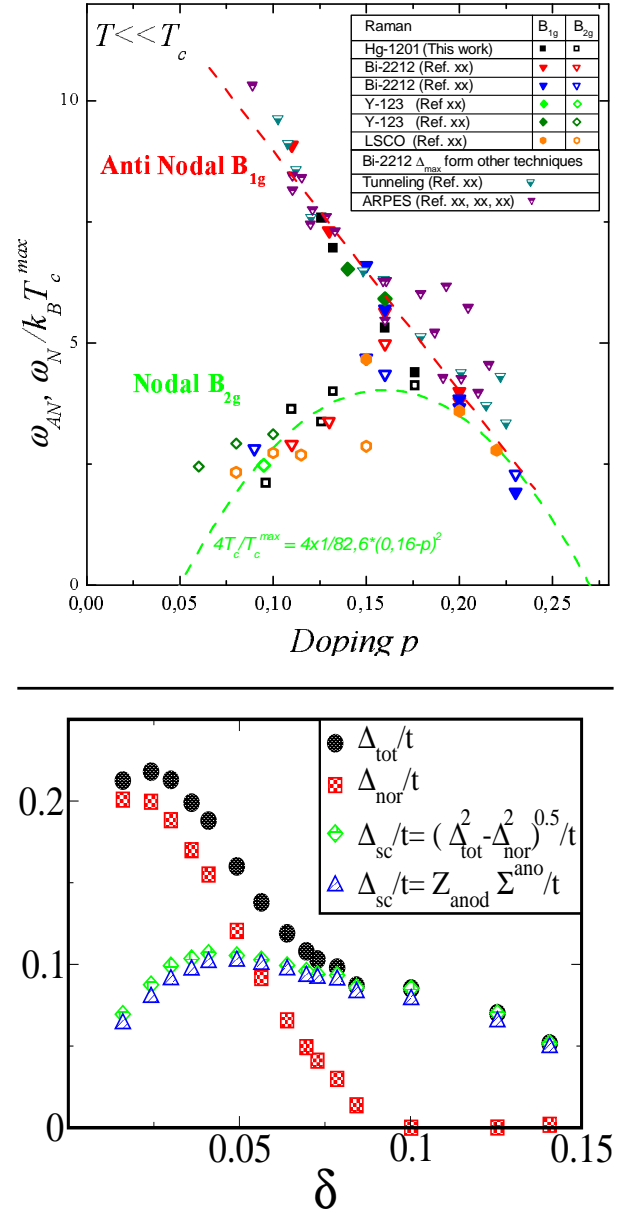


FIG. 14: (Color online). **Top:** Nodal (B_{1g}) and antinodal (B_{2g}) quasiparticle gap extracted by different spectroscopy experiments (in particular, the figure is taken from the Raman spectroscopy results of ref.⁵⁴) as a function of doping. **Bottom:** The antinodal gap Δ_{tot} and the nodal Δ_{sc} extracted from the spectra of Fig. 9, as a function of doping δ . Δ_{nor} is the pseudogap in the normal component extracted in panel C of Fig. 9.

of high temperature superconductivity (e.g. resonating valence bond theory⁴, for a recent general review see e.g.⁴⁵). In our calculation we show that at small doping an important contribution comes indeed from the normal component Δ_{nor} , which appears at δ_c and it is also monotonic. From the experimental side, the novelty comes from precise measures of the nodal gap, re-

cently obtained by Raman spectroscopy⁵⁴ and ARPES⁵⁵, which show surprisingly that in this region of momentum space the spectral gap is non-monotonic with doping δ , tracking instead the behavior of the critical temperature T_c (curve labeled “Nodal B_{2g} ” in the top panel of Fig. 14). In our calculation the nodal gap corresponds to the anomalous component of the nodal velocity v_{ano} , which we have discussed in Fig. 11, and which shows indeed a behavior strongly similar to these experimental results. We clarify now how it is possible that the nodal component of the gap tracks T_c as a function of doping δ , while at the same time the antinodal component is monotonic, by disentangling the superconducting contribution $\Delta_{sc} = \sqrt{\Delta_{tot}^2 - \Delta_{nor}^2}$, which we also display in the bottom panel of Fig. 14. To check the validity of our formula 34, and making connection with $v_{ano} \sim Z_{k_{nod}} \Sigma_{ano}$, which has been evaluated at the nodal point, we also evaluate and display $\Delta_{sc} = Z_{ano} \Sigma_{ano}(k_{ano}, \omega = \Delta_{nor})$, finding numerical agreement. This shows indeed that the total antinodal gap Δ_{tot} has indeed two distinct contributions, displaying opposite trends with dopings. In the underdoped side Δ_{nor} dominates in the antinodes, and creates a monotonically increasing total gap. In the nodes, instead, Δ_{nor} is zero and only the superconducting gap is detectable. In our results we connect therefore the experimentally observed two-gap phenomenon with the opening of the pseudogap at the anti-nodes at a finite critical doping δ_c . And, according to our point of view, this is an effect arising in a strongly correlated electron system that approaches the doping-driven Mott transition in a two dimensional lattice. The fact that Δ_{sc} tracks T_c ⁷⁸ is remarkably similar to the standard BCS superconductivity. These results put strong constraints on the theories of cuprate-based superconductivity, which have to consider the presence of these two distinct components in the spectral gap and its interplay with the dome-like shape of the order parameter, the rising of the pseudogap phase and the approaching to the Mott insulator. Our cluster results, interpreted via a periodization procedure, well fit the experimental observations and give a simple interpretation in terms of a combination of all these effects.

V. A MIXED-PERIODIZATION SCHEME

The discussion presented in the previous subsections is valid close to the nodal and antinodal points of momentum space, where we have shown that periodizing the self-energy or the cumulant its a reasonable approximation. Obtaining information in intermediate region of momentum space, between the nodal and antinodal ones, is beyond the limits of a pure 2×2 -plaquette study. In this region in fact the Fermi liquid physical properties of the nodal points have to interlace in some non-trivial way with the insulating-like properties of the antinodal point. A detailed description of this phenomenon can be taken into account by studying bigger cluster (i.e. obtaining a

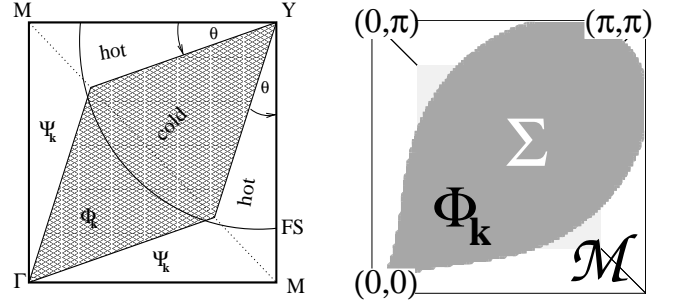


FIG. 15: Left: the shaded region is the patch Φ_k used in the phenomenological Boltzmann approach of ref.⁴⁸ in the first quadrant of the Brillouin Zone. Right: the patch Φ_k used in this work (see formula 37).

better truncation of the Fourier expansion in eq. 20), at present not possible with ED-CDMFT. Nevertheless we want to keep in this section a low profile, and introduce a first order description of the spectral properties in all momentum space, which could be compared to experimental results (like e.g. ARPES). We want therefore to introduce a periodizing scheme able to describe

1. a Fermi liquid quasiparticle in correspondence of the nodal point
2. the opening of a pseudogap in the antinodal points in the under-doped regime
3. the formation of the Mott gap at high energies in approaching the Mott insulator (see top panel of Fig. 8 region marked A).

We can satisfy the first condition by using the self-energy Σ -periodization. The second and third points are instead obtained by using the cumulant \mathcal{M} -periodization, which is able to describe the formation of the antinodal.

In order to combine all these requests, we take advantage from ideas introduced in phenomenological Fermi-liquid Boltzmann approaches to the normal-state transport properties of cuprate superconducting materials^{48,62,63,64}. We base in particular on the work of ref.⁴⁸, where the division of momentum space in nodal Fermi-liquid-like regions, *cold spots*, and antinodal insulator-like regions, *hot spots*, was achieved by projecting the quasiparticle scattering operator $C_{kk'}$ on a basis of patches $\{\phi_\alpha\}$ in momentum space with different temperature scattering-dependencies:

$$C_{kk'} = \sum_{\alpha\beta} \phi_\alpha(k) C_{\alpha\beta}(T) \phi_\beta(k) \quad (35)$$

In this case, it is possible to solve exactly the Boltzmann equation for the simple case of two patches (one marking the nodal and the other the antinodal region). The shape and the scattering properties of the cold patch (modeled by a small set of parameters) was fixed by obtaining the

best fit on few transport quantities (resistivity, Hall coefficient), and a systematic correspondence with others transport quantities (magnetoresistance and thermoelectric power) was then obtained. For comparison, the nodal patch Φ_k used in ref.⁴⁸ is shown in the left hand side of Fig. 15 (the antinodal patch is simply defined as $1 - \Phi_k$).

In the same spirit, we introduce here a mixed periodization-scheme, by projecting the lattice self-energy $\Sigma_k(\omega)$ on a nodal $\Phi(k, \omega)$ and an antinodal $1 - \Phi(k, \omega)$ patch in momentum space:

$$\Sigma_k(\omega) = \Phi(k, \omega)\Sigma_k(\omega)[\hat{\Sigma}] + [1 - \Phi(k, \omega)]\Sigma_k(\omega)[\hat{\mathcal{M}}] \quad (36)$$

where $\Sigma_k(\omega)[\hat{\Sigma}]$ is obtained by periodization of the cluster Σ and $\Sigma_k(\omega)[\hat{\mathcal{M}}]$ by periodization of the cluster cumulant \mathcal{M} (eq. 26). The patch $\Phi(k, \omega)$ separates the Σ -periodized from the \mathcal{M} -periodized regions (right hand side of Fig. 15). For convenience's sake, we choose a form with k and ω separable:

$$\begin{aligned} \Phi(k, \omega) &= \Psi(k)\Psi(\omega) \\ \Psi(\alpha) &= \frac{1}{2} [1 - \tanh(\beta_\alpha r_\alpha)] \end{aligned} \quad (37)$$

where r_α is the distance from the a center in k or ω space:

$$\begin{aligned} r_k &= \sqrt{(k_x - k_{x_c})^2 + (k_y - k_{y_c})^2} - r_o(\theta) \\ r_\omega &= |\omega| - \omega_o \end{aligned} \quad (38)$$

Here $(k_{x_c}, k_{y_c}) \sim (\frac{\pi}{2}, \frac{\pi}{2})$, $r_o(\theta) = r_o e^{-(\theta - \frac{\pi}{4})/\sigma_o}$ and $\theta = \arctan(k_y/k_x)$ can be chosen to properly shape the patch. We fix through all the rest of the paper $\omega_o \sim 0.5t$, $\beta_k \sim 100$ and $\beta_\omega \sim 15$, which smooth the boundaries of the patch. It remains to fix the parameters \mathbf{k}_c , r_o and σ_o , which have to be chosen to mimic the phenomenological patch of Fig. 15. There is of course a good degree of arbitrariness in its form. We want however to have a first order qualitative description of the physical properties in momentum space, with the aim to address consideration that are only slightly dependent on the exact form of the patch.

A. Evolution of the Fermi Surface

In order to fix the dimension of the patch $\Psi(k)$ in k -space it is useful to follow the evolution of the Fermi surface in approaching the Mott insulator with the two periodization schemes Σ and \mathcal{M} , as shown in the panels of Fig. 16. At high doping (in our case $\delta = 0.13$) all the system is well described by a Fermi liquid, the self-energy is mostly local, the Σ - (green dash line on the left top panel of Fig. 16) and \mathcal{M} - (blue continues line on the left top panel of Fig. 16) periodizations give in practice the same result. We can choose to describe the system with the Σ -periodization and $\Psi(k)$ covering all the k -space (for example see the left panel of Fig. 17 for $\delta = 0.13$, where the patch is marked by the gray region

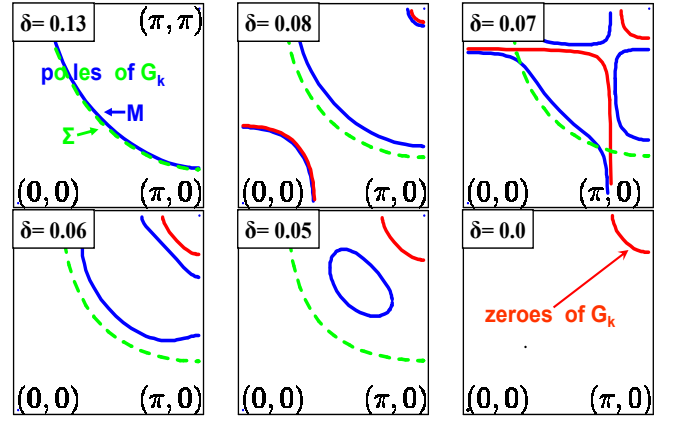


FIG. 16: (Color online). We show the evolution of the normal-component Fermi surface (blue continuous line in the \mathcal{M} -periodization scheme, green dashed line in the Σ -periodization scheme), defined as $\xi_k + \text{Re } \Sigma_k = 0$ in eq. 19. Panels span from the over-doped region ($\delta = 0.13$ top-left panel) to the Mott insulator ($\delta = 0.0$ bottom-right panel). **By periodizing the cumulant \mathcal{M}** , the Fermi surface disappears in the insulating state and it is replaced by a line of zeroes of G_k (red lines). The way this takes place is via a topological phase transition around $\delta_p \sim 0.06 < \delta < \delta_c \sim 0.08$, from a large hole-like Fermi surface to a pocket-like Fermi surface. The low doping region is marked by a phase where Fermi surface and lines of zeroes co-exists. This gives origin to the pseudogap and the fragmentation of the Fermi arcs in measures of spectra of the normal state system (see e.g. Fig. 18). **By periodizing the self-energy Σ** instead, by construction, the lines of zeroes cannot appear. The pseudogap is realized only through a modulation of the spectral intensity along the Fermi surface line, which extends always on all the Brillouin Zone (see also Fig. 18).

covering all the quadrant). By reducing doping, however, the off-diagonal components of the cluster self-energy $\hat{\Sigma}$ are not negligible anymore, and the two periodizations produce different results. In particular, as we stressed in the previous sections, doping $\delta_c \sim 0.08$ and $\delta_p \sim 0.06$ are special points. In the \mathcal{M} -periodization the Fermi surface shows a striking topological phase transition, produced by the appearance of lines of zeroes of the Green's function $G_k(\omega \rightarrow 0)$ at the Fermi level (marked by a continuous red line in Fig. 16). The effect of the appearance of the lines of zeroes of the Green's function is at the origin of the opening of a pseudogap in the spectral function close to the $(0, \pi) - (\pi, \pi)$ and $(\pi, 0) - (\pi, \pi)$ sides of the first quadrant in the Brillouin zone (as shown for example in panel C of Fig. 9). In the Σ -periodization instead a more continuous evolution of the original high-doping Fermi surface (green dashed line) takes place at all dopings up to the Mott insulating state, where it disappears. We notice however that the doping δ_c still marks a change in the curvature of the Fermi surface (even if with the Σ periodization the effect is more difficult to be noticed at naked eye), as evidenced in the downturn of the k_{nod} vec-

tor as a function of doping in panel A of Fig. 9. This effect was first noticed in ref.²⁶, where we show that the result of periodizing Σ produces a Fermi surface which enhances its hole-like curvature while reducing doping (and the spectral weight reduces too with respect to the nodal point). This goes in the direction of forming a hole pocket, which however never arrives to be created within the Σ -periodization. Within the \mathcal{M} scheme instead, the Fermi pocket forms at low doping and its progressive reduction in approaching the Mott transition describes the way the Fermi surface disappears. In the Mott insulating state Fermi lines have of course totally disappeared, but a line of zeroes of G_k (i.e. a line of divergent self-energy $\Sigma_k^{nor}(\omega = 0)$) remains (in red) close to the corner $k = (\pi, \pi)$ of the first quadrant of the Brillouin Zone.

It is very difficult to state how close to the real solution one or the other of the two descriptions are. Particular intriguing is the \mathcal{M} periodization result. Not only it well portrays the pseudogap in anti-nodes, it also produces, together with the Fermi surface, lines of zeroes of G_k . In this way it describes a continuity from the Fermi liquid at high doping (where only the Fermi surface is present) to the Mott insulating state (where only lines of zeroes are present). To this respect, it is clear that the Σ periodization scheme fails in describing the Mott state, as it is unable by construction to build up lines of zeroes. Within our analysis however, we cannot claim that in the real physical system a Fermi pocket, together with lines of zeros, is actually present. Recent experiments on cuprate systems, where it has been possible to induce a low temperature normal state by the application of an external magnetic field, have actually observed de Haas-van Alphen oscillations compatible with a Fermi pocket picture⁷⁹. Hall resistivity measures, extracted at low temperature by suppressing superconductivity with the application of an external magnetic field^{80,81,82}, are also compatible with the scenario of a topological phase transition of the Fermi surface. Our results are also in strong resemblance with the theoretical study of ref.⁷⁵, where similar conclusions on the evolution of the Fermi surface and the appearance of lines of zeroes have been drawn starting from an ad hoc model for the doping-driven Mott insulator transition in two dimensions. Other non-perturbative microscopic approaches have drawn conclusions in similar directions (see e.g. ref.^{83,84}). There are however some caveats in concerning the hole pocket which have to be considered.

In first place, according to the generalized Luttinger theorem^{67,85,86,87} the volume enclosed between the Fermi surface and the line of zeroes (if present) should be equal to the particle density $n = 1 - \delta$. This theorem is quite respected (but not so much at low doping) by the Fermi surface derived with the Σ -periodization (green dashed line of Fig. 16). It is not clearly obeyed instead at low doping by \mathcal{M} -periodization, as evident e.g. by looking at the area enclosed between the Fermi pocket (blue line) and the lines of zeroes (red line) in the panel $\delta = 0.05$ of Fig. 16 (close to half-filling the volume which gives the correct

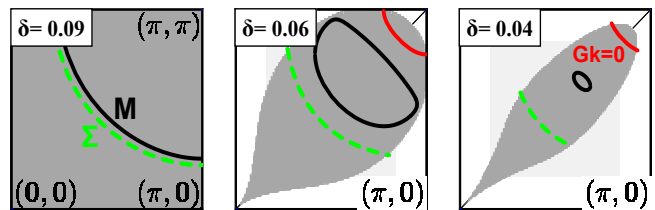


FIG. 17: (Color online). The dimension of the patch Ψ_k in momentum space (gray shaded region) is determined in such a way that the \mathcal{M} -Fermi surface (black line) is cut away and replaced by the Σ -Fermi surface (dashed green line). The red line are where the self-energy Σ_k is diverging and $G_k = 0$.

density should be half of the quadrant). Far from stating that the system is violating Luttinger theorem (which in strongly correlated system is actually a possibility^{38,88}), this effect is likely an artifact coming from the truncated Fourier expansion in eq. 20, which can be improved only by increasing the cluster size. A possible scenario is that in real systems the line of zeroes is closer to the zone diagonal which goes from $(0, \pi) \rightarrow (\pi, 0)$, as actually we find at half-filling for a chemical potential value in the middle of the Mott gap $\mu \sim U/2$ (the panel displayed in Fig. 16 has a chemical potential close to the Mott gap edge $\mu \sim U/2 - \Delta_M/2$, where Δ_M is the total Mott gap). This is in fact what was proposed in ref.⁷⁵ as starting hypothesis. In this way, the side of the hole-pocket facing the (π, π) corner point is "cancelled" by the proximity of the lines of zeroes (see for example the spectral functions of Fig. 17), and the resulting picture is a Fermi arc in the nodal region, which is replaced by a lines of zeroes in the antinodal regions.

In second place, the discussion we have previously carried out (see Fig. 8 in section III and the description of nodal properties in section IV) shows that the low energy nodal point is better portrayed by periodizing Σ , i.e. at the nodal point we rather have a Fermi arc more than a pocket. This is important if the nodal point properties (presented in the previous sections III and IV) have to be well portrayed. The real solution result at the nodes is likely to lay in between the \mathcal{M} and Σ periodization schemes.

B. The choice of the patch shape

In line with the discussion above, we choose therefore to assign to the nodal region the path Ψ_k , which uses the Σ periodization. The rest of the k -space (covered by $1 - \Psi_k$) is described with the \mathcal{M} periodization. By following this criterion we establish the evolution of $\Psi(k)$ with doping, as shown in Fig. 17. The size and shape of the patch Ψ_k is determined so that the \mathcal{M} Fermi surface is cut away, and the only piece of Fermi surface inside Ψ_k is the one produced by periodizing Σ (green dashed line). By reducing doping δ the size of the patch Ψ_k

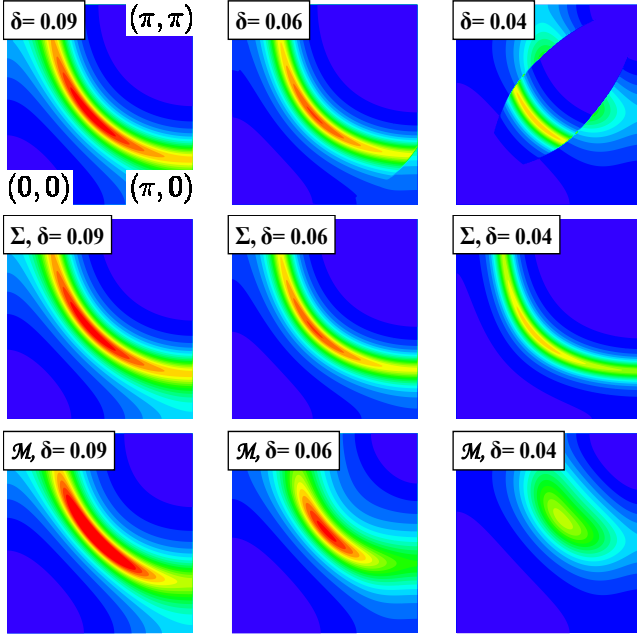


FIG. 18: (Color online). The spectral function $-\frac{1}{\pi}\text{Im}G_k(\omega \rightarrow 0)$ in the first quadrant of the Brillouin Zone obtained with the mixed periodization (top row) is confronted with one obtained from the self-energy (Σ) and the cumulant (\mathcal{M}) periodizations (second and third row from the top). The broadening $\eta = 0.052$, the color scale $x = 0.5$ (see appendix A for details).

progressively reduces, until possibly disappearing in the Mott insulating state ($\delta = 0$) where only the \mathcal{M} -scheme reproduces well the gapped spectra. We have fixed the center of Ψ_k by choosing $(k_{x_c}, k_{y_c}) = (k_{x_{nod}}, k_{y_{nod}})$, the momentum coordinate of the nodal point described in panel A of Fig. 9. A complete description of the patch parameters r_o and σ_o (see formula 37) as a function of doping is given in the following table:

δ	>0.08	0.08	0.06	0.055	0.05	0.04	0.03
r_o	3.00	2.20	2.20	2.20	2.20	2.20	2.20
σ_o	$\pi/2$	$\pi/2.4$	$\pi/2.8$	$\pi/5$	$\pi/8$	$\pi/12$	$\pi/16$

We notice that with the choice of this patch most of the lines of zeroes disappear from the quadrant the Fermi level. As mentioned above, we are not able to make definitive statement about the actual position of these lines of zeroes. If it were closer to the quadrant diagonal (as conjecture in work⁷⁵), they would re-appear in the $1 - \Psi_k$ region of momentum space, which is described by the cumulant. As stressed in the previous subsection, this would be important if one want to respect the Luttinger theorem on the particle counting. In this mixed periodization used for the 2×2 plaquette result however this does not take place. We remark however that in the $1 - \Psi_k$ region scattering rate (i.e. self-energy) is very high (similarly to the results in ref.⁸⁴), and this fact is ultimately the reason for the appearance of a pseudogap,

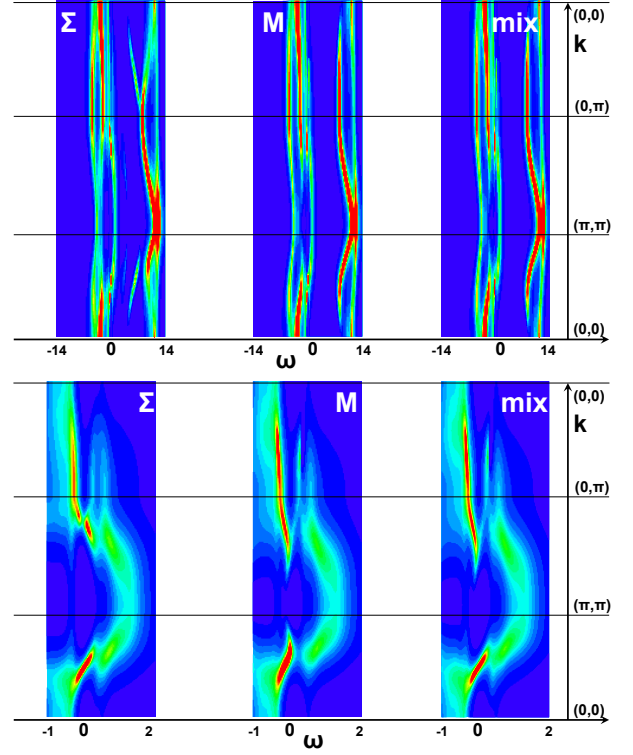


FIG. 19: (Color online). Comparison between the Σ -periodization scheme, the cumulant \mathcal{M} -periodization scheme and the mixed-periodization scheme for a low doped system $\delta = 0.05$. On the top row we show the full energy range $-14 < \omega < 14$ covering the lower Hubbard and upper Hubbard bands. The gross features are very similar. Notice the Σ -scheme introduces fake density of states in the Mott Hubbard gap. In the bottom row we show a close up at low energy $-1 < \omega < 2$, where the methods are most different. The mixed scheme is constructed to retain a Σ -periodization character close to the nodal region $k \sim (\frac{\pi}{2}, \frac{\pi}{2})$ and a \mathcal{M} -periodization character in the antinodal region $k \sim (0, \pi)$. Spectral functions are displayed by introducing a ω dependent broadening $i\eta(\omega)$ and the maximal color scale value are $x = 0.20[0.25]$ for the top [bottom] panel (see appendix A).

whether or not the lines zeroes are effectively present. The division of the k -space via the patch Ψ_k is surely artificial, and it has not pretext of describing in detail the real properties of the system. It has however capable of capturing in a unique scheme either the virtues of the Σ -periodization (above all in the nodes) and of the \mathcal{M} -periodization (above all in the anti-nodes), which portray with some good degree of confidence the physical properties in different regions of momentum space (as we discussed in the previous sections).

A confront between the Σ , \mathcal{M} and mixed periodizations is presented in Fig. 18 and Fig. 19. In Fig. 18 we show the spectral density $A(k, \omega) = \frac{1}{\pi}\text{Im}G_k^{nor}(\omega \rightarrow 0)$ in the first quadrant of the Brillouin Zone for decreasing doping δ (from left to right). The mixed-periodization scheme (top row) is confronted with the Σ and \mathcal{M} pe-

riodizations (bottom rows), showing how the patch Ψ_k is interlacing them. The well known phenomenon of the Fermi arc breakup^{12,13} is reasonably well described by all methods, showing this is a solid result of CDMFT. Moreover, the similarity with spectra calculated in previous CDMFT work on the normal state^{36,47} shows the smooth continuity between the normal component spectra of this superconducting state solution with the spectra of a normal state result. In Fig. 19 we show the band spectrum $A(k, \omega)$ plotted as a function of the energy ω along the path $(0,0) \rightarrow (\pi, \pi) \rightarrow (0, \pi) \rightarrow (0,0)$ in the first quadrant of the Brillouin Zone. In the top panel we confront the full energy range $-14 < \omega < 14$ covering upper Hubbard band and lower Hubbard band. At this energy resolution the three schemes are qualitatively very similar. We just stress that the Σ -periodization artificially introduces spectral weight in the Mott gap (as discussed in Fig. 8 and evident in the figure around $\omega \sim 3 - 7t$). This justify the choice of cutting the patch $\Psi(\omega)$ at low energies $\omega \leq 0.5t$, using the \mathcal{M} -periodization in the remaining of the energy range. In the bottom panel of Fig.(16) we show a close up at low energy ($-1 < \omega < 2$). In this energy range the methods most differ, however the qualitative results are still very similar. In particular the mixed scheme has been designed to well describe a Fermi liquid linear dispersion at the node, and the right description of the Mott gap, especially in the antinodal region. In the analysis of the following sections we will therefore apply the mixed scheme introduced here through formula 36 to periodize the normal component of the self-energy (while the anomalous component $\Sigma_{ano}(\omega)$ is always obtained through formula 24, implying by construction a d-wave shape of the superconducting gap).

C. Local density of state with the mixed scheme

We use now the mixed periodization to re-calculate the local density of states $N(\omega) = -\frac{1}{\pi} \sum_k \text{Im} G_k(\omega)$ at low energy, beyond the cluster energy resolution (which is due to the finite dimension of the truncated Anderson impurity model used to implement CDMFT, see Fig. 6). As widely explained above, this relies on the implicit assumption that the superconducting gap has a d-wave form (see eq. 24) and at the node we have a well defined Fermi liquid arc. The result is shown in Fig. 20. A "V-shaped" $N(\omega)$ is observed either in the over-doped and under-doped regions. Coming from the over-doped side towards the under-doped side, the slope is always decreasing, until reaching a saturating value at the small doping (until eventually showing a small up-turn for the smaller doping, see Fig. 12). The slopes well fit the analytical value extracted at low energy in formula 32. On a wide range of energy ($-1 < \omega < 1$), the V-shape is quite symmetric in the over-doped region $\delta \geq \delta_c \sim 0.08$ (as already remarked in the CTQMC-CDMFT study of ref.⁴¹). Spectra become strongly asymmetric in the under-doped region ($\delta \leq \delta_p \sim 0.06$), when the pseudogap in the nor-

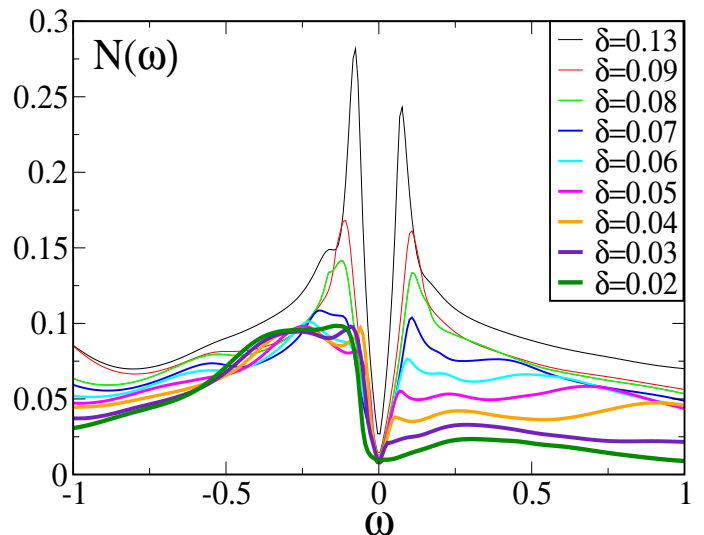


FIG. 20: (Color online). Local density of states $N(\omega)$ as a function of the doping obtained with the mixed-periodization scheme. The V-shape at $\omega \rightarrow 0$ is expected from a d-wave superconductor with nodal Fermi liquid quasiparticles. For doping $\delta < \delta_p \sim 0.6$ spectra develop a marked asymmetry. This result interprets the cluster result of Fig. 6 and it is in good agreement with scanning tunneling experiments (see e.g. ref.⁵³). The display on the real axis of the Green's function has been obtained by introducing a ω -dependent broadening $i\eta(\omega)$ (see appendix A for details).

mal part of the system opens and super-impose to the superconducting gap (as commented in panel D of Fig. 9). The qualitative behavior of these curves should be compared with the raw cluster result of Fig. 6. The periodizing mixed scheme we introduced should be considered as the best fit we could achieve to our cluster DMFT results, basing on few reasonable solid assumptions on the physical properties of the system (like the d-wave superconducting gap, the pseudogap formation, the Fermi liquid properties at the node). This allows us to recover a momentum dependent Green's function and access physical quantities comparable to experimental results on cuprates. The qualitative behaviour of $N(\omega)$ we determined well portrays in fact results of scanning tunneling experimental⁵³, and it supports a comparison in momentum space.

VI. QUASIPARTICLE SPECTRA FROM THE SUPERCONDUCTOR TO THE INSULATOR.

In this section we use the mixed-periodization scheme and derive a detailed description of the connection between the spectra of the Mott insulator and the superconductor by varying doping.

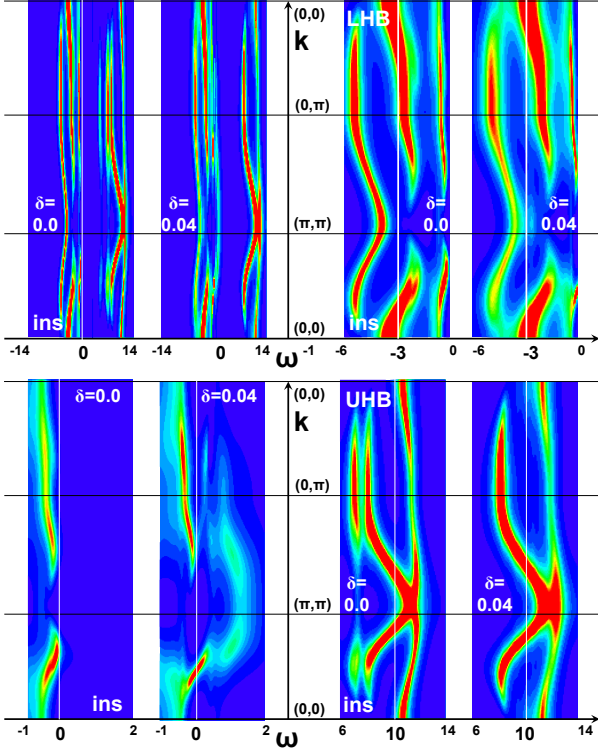


FIG. 21: (Color online). Band dispersion $A(k, \omega)$ along the path $(0,0) \rightarrow (\pi, \pi) \rightarrow (0, \pi) \rightarrow (0,0)$ in the first quadrant of the Brillouin Zone. The Mott-insulating state ($\delta = 0$) is confronted with a small doping ($\delta = 0.04$) state. **Top-left** corner: the full range of energies ($-15 < \omega < 15$) covered by the one-particle spectrum is displayed. The gross band-structure, displaying a lower Hubbard band (LHB) ($-6 < \omega < 0$) and an upper band (UHB) ($10 < \omega < 15$) separated by a Mott gap ($0 < \omega < 10$) remains un-changed in going from the insulator into the metal. **Top-right** corner: detail of the LHB, which rigidly shifts in going from the insulating to the metallic state. **Bottom-left** corner: detail of the low energy ($-1 < \omega < 2$) feature. In going into the metallic state, the shift of the bands is not rigid and spectral weight appears at positive energy as soon as doping is added into the system. **Bottom-right** corner: detail of the UHB. Upon doping, a rigid shift in the metallic state is accompanied by a transfer of spectral weight to low energies. The color scale maximum value is always $x = 0.20$, except for the lower left panel, where it is set $x = 0.25$. We refer to appendix A for the choice of the broadening $\eta(\omega)$.

A. Doping a Mott insulator

To this purpose, we analyze in Fig. 21 the spectral functions, $A(k, \omega) = -\frac{1}{\pi} \text{Im} G(k, \omega)$ in the $\omega - k$ space, along the k -path $(0,0) \rightarrow (\pi, \pi) \rightarrow (0, \pi) \rightarrow (0,0)$ in the first quadrant of the Brillouin zone. We compare the insulating state ($\delta = 0$) with a slightly doped state ($\delta = 0.04$). In the left top panel we display a wide energy-range $-14 < \omega < 14$, which covers the lower (LHB) and upper (UHB) Hubbard bands. We notice

that, upon adding a small doping, the gross structure of the lower Hubbard band ($-6 < \omega < 0$) and the upper band ($10 < \omega < 15$), which are separated by a Mott gap ($0 < \omega < 10$), remains substantially un-changed. A detail of the lower Hubbard band, a closeup of the Fermi level ($-1 < \omega < 2$) and a detail of the upper Hubbard band are presented in the right top, left bottom, right bottom panels respectively. The LHB (top right) rigidly shifts in going from the insulating to the metallic state, losing spectral intensity, which goes to build up quasiparticles at the Fermi level $\omega = 0$ (bottom left). The novel outcome from the CDMFT calculation, as compared with the single-site DMFT⁵, consists in the anisotropic fashion quasiparticles first occupy the Fermi level in momentum space. This is better seen in a closeup of the band dispersion around the Fermi level (bottom left). The region where firstly quasiparticles appear is close to $k = (\frac{\pi}{2}, \frac{\pi}{2})$. In fact, already in the insulating state ($\delta = 0$), we observe that around $k = (\frac{\pi}{2}, \frac{\pi}{2})$ a heavy-particle hook-shaped band is closest to the $\omega = 0$ level, while in the proximity of $k = (0, \pi)$ there is a "pseudogap" and the band disperses at negative energies. This kind of band-structure survives upon doping, as we can observe in the $\delta = 0.04$ panel. Contrary to the Hubbard bands, however, the low-energy band does not shift rigidly as doping is added to the insulator, rather it stays pinned at the Fermi level, and the shifts in frequency is only a small fraction of the changing in chemical potential. We also observe the appearance of spectral weight at positive energy, coming from both the LHB and UHB, which starts building up a full Fermi-liquid-like band, as we show more in detail in the following. In the bottom right corner of Fig. 21 we finally show the UHB. In this case a rigid shift in the metallic state is accompanied by a strong reduction of spectral weight. In fact, according to our result, the UHB narrows with respect to the insulating state.

B. Approaching the Mott insulator from the over-doped side

We start now from the viewpoint of the highly doped system and observe how the approach to the Mott insulator affects the electronic structure of the superconducting state. The high-doping system offers the advantage of having more standard Fermi-liquid-like properties (the patch $\Psi(k)$ introduced in the previous section covers all the momentum space). In Fig. 22 we show the electronic band $A(k, \omega)$ in the $k - \omega$ space, once again in the path $(0,0) \rightarrow (\pi, \pi) \rightarrow (0, \pi) \rightarrow (0,0)$ of the first quadrant of the Brillouin zone, on the full energy-range $10 < \omega < 15$ covering the LHB and UHB. Here we want to display the evolution from high doping (left) to small doping (right). At high a doping $\delta = 0.13$ a Mott Hubbard gap which separates a LHB structure from the UHB is already visible. A narrow but Fermi Liquid-like band is however present, and it crosses the Fermi level either

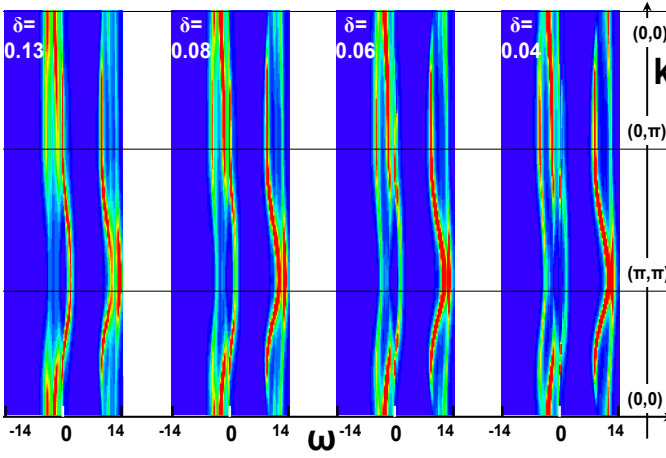


FIG. 22: (Color online). Evolution of the one-particle spectrum from the over-doped (left side, $\delta = 0.13$) to the under-doped (right side, $\delta = 0.04$) state. The typical Fermi-liquid band, well visible in a narrow energy range ($-1 < \omega < 1$) around the Fermi level at high doping $\delta = 0.13$, is progressively destroyed by reducing doping, while the upper and lower Hubbard bands build up acquiring spectral weight. These features are shown in detail in Figures 23 and 24. The color scale maximum value is $x = 0.20$ and we refer to appendix A for the choice of the broadening $i\eta(\omega)$.

in the region of momentum-space around $k = (\frac{\pi}{2}, \frac{\pi}{2})$ and $k = (0, \pi)$ (see also Fig. 24). Reducing the doping δ , we see that this narrow band loses intensity more and more (follow the horizontal line at $k = (\pi, \pi)$ in $\omega \sim 0$) to the advantage of the Hubbard bands, which instead gain spectral weight in approaching the Mott insulator. To have a glance on how this is taking place we look in the following figures at the different energy-regions of the band in further detail.

Fig. 23 shows the UHB and the LHB in detail. The statements made above are confirmed: both Hubbard bands gain spectral weight in decreasing doping, mainly in the region of momentum space close to the anti-nodes $k \sim (0, \pi)$ (follow once again the horizontal line), while rigidly shifting with respect to the change of chemical potential $\Delta\mu$ (one can actually show that the shift of the bands in energy is equal to $\Delta\mu$). The behavior of the Hubbard bands is therefore in agreement with a picture describing the approach to the Mott insulator as a rigidly moving bands, which transfer part of their weight to low energy. As mentioned in the previous subsection, the novelty of our CDMFT result in finite dimension, with respect to the standard vision of the Mott transition given by single-site DMFT in infinite dimension, is that this transfer of spectral weight takes place in a very anisotropic fashion, with the antinodal regions $k \sim (0, \pi)$ getting insulating before the nodal ones.

A closer look to the behavior at low energy, Fig. 24, reveals much richer phenomena taking place. In the top panel we show the spectra resulting from the one-particle

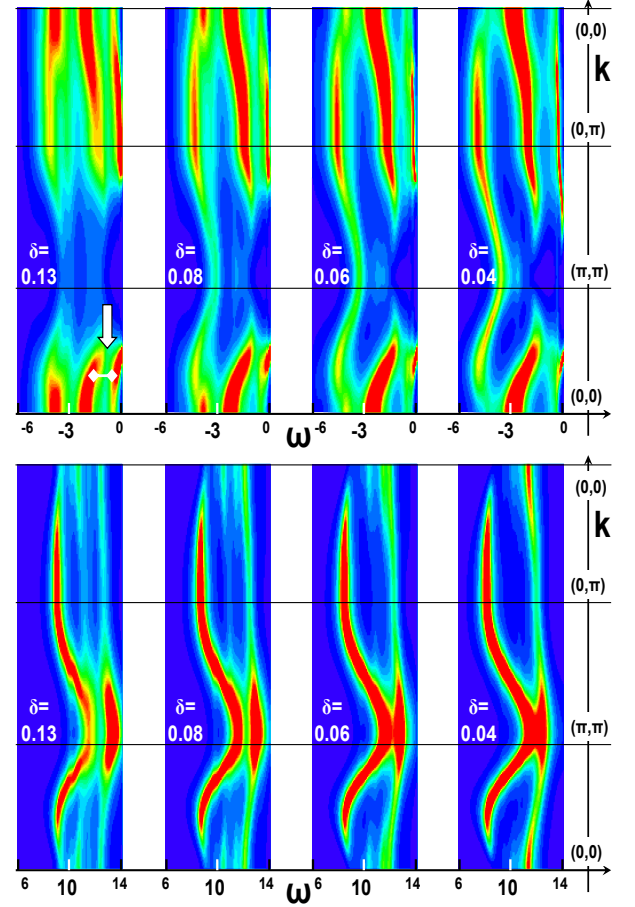


FIG. 23: (Color online). **Top panel:** Evolution of the LHB (top) from the over-doped (left side, $\delta = 0.13$) to the under-doped (right side, $\delta = 0.04$) state. The LHB rigidly shift according to the change in chemical potential by reducing doping, acquiring structure (follow the horizontal line at $k \sim (0, \pi)$). **Bottom panel:** Evolution of the UHB from the over-doped (left side, $\delta = 0.13$) to the under-doped (right side, $\delta = 0.04$) state. The UHB rigidly shift according to the change in chemical potential by reducing doping and, as evident in the color intensity, it gains spectral weight. The color scale maximum value is $x = 0.20$ and we refer to appendix A for the choice of the broadening $i\eta(\omega)$.

Green's function $G_{11}(k, \omega)$ (eq. 19) in the superconducting state. First of all, contrary to the behaviour of the Hubbard bands, the low energy part of the band does not shift proportionally to $\Delta\mu$, in agreement with the observation already made in Fig. 21. The Fermi-liquid-like band at high doping (left side, $\delta = 0.13$) is progressively destroyed by decreasing doping (with progressive reduction of spectral weight in the arc at $0 < \omega < 2$). In the region close to $k = (0, \pi)$ instead, the d-wave superconducting-state opens a gap by removing spectral weight from positive and negative energies (a Bogoliubov band is formed at $\omega > 0$). As widely discussed in the previous sections however, the presence of lines of zeroes

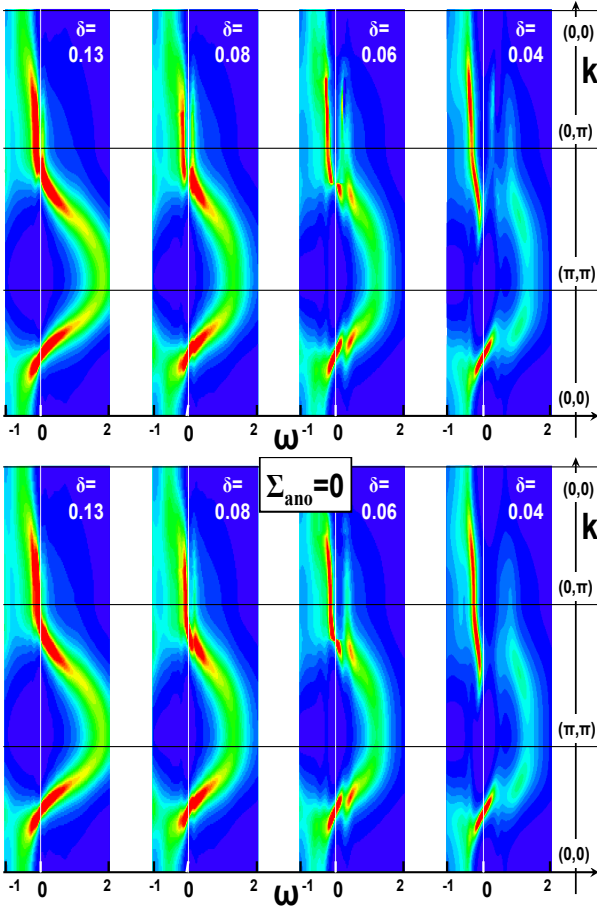


FIG. 24: (Color online). **Top panel:** we show the evolution of the low-energy one-particle spectral band from the over-doped (left side, $\delta = 0.13$) to the under-doped (right side, $\delta = 0.04$) state. A Fermi-liquid-like band at high doping (left side, $\delta = 0.13$) is progressively destroyed by decreasing doping. Around the region $k = (\frac{\pi}{2}, \frac{\pi}{2})$ the dispersion presents a Fermi liquid quasiparticle crossing the Fermi Level. Around the region $k = (0, \pi)$, the d-wave superconducting-state opens a gap by removing spectral weight from the Fermi level to positive and negative energies. **Bottom panel:** we show the contribution to the low energy band coming from the normal component of the system (we set the anomalous self-energy $\Sigma_{ano} = 0$). In particular we observe that in the under-doped side ($\delta \leq 0.08$) a gap (the pseudogap) opens in the $k = (0, \pi)$ region even if the superconductive term is absent. For convenience's sake, the color scale maximum value is set $x = 0.30$ for $\delta = 0.13$ and $x = 0.25$ for all the other doping values. We refer to appendix A for the choice of the broadening $i\eta(\omega)$.

in the Green's function kicks in the under-doped region ($\delta < 0.08$), opening a pseudogap in the normal component of $G_{11}(k, \omega)$ around $k = (0, \pi)$. This is shown in the bottom row of Fig. 24, where the same panels of the top row are reproduced by imposing the anomalous self-energy identically zero $\Sigma_{ano} = 0$ in eq. 19. Switching off superconductivity has in general little effect on the quasiparticle bands, except indeed close to the antinodal point

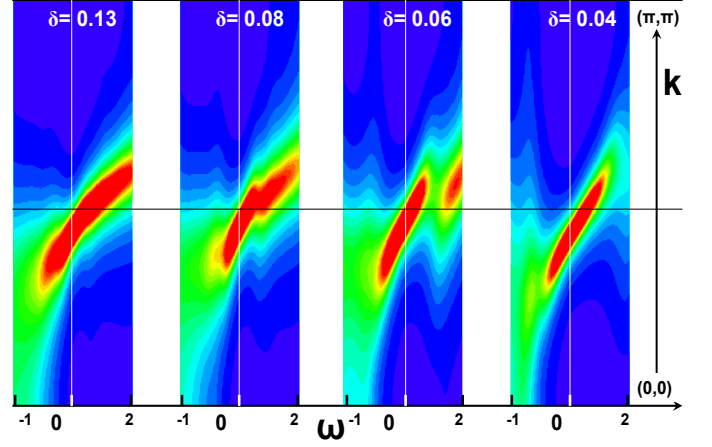


FIG. 25: (Color online). The low energy kink-feature in the spectral intensity at the nodal point for various values of doping. For convenience's sake, the color scale maximum value is set $x = 0.35$ for $\delta = 0.13$ and $x = 0.30$ for all the other doping values. We refer to appendix A for the choice of the broadening $i\eta(\omega)$.

$k \sim (0, \pi)$ and close to the Fermi level $\omega \sim 0$ (the nodal points $k \sim (\frac{\pi}{2}, \frac{\pi}{2})$) are practically unaffected). The differences are most evident in the over-doped region (see e.g. $\delta \sim 0.13 - 0.08$ close to $k \sim (0, \pi)$), where the superconducting gap has disappeared and the quasiparticle band is reconstructed. The weight in the Bogoliubov branch at $\omega > 0$ also disappears. For $\delta > \delta_c \sim 0.8$ differences are much less evident (above all $\delta \sim 0.04$). A gap is also present in the normal component solution, the structure of the quasiparticle dispersion around $k \sim (0, \pi)$ is very reminiscent of the superconducting solution in the corresponding top row. It seems that in the under-doped region the superconducting gap appears to complete the structure already present in the normal component solution. This indicates that the pseudo-gap appearing in the normal component of the system (and present at temperatures above T_C) and the d-wave superconducting gap are possible answers of the system to the same instability, and they co-exist in the under-doped region (while in the over-doped only the superconducting gap is present). This instability is, in our view, connected to the approach to the Mott transition, and it reflects the anisotropic way chosen by the Hubbard system in two dimension to approach the insulating state: the regions around the anti-nodes $k \sim (0, \pi)$ become insulating (at $\delta = \delta_c \sim 0.08$) before the regions close to the nodes $k \sim (\frac{\pi}{2}, \frac{\pi}{2})$ (which become finally insulating $\delta = 0$).

VII. LOW-ENERGY KINK IN THE QUASIPARTICLE SPECTRA

We can now compare the quasiparticle spectra presented in the previous section with the spectra measured,

e.g. by photo-emission, in cuprate-based systems. Unlike the linear dispersion predicted by simple band calculations, in recent years a series of experiments on the electronic structure of many H-TC superconductor compounds has shown sharp breaks in the dispersion of spectra, "kinks", at binding energies of the order of 50-80 meV^{89,90,91,92,93}. Sudden changes in the quasiparticle velocity were reported by a factor two or more. This break in the dispersion is evident at and away from the d -wave node line, and its magnitude shows doping and temperature dependence. Kinks may provide useful information on the nature of the coupling between electrons and possible single-particle or many-body excitations, which are at the origin of strongly-correlated many-body properties of the system. In H-TC superconductors these feature have been associated either with phonons^{89,90} or spin-fluctuation based^{91,92} pairing mechanisms.

In Fig. 25 the dispersion we observe in the quasiparticle band of our result around $k = (\frac{\pi}{2}, \frac{\pi}{2})$ is similar to the experimentally observed kink (see e.g. ref.⁹⁴). A neat linearly dispersing quasiparticle crosses the Fermi level ($\omega = 0$) in the k - ω plot, but around $\omega \sim -0.2t$, the dispersion suddenly changes in slope and gets more incoherent, as evidenced by the broadening spectra. If we set $t \sim 300\text{meV}$ as order of magnitude, we have that the kink appears at $\omega \sim 60\text{meV}$, in good agreement with the observed experimental energy range. The kink present in a wide range of doping, from the under-doped to the over-doped regime, and its slope is increasing with decreasing doping.

This new energy scale in H-TC superconductors arises the debate on the possible nature of the electron-electron coupling. In order for superconductivity to take place in metals, it is necessary that electrons bind into pairs, which condense in a phase-coherent quantum state. In standard BCS superconductivity, coupling between electrons and phonons (lattice vibrations) drives the formation of the pairs. The existence of the kink low-energy scale, not explicable in band theory calculation, may give an hint on the low-energy nature of the interaction between electrons, and hence help revealing the pairing mechanism of the unconventional H-TC superconductivity. The single-band Hubbard Model studied in this paper does not take into account phonons by construction. Therefore the presence of the kink supports the idea that the origin of these features are indeed purely electronic, in agreement with the DMFT and CDMFT studies of ref.^{95,96}. In Fig. 26 we present the spectral function $A(k, \omega) = -\frac{1}{\pi} \text{Im}G(k, \omega)$ calculated in our theory, confronted with experimental ARPES data taken from ref.⁹⁴. Fig. 26 shows the spectral function $A(k, \omega)$ as a function of the energy ω , along two vertical cuts in the first quadrant of the Brillouin Zone in correspondence of the nodal and antinodal region $(k_{nod}, 0) \sim (\frac{\pi}{2}, 0) \rightarrow (k_{nod}, k_{nod}) \sim (\frac{\pi}{2}, \frac{\pi}{2})$ and $(k_{anod}, 0) \sim (\pi, 0) \rightarrow (k_{anod}, k_{anod}) \sim (\pi, \frac{\pi}{2})$. The system is close to optimal doping $\delta_c \sim 0.08$. In the left column we display the CDMFT calculation, while the right column the experimental data, taken from ref.⁹⁴.

The nodal quasiparticle clearly show a dispersion, that from the Fermi level propagates at negative frequencies until $\omega \sim -0.2t$, where it has a sudden broadening, indicating a strong incoherence. The antinodal quasiparticle shows instead a much flatter dispersion at energy corresponding to the superconductive gap, and the antinodal quasiparticle (which shows to have less weight than the nodal quasiparticle) does not lose much coherence. This plots have a good resemblance with the experimental data on the right column. The comparison between the energy scale of our results in the left $-t < \omega < 0$ and of the experimental data $-300\text{eV} < \omega < 0$ shows also that the esteem we have used $t \sim 300\text{eV}$ is a reasonable order of magnitude.

The same comparison is also presented in the intensity color plot at the bottom of Fig. 26, where the nodal (left side) and the antinodal (right side) dispersion calculated with CDMFT are displayed in the top row, while experimental plots of ref.⁹⁴ are in the bottom row. From these diagrams, it is more evident the quasiparticle-like dispersion in the nodal point, which compares very well to the data from photo-emission. In the photo-emission data however at $\omega \sim -0.075\text{eV}$ the quasiparticle appears loosing coherence (effect marked by the loss of red color that gets yellow) and at the same time the slope of the dispersion changes substantially. In the CDMFT calculation instead, as soon as the quasiparticle loses coherence (around $\omega \sim -0.2t$), the dispersion stops (i.e. is $\omega(k) \sim \text{constant}$), and no spectral weight is present in the region at smaller energy ($\omega < -0.2t$). The kink appears in our result as a "gap" in the ω vs k spectra. A similar phenomenon takes place at higher energies, as marked by an arrow in the top-left panel of Fig. 23, where an evident gap is present in between the low energy band and the lower Hubbard band. This could be possibly associated with the "water-fall" dispersion features recently observed in many cuprate materials (see e.g. ref.^{97,98}) at energies $\sim 350 - 600\text{meV}$, where the same k -vector is marking the dispersion $\omega(k)$ in a rather extensive range of energy. In our calculation this phenomenon is described as a gap in the dispersion. The antinodal point, where the superconducting gap is present, is non-dispersing at low energy (right-bottom side in Fig. 26), and the resemblance of our result with the photo-emission data is rather good.

VIII. THE HALL RESISTIVITY TO DETECT THE TOPOLOGICAL PHASE TRANSITION OF THE FERMI SURFACE

We have shown in section V that in the under-doped region ($\delta < \delta_p \sim 0.06$) a different regime sets in our solution, marked by a topological transition from a large to a small Fermi surface (which reduces to an arc or pocket). The strong reduction of the Fermi surface area should correspond to a strong reduction of the carrier density too. This could be in principle

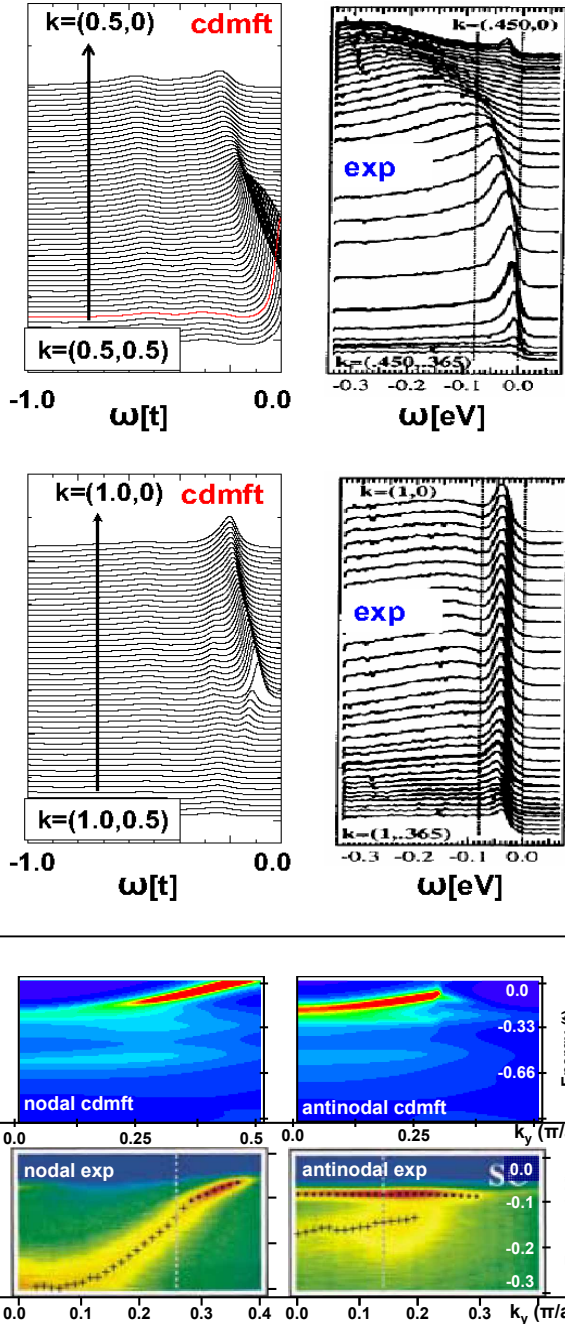


FIG. 26: (Color online). **Top panel:** The low energy spectral intensity $A(k, \omega)$ vs ω calculated within CDMFT (left) is confronted with the experimental result of ref.⁹⁴ in the nodal and antinodal regions. Vertical cuts are traced in k -space close to the node and the antinode, as traced on the figures. \mathbf{k} is expressed in units of (π, π) . **Bottom panel:** Color-intensity plots of the spectral intensity $A(k, \omega)$ in the $k - \omega$ space in the nodal (left) and antinodal (right) cuts of momentum space (the same used in the top panel). The color scale is set $x = 0.30$ (see appendix A). In the bottom row the experimental result of ref.⁹⁴ are displayed for comparison. We refer to appendix A for the choice of the broadening $i\eta(\omega)$.

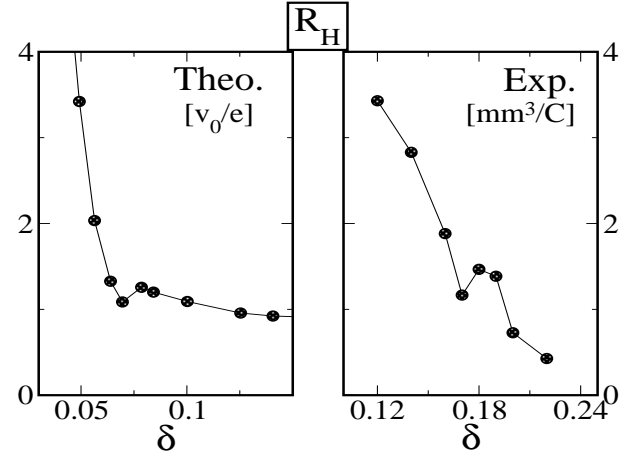


FIG. 27: Hall resistivity R_H as a function of doping δ . The topological phase transition of the Fermi Surface is efficiently detected by a rapid change of the behavior in the Hall resistivity R_H , which indicates a change of the carrier density. **Left:** our theoretical result (units are in the unitary cell volume v_0 over electron charge e). **Right:** the experimental result for *LSCO* extracted from ref.⁸¹.

experimentally detected by measuring the Hall resistivity $R_H = -\frac{1}{n_c e}$, which is directly related to the carrier density n_c , provided superconductivity can be suppressed and the underlying normal liquid extracted. This latter is far from being a trivial procedure, which has many caveats. A standard method is for example to apply a magnetic field, which suppresses superconductivity. Recent publications have addressed this problem in *BSLCO*⁸² ($Bi_2Sr_{1.51}La_{0.49}CuO_{6+\delta}$) and *LSCO*⁸¹ ($La_{2-\delta}Sr_{\delta}CuO_4$), where magnetic field up to 65 Tesla was applied, and in *Nd-LSCO*⁸⁰ ($La_{1.6-x}Nd_{0.4}Sr_xCuO_4$), where more moderate magnetic fields (up to 35 Tesla) can totally suppress superconductivity. The results of these experiences on the Hall resistivity show in fact to be compatible with a reduction of the carrier density at low temperature in an under-doped sample (as we will discuss more in detail in the following).

In our study we can easily estimate the Hall resistivity by using a Boltzmann approach, similarly for example to the phenomenological study of ref.⁴⁸. The Hall resistivity R_H can be expressed in terms of the in-plane conductivity (in the direction of an applied voltage) σ_{xx} and the transverse conductivity σ_{xy} (perpendicular to the applied voltage):

$$R_H = -\frac{\sigma_{xy}}{\sigma_{xx}^2 - \sigma_{xy}^2} \frac{1}{H} \quad (39)$$

where H is the applied field. We can use the low-energy limit (similarly to eq. 30) and extract the normal component of the system (by setting $\Sigma_{ano} = 0$ in eq. 19). The Green's function is conveniently written on the Matsub-

ara axis as:

$$G(k, \omega_n) = \frac{1}{i \frac{(2n-1)\pi}{Z_k \beta} - \zeta_k} \quad (40)$$

where a re-normalized dispersion $\zeta_k = [\xi_k + \text{Re}\Sigma_k(0)]$ and a inverse temperature β^{-1} , re-normalized by the quasiparticle residuum Z_k , are introduced. We consider this liquid as the base on which to start applying a Boltzmann theory. The conductivities can then be expressed in the first order in H (see e.g. ref.⁴⁸):

$$\begin{aligned} \sigma_{xx} &= -2e^2\tau \sum_k (v_k^x)^2 \frac{\partial f(Z_k \zeta_k)}{\partial \zeta_k} \\ \sigma_{xy} &= \frac{2e^3 H \tau^2}{\hbar c} \sum_k v_k^x [v_k^y \partial_{k_x} v_k^y - v_k^x \partial_{k_y} v_k^y] \frac{\partial f(Z_k \zeta_k)}{\partial \zeta_k} \end{aligned} \quad (41)$$

Here, $v_k^\nu = \partial \zeta_k / \partial k_\nu$ is $\nu = x, y$ component of the normal velocity, $f(x) = 1/(e^{\beta x} + 1)$ is the Fermi function, τ is the scattering time, which at $T = 0$ is, for example, given by the impurities, and that, for convenience's sake, in a first order approach, we can hypothesize k -independent. In the pure model, like the Hubbard Model, this term is absent, so we have to add it in order to simulate the finite $T = 0$ resistivity of a real material. As the Hall resistivity R_H is anyway independent of a constant τ , we do not need to make any special further assumption about it.

The Hall resistivity resulting from our calculation implemented via a mixed periodization and plug into the Boltzmann expression is displayed in the left hand side of Fig. 27 as a function of doping δ . The unit used to display R_H is the ratio between the unitary cell volume v_o and the electron charge e . To give an idea of the order of magnitude, taking for *LSCO* (see e.g. ref.⁹⁹) an average lattice spacing $a_o \sim 4\text{\AA} = 4 \times 10^{-7} \text{mm}$ in the $Cu - O_2$ planes, and $a_1 \sim 3a_o$ in the c -axis $\frac{v_o}{e} \sim 1.2 \text{mm}^3/C$, which well compares with the experimental results extracted from ref.⁸¹ (but similar results hold for *BSLCO*⁸²), and presented on the right hand side. In the following, in drawing a parallel between our theoretical result and the experimental data, one should keep in mind that in our study the "optimal doping" (which we can only identify with some degree of uncertainty as a maximum in the order parameter $\delta_c \sim 0.08 < \delta < \delta_p \sim 0.06$, see also the discussion in the conclusions) is situated at a smaller doping than the experimental value $\delta_{opt} \sim 0.17$.

R_H is positive, as expected by the hole-like Fermi surface in the hole-doped system. As, in approaching the Mott insulator, the localization of particles reduces free carriers, R_H is generally expected to monotonically decrease with doping. Two regimes are clearly separable in our result (left side of Fig. 27). At $\delta \sim \delta_p \sim 0.06$ we observe a discontinuity in the behavior of R_H (which slightly decreases instead of increasing), and for $\delta < \delta_p$ a sudden increase of R_H , related to the topological phase transition of the Fermi surface presented in section V,

marks the reduction in the carriers in approaching the Mott state. Such a discontinuity is present and more evident in the experimental data (right side of Fig. 27). The presence of a local minimum at optimal doping $\delta_{opt} \sim 0.17$ represents a crucial point in the results presented in references^{81,82}. This behavior is interpreted in terms of a quantum critical point, associated with a change in the topology from a large hole-like Fermi surface (realized for $\delta > \delta_{opt}$) to a small (pocket-like?) Fermi surface, realized for $\delta < \delta_{opt}$). According to their point of view, the force driving the superconductivity is related to the fluctuations around a critical point. This attractive force could overcome the mutual Coulomb repulsion of electrons, delocalizing and freeing carriers right in proximity of the quantum critical point. This fact would originate the local minimum in the Hall resistivity R_H (which is inversely proportional to the number of free carriers). The critical point would correspond then to the optimal doping δ_{opt} , where the critical temperature T_C is the highest.

Our result shows qualitatively very similar trends, with a minimum (even if milder) just at doping δ_p , where the topological transition of the Fermi surface takes place. This strongly supports the analysis of our results and the conclusion we have derived, in comparison with the experimental evidence on the Hall resistivity.

In our 2×2 plaquette study at $T = 0$, however, we are not unfortunately able to state if δ_p is or not the optimal doping (which is defined at $T = T_C$). This point is as a matter of facts close to the maximum of the d-wave order parameter (as evident in Fig. 1). The study of ref.⁴¹ has pointed out that the exact determination of the optimal doping may depend on temperature. Also, we cannot demonstrate that $\delta_p \sim 0.06$ is a quantum critical point, as we have not clearly identified an order parameter or the divergence, to some order, in the free energy. Our study however finds good agreement with the experimental results of ref.^{80,81,82}, and it is not in contradiction with their conclusions. We can in fact associate the discontinuity of R_H with a dramatic re-arrangement of the electronic structure in the system, corresponding to the topological transformation of the Fermi surface. This happening is marked by a fast crossover region (between $\delta_c \sim 0.08 < \delta < \delta_p \sim 0.06$), where the maximum of order parameter is located, the pseudogap appears (at $\delta \sim \delta_c$), the superconducting gap start decreasing (at $\delta \sim \delta_p$). All these facts have striking consequences on spectra and transport properties, which we have presented throughout the paper.

More developments beyond the 2×2 plaquette CDMFT are needed, in order to be able to reveal if in reality $\delta_c \equiv \delta_p$, or rather they represent two different "transition" points. It would be then important to clarify if any of these points are a quantum critical point, and their exact connection with the optimal doping δ_{opt} of the system. All these are important open questions left for the future studies.

IX. CONCLUSION

A. Comparison with the resonating valence bond mean field theory

CDMFT can be viewed as a generalization of the earlier slave boson resonating valence bond mean field theory^{100,101}. It is therefore useful to put our results in this context. RVB mean field theories had numerous early successes, like the prediction of d-wave superconductivity and a pseudogap phase having the same symmetry as the superconducting state⁵². Both RVB mean field theories and our CDMFT study are formulated in terms of variables defined in a plaquette. The main differences stem from the fact that in CDMFT these variables are frequency dependent, and thus they are able to properly describe coherence to incoherence crossover in the momentum space. In the slave boson RVB mean field theory there are two very important notions. The slave boson order parameter, which measures "Fermi liquid coherence", namely the emergence of a well defined quasiparticle peak in the spectral function, and the "spinon condensation" order parameters, both in the particle-particle and particle-hole channel. The position of the quasiparticle is shifted by a Lagrange multiplier which, adding to the bare chemical potential, forms a quasiparticle chemical potential. The dynamical mean field picture of CDMFT develops these ideas, allowing them to acquire non trivial dependence in momentum space.

To begin with, CDMFT describes naturally a high temperature state showing poor coherence. As discussed in reference²⁶ and Fig. 7, the peaks in the spectral functions in the normal state are broad and incoherent. It is only in the superconducting state that we can, for the first time, extract the Fermi liquid parameters discussed in this work. Coherence appears at low temperature in the nodal region more than in the antinodal region, as it is clearly seen for example Fig. 7. Furthermore the weight of the quasiparticle is different (and larger in most of the phase diagram) in the nodal than in the antinodal region, as seen in Fig. 10. At small doping quasiparticles in the antinodal region cannot be defined in a strict Landau-Fermi liquid sense, as a quasiparticle peak cannot be identified at the Fermi level anymore. As a matter of fact a pseudogap opens in the antinodal quasiparticle spectra. In the nodal region instead, quasiparticles are always well defined and their weight dramatically reduces as the doping is reduced. The slave boson RVB picture describes the pseudogap phase in terms of the formation of spin-singlets, parameterized by two order parameters, one describing correlations in the particle-particle channel and the second in the particle-hole channel. A similar but more complete description is achieved in terms of the dynamical anomalous and normal self-energies. Notice the remarkable fact that the anomalous self-energy at low temperatures and at low frequencies has a similar order of magnitude as the normal self-energy (Fig. 2 and Fig. 5), indicating that, as in the RVB mean field

theory, they might both have a similar singlet-pairing origin deriving from the approach to the Mott insulator. On the other hand, the normal state self-energy has a more complicated angular dependence than the simple harmonic (d-wave) k -dependence of the anomalous self-energy. In this sense, the normal and the anomalous gaps can also be viewed as competing for the same electrons, suggesting that further refinements of CDMFT along the lines of ref.¹⁰² are worth being pursued.

B. The scenario presented by our CDMFT results

While the dynamical frequency dependence introduced by DMFT well describes the low-to-high energy crossover, as well known from the infinite dimensional case⁵, the momentum dependence introduced by a cluster DMFT uncovers a wider spectrum of k -dependent physical phenomena, which turn out fundamental in describing the approach to the Mott transition in two dimensions.

In the first part of the paper (section II) we have presented raw cluster quantities, which are direct output of the CDMFT procedure, but which can be only partially interpreted in physical terms. Nevertheless we have shown that the doping-driven approach to the Mott transition takes place via an intermediate regime (rising after an "optimal doping region" $\delta_c \sim 0.08 > \delta > \delta_p \sim 0.06$), where physical properties depart from the standard picture of a BCS superconductor. In particular we were able to identify two distinct energy-scales, one associated with the anomalous component of the self-energy (see e.g. Fig. 5), the other better enlightened in the local density of states (see Fig. 6), showing different doping dependence. In the low doping regime the local spectra also show a strong asymmetry in ω , as observed in experiments⁵³ and contrary to the expectations from a BCS superconductor.

In order to physically interpret the genuine cluster results, we have restored the lattice translational invariance (broken in the CDMFT procedure) by introducing a periodization scheme. In section III we have justified and compared two possible methods, based on periodization of the cluster self-energy and the cluster cumulant respectively. To this purpose, we have discussed the physical properties of our system, taking advantage from either the cluster results (supported also by the comparison with CDMFT results obtained with QMC impurity-solver methods^{25,41,65}) and experimental observation. We have performed a robust test on our approach by reconstructing the local quantities from the momentum-dependent Green's function $G(k, \omega)$ (see Fig. 20), which show to be not far from the corresponding cluster quantities obtained directly in the impurity model.

By introducing a periodization procedure in momentum-space we were able to analyze our result in terms of experimentally observable quantities in the nodal and antinodal points of momentum space (section IV), making contact with recent spectroscopy

experiments^{54,55}. In particular, we were able to interpret the two energy scale in terms of a pure superconducting gap (dominant in the nodes) co-existing with a normal component gap (related to the pseudogap of the normal state and dominant in the anti-nodal region of momentum space at low doping). We complete in this way the work presented in the short publication of ref.⁴⁴.

We have then extended our procedure to describe in first approximation physical properties in all momentum space (section V). The scenario which results present an under-doped state where electronic structure undergoes a dramatic re-arrangement. We could associate this fact with the appearance of a topological phase transition of the Fermi surface (see e.g. Fig. 16), driven by the appearance in momentum space of lines of diverging self-energy, fingerprints of the Mott physics. While these results may be quantitatively different for different periodizing methods, in terms of a large enhancement of the real part of the self-energies they indicate the same qualitative trends. Enhancement of self-energy Σ_k is most relevant in the cumulant scheme. The formation of a pseudogap in the antinodal region, however, only requires a large value of the self-energy and not a strict divergence (which in any case can only occur at $T = 0$). Based on this physical idea, at finite doping the antinodal region is closer to the Mott insulating phase, while the nodal region is closer to the Fermi liquid state (see the band structure of Fig. 24 and the quasiparticle peaks Fig. 9). We achieve in this way a consistent picture of the evolution of the electronic structure with doping within our formalism.

We were able to explain the strong asymmetry in the local density of states, observed e.g. in scanning tunneling experiments⁵³. We were able to give a complete description of the evolution of electronic spectra with varying doping, comparing the doped state with the Mott insulating one (see section VI). In particular, we have shown that the transfer of spectral weight in approaching the Mott transition takes place in a strongly anisotropic fashion. We have described the behavior of the low energy band close to the Fermi level, which is strongly renormalized by the interaction and progressively destroys by reducing doping, opening first a pseudogap in the antinodal region. This latter appears to be present already in the parent Mott insulator. We have stressed how this phenomenon is connected to the aforementioned lines of diverging self-energy. We have described how, from this underlying structure of the normal component, a d-wave superconducting gap rises. We have also shown (in section VII) how the combination of these effects results in spectra which show "kink" features similar to the ones observed in the electronic dispersion of many photo-emission experiments. Finally we have shown, using a simplified Boltzmann approach, how the rising of the under-doped regime, associated in our study to a topological phase-transition of the Fermi surface, is experimentally detectable from the doping-dependent behavior of transport quantities, like for instance a singularity in

the Hall resistivity. All these properties are comparable with experiments on cuprate materials, and the good agreement we have found supports our study of the evolution with doping of the superconducting state of the Hubbard Model, offering a self-consistent scenario of the approach to the Mott transition in two dimension. This is most relevant in connection with cuprate H-TC superconductors, in which the evolution of the electronic structure with doping (and its relation with H-TC superconductivity) remains a fundamental open question. In particular, in recent times, the issue of two (nodal and antinodal) gaps^{54,55} or one pure d-wave gap^{103,104,105} has been at the center of the experimental and theoretical debate^{56,57,59}. In this contest, our CDMFT results on the simplest electronic model for H-TC materials show a good agreement with the two gaps scenario and, at the same time, with many other electronic properties of cuprates.

An important question left open in our study is to determine the exact nature of the small "transition region" between $\delta_p \sim 0.06$ and $\delta_c \sim 0.08$, where fundamental changes take place in the physical properties of the system, in going from the Fermi-liquid of the over-doped side into the anomalous liquid of the under-doped side of phase diagram. In particular, we have shown that lines of diverging self-energy appear at the Fermi level, a pseudogap opens in the one-particle spectrum and a topological phase transition of the Fermi surface occurs (see Fig. 16). This small region of doping locates, within the numerical precision of our result, the "optimal doping", which we identify as a maximum in the d-wave order parameter (Fig. 1). All these observations point towards indicating a tight connection between the physical happening taking place in this optimal doping region and the H-TC mechanism. We are not able to state within our study if behind lays a quantum critical point (which could provide the binding force for a high critical temperature). This scenario is actually supported by many theories^{106,107,108,109} and experimental studies^{82,110,111}, and it could be that further developments of CDMFT (i.e. increasing cluster size) could reveal that the two points δ_p and δ_c actually coincide. Or two distinct points could be actually present, and one (or both) could have the characteristic of a quantum critical point. To reveal this, the right divergence in any order of the free energy and an order parameter should be clearly identified.

At present it is not possible to demonstrate that our solution will survive in the thermodynamic limit (i.e. in the infinite cluster size limit), in the sense that the real ground-state of the Hubbard Model in two dimensions could be another one of the possible competing instabilities, like, e.g. stripe ordering or antiferromagnetism. The latter, in particular, is expected to be the ground-state close to the Mott insulating state. Within a (dynamical) mean-field approach, however, we can study the pure paramagnetic phase, showing that it is a relevant phase even if it is not the true ground-state of the system. We leave open the physical question of what terms

need eventually to be added in the Hamiltonian in order to make this state a real ground-state. In order to make our first order picture more rigorous, further developments are needed. These should involve the cumulants directly in the self-consistency condition, as proposed for example in ref.^{36,102}, and should exploit the flexibility of CDMFT, which can be formulated in terms of a set of adaptive patches in momentum space (on this line see the recent work¹¹²). These extensions, as well as the use of more powerful solvers, which could allow going beyond a 2×2 cluster, are worth pursuing and are left for future studies.

APPENDIX A: DISPLAYING FUNCTION ON THE REAL AXIS WITH ED-CDMFT

Once the ground-state $|gs\rangle$ of the associate Anderson Impurity Model (eq. 8) has been determined via the Lanczos procedure, it is possible to determine the zero-temperature Green's function via a second Lanczos step (see e.g. the review⁵). To this purpose, one has to take as initial vector $c_\mu^\dagger |gs\rangle$ (μ denoting the generic cluster-site index), and write the ground-state Green's function in a continued-fraction expansion, describing the "particle" and "hole" excitations:

$$G(\omega_n) = G^>(\omega_n) + G^<(\omega_n) \quad (A1)$$

with

$$G^{\alpha=>,<}(\omega_n) = \frac{\langle gs | c_\mu c_\mu^\dagger | gs \rangle}{i\omega_n - a_0^\alpha - \frac{b_1^{\alpha^2}}{i\omega_n - a_1^\alpha - \frac{b_2^{\alpha^2}}{i\omega_n - a_2^\alpha - \dots}}} \quad (A2)$$

The parameters a_j^α and b_j^α ($j = 1 \dots$ number of Lanczos steps, $\alpha = >, <$) output directly from the second Lanczos step¹¹³. In the ED-CDMFT procedure the cluster Green's function and the self-consistency equation 4 are evaluated on the Matsubara axis. This implies introducing a parameter β which determines the grid of Matsubara points $\omega_n = (2n-1)\pi/\beta$, and which plays the role of a fictitious temperature (our solution is however at zero temperature). We can easily analytically continue the Green's functions by replacing in the continued-fraction expansion (eq. A2)

$$i\omega \rightarrow \omega + i\eta \quad (A3)$$

where ω is the real axis frequency and η a small parameter used to display the poles. It is difficult to know *a priori* the smallest value we can assign to η . It depends on the physical problem considered, on the size of the associated Anderson Impurity Problem used in the Lanczos procedure and on the energy resolution imposed in satisfying the self-consistency condition on the Matsubara axis (i.e. the parameter β). A reasonable guess for a lower bound value would be for example $\eta \approx \pi/\beta$. Moreover we expect η to be frequency dependent too.

The Lanczos better determines the ground state of the system, and portrays better low-energy properties. The uncertainty in the ground-state vector $|gs\rangle$ propagates in the determination of the a_j^α and b_j^α coefficients (which is a further Lanczos step), and further propagates in the periodization procedures (section III). The error in the second Lanczos step turns out much bigger at higher frequency, and, if η is chosen too small, this can create enormous errors, even breaking causality (which is instead by construction always satisfied in the impurity solver output, i.e. in the cluster Green's function of eq. 6). A too big value of η results however in a poor resolution, which may hide important features, above all at small energy. In order to be able to display at the same time high and

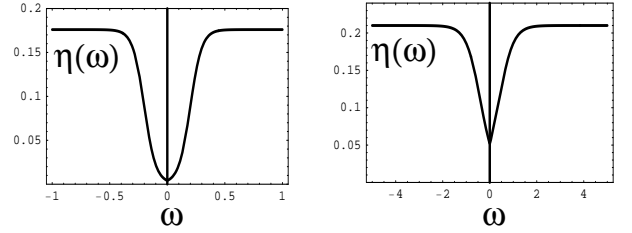


FIG. 28: Example of the broadening $\eta(\omega)$ used to display spectral function on the real axis. **Left:** the low energy range $-1 < \omega < 1$ example of Fig. 20. **Right:** the wide energy range $-14 < \omega < 14$ example of Fig. 19. For a complete list of $\eta(\omega)$ see table A

low energy features, we have introduced for convenience's sake in sections III (with the only exception of Fig. 7, see the corresponding caption), V, VI and VII a ω dependent η , arbitrarily choosing a function-shape which quickly separates a low from a high energy range (see Fig. 28):

$$\eta(\omega) = \eta_0 + \frac{\eta_1}{e^{-|\omega - \omega_0|/T_w} + 1} \quad (A4)$$

The branching between the low and high energy regimes takes place in a Fermi-function-like step at $\omega = \omega_0$ with rapidity $1/T_w$. In Fig. 28 we report as example the $\eta(\omega)$ adopted to display the local density of states of Fig. 20 (on the left), where the low-energy range is $-1 < \omega < 1$, and (on the right) the $\eta(\omega)$ of the density plots of the Fig. 19 and 21, where the full energy scale $-14 < \omega < 14$, including the lower and upper Hubbard bands, is considered. In the following we report exactly the values of the parameters determining $\eta(\omega)$ for all the figures involved:

Figures	η_0	η_1	ω_0	T_w
8, top panel	0.01	0.15	0.05	0.01
8, middle and bottom panels	0.001	0.05	0.05	0.01
19,21,22,23, 24,25	0.01	0.2	0.4	0.3
20	0.001	0.175	0.2	0.05
26	0.025	0.04	0.2	0.025

It is clear that spectral peaks displayed with different $\eta(\omega)$ at different frequency present uncomparable heights and widths. Our task is not however to make this kind of comparison, rather to focalize on the position of the spectral peaks and compare heights and widths at different doping (but at the same frequency). This has to be kept in mind when analyzing these figures.



FIG. 29: Color scale code adopted in displaying the color-density plots. x is the maximum value of the scale.

Finally, the color-code we adopted to display the density-plots (see e.g. figures 19, 21, 22, 23, 24, 25) is shown in Fig. 29. x is the maximum value of the scale, that we have chosen according to the picture (see the corresponding caption). If the value of the function displayed is bigger than x , the color remains red.

APPENDIX B: SUPERCONDUCTING BATH-PARAMETERIZATION WITHIN CDMFT

The general form of the associated cluster-Anderson impurity Hamiltonian \mathcal{H}_{imp} can be written:

$$\begin{aligned} \mathcal{H}_{\text{imp}} = & \sum_{\mu\nu\sigma} E_{\mu\nu\sigma} c_{\mu\sigma}^\dagger c_{\nu\sigma} + U \sum_{\mu} n_{\mu\uparrow} n_{\mu\downarrow} + \\ & + \sum_{k\sigma} \epsilon_{k\sigma} a_{k\sigma}^\dagger a_{k\sigma} + \sum_{k\mu\sigma} V_{k\mu\sigma} a_{k\sigma}^\dagger c_{\mu\sigma} + \text{h.c.} + \\ & + \sum_{k\mu\sigma} V_{k\mu\sigma}^{\text{sup}} a_{k\sigma}^\dagger c_{\mu\bar{\sigma}}^\dagger + \sum_{k\mu\sigma} V_{k\mu\sigma}^{\dagger\text{sup}} c_{\mu\bar{\sigma}} a_{k\sigma} \quad (\text{B1}) \end{aligned}$$

Here $\mu, \nu = 1, \dots, N_c$ label the sites in the cluster and $E_{\mu\nu\sigma}$ represents the hopping and the chemical potential within the cluster. $\epsilon_{k\sigma}$ is the energy level of the (k, σ) orbital in the free electron bath, V s represent the hybridization hopping amplitude either for a particle-destruction/construction and for the singlet-destruction/destruction (construction/construction) between the impurity-cluster and the bath. In order to drive the solutions towards physically interesting regions of the bath-parameters space, we have introduced a reduced bath-parametrization²⁸ which allows to exploit the symmetries in the square lattice to gain a better physical insight of the Green's function symmetries. Moreover using fewer parameters the work required by the minimization procedure is faster and the result simpler to interpret:

$$\begin{aligned} \mathcal{H}_{\text{imp}}^R = & \sum_{\mu\nu\sigma} E_{\mu\nu\sigma} c_{\mu\sigma}^\dagger c_{\nu\sigma} + U \sum_{\mu} n_{\mu\uparrow} n_{\mu\downarrow} \\ & + \sum_{mm'\sigma} \epsilon_{mm'\sigma}^\alpha a_{m'\sigma}^\dagger a_{m\sigma}^\alpha + \sum_{m\mu\sigma} V_{m\mu\sigma}^\alpha a_{m\sigma}^\dagger c_{\mu\sigma} + \text{h.c.} + \\ & + \sum_{\alpha} \Delta^\alpha (a_{1\uparrow}^\alpha a_{2\downarrow}^\alpha - a_{2\uparrow}^\alpha a_{3\downarrow}^\alpha + a_{3\uparrow}^\alpha a_{4\downarrow}^\alpha - a_{4\uparrow}^\alpha a_{1\downarrow}^\alpha) \end{aligned}$$

$$+ a_{2\uparrow}^\alpha a_{1\downarrow}^\alpha - a_{3\uparrow}^\alpha a_{2\downarrow}^\alpha + a_{4\uparrow}^\alpha a_{3\downarrow}^\alpha - a_{1\uparrow}^\alpha a_{4\downarrow}^\alpha) + \text{h.c.} \quad (\text{B2})$$

The energy levels in the bath are grouped into multiples of the cluster size ($N_c = 4$) with the labels $m = 1, \dots, N_c$ and $\alpha = 1, 2$ such that we have 8 bath energy levels $\epsilon_{m\sigma}^\alpha$ coupled to the cluster via the hybridization matrix $V_{m\mu\sigma}^\alpha$. Using lattice symmetries we take $V_{m\mu\sigma}^\alpha \equiv V^\alpha \delta_{m\mu}$ and $\epsilon_{m\sigma}^\alpha \equiv \epsilon^\alpha$. Δ^α represents the amplitude of superconducting correlations in the bath. No static mean-field order parameter acts directly on the cluster sites^{28,114}. ϵ^α , V^α and Δ^α are determined by imposing the self-consistency condition in eq. 4 using a conjugate gradient minimization algorithm with a distance function that emphasizes the lowest frequencies of the Weiss field⁴² (see eq. 12). The reduced form eq. B2 is in fact a sub-case of the more general Hamiltonian eq. B1, and a canonical transformation connects eq. B2 to eq. B1. In order to see this, it is most convenient to express \mathcal{H} in a Nambu's form, introducing cluster-plaquette spinors:

$$\begin{aligned} \Psi_c^\dagger & \equiv (c_{1\uparrow}^\dagger, \dots, c_{4\uparrow}^\dagger, c_{1\downarrow}, \dots, c_{4\downarrow}) \\ \Phi_a^\dagger & \equiv (a_{1\uparrow}^\dagger, \dots, a_{4\uparrow}^\dagger, a_{1\downarrow}, \dots, a_{4\downarrow}) \quad (\text{B3}) \end{aligned}$$

and recast the Hamiltonian:

$$\begin{aligned} \mathcal{H}_{\text{imp}} = & \Psi^\dagger \mathbf{E} \Psi + U \sum_{\mu} n_{\mu\uparrow} n_{\mu\downarrow} + \\ & + \sum_{\alpha} \Phi_a^\dagger \mathbf{E}_B^\alpha \Phi_a + \Phi_a^\dagger \mathbf{V}_\alpha \Psi + \Psi^\dagger \mathbf{V}_\alpha^\dagger \Phi_a \quad (\text{B4}) \end{aligned}$$

where the Hamiltonian coupling constants are expressed by 8X8 matrices (leaving for convenience's sake the multi-bath index α implicit):

$$\mathbf{E} = \begin{pmatrix} E_{\mu,\nu,\uparrow}(4X4) & 0 \\ 0 & E_{\mu,\nu,\downarrow}(4X4) \end{pmatrix}$$

$$\mathbf{E}_B = \begin{pmatrix} \mathbf{E}_{B\uparrow}(4X4) & \mathbf{E}_B^S(4X4) \\ \mathbf{E}_B^{S\dagger}(4X4) & -\mathbf{E}_{B\downarrow}(4X4) \end{pmatrix}$$

and

$$\mathbf{V} = \begin{pmatrix} \mathbf{V}_\uparrow(4X4) & \mathbf{V}_\uparrow^S(4X4) \\ -\mathbf{V}_\uparrow^{S\dagger}(4X4) & -\mathbf{V}_\downarrow(4X4) \end{pmatrix}$$

In the more general case $\mathcal{H}_{\text{imp}}^{\text{B1}}$, the bath matrix is diagonal, so that $\mathbf{E}_{B\sigma}^{\text{kk}'} = \delta_{kk'} \epsilon_{k\sigma}$, and $\mathbf{E}_B^S = 0$. \mathbf{V}_σ and \mathbf{V}_σ^S have generally non-zero elements. In the reduced parameterization case instead (eq. B2), the bath matrix is not diagonal but chosen to mimic a cluster-plaquette, by introducing in each multi-bath α the same bath-energy $\epsilon_{\alpha\sigma}$ on every bath-site, a next-neighbor hopping t_b^α and a nearest next-neighbor hopping $t_b'^\alpha$:

$$\mathbf{E}_{B\sigma}^{\text{B2}} = \begin{pmatrix} \epsilon_{\alpha\sigma} & t_b^\alpha & t_b'^\alpha & t_b^\alpha \\ t_b^\alpha & \epsilon_{\alpha\sigma} & t_b^\alpha & t_b'^\alpha \\ t_b'^\alpha & t_b^\alpha & \epsilon_{\alpha\sigma} & t_b^\alpha \\ t_b^\alpha & t_b'^\alpha & t_b^\alpha & \epsilon_{\alpha\sigma} \end{pmatrix}$$

Moreover superconductive d-wave pairing terms Δ_α appear in the bath:

$$\mathbf{E}_B^{\mathbf{S}_\alpha \mathbf{B}2} = \begin{pmatrix} 0 & \Delta_\alpha & 0 & -\Delta_\alpha \\ \Delta_\alpha & 0 & -\Delta_\alpha & 0 \\ 0 & -\Delta_\alpha & 0 & \Delta_\alpha \\ -\Delta_\alpha & 0 & \Delta_\alpha & 0 \end{pmatrix}$$

while the hybridization between the cluster and the bath is only normal $\mathbf{V}_\sigma^S = 0$ and simplified by connecting each site of the cluster μ with only one site k_μ^α of the multi-bath α with the same coupling constant $V_{\sigma\alpha}$:

$$\mathbf{V}_{\sigma\alpha}^{\mathbf{B}2} = \begin{pmatrix} V_{\sigma\alpha} & 0 & 0 & 0 \\ 0 & V_{\sigma\alpha} & 0 & 0 \\ 0 & 0 & V_{\sigma\alpha} & 0 \\ 0 & 0 & 0 & V_{\sigma\alpha} \end{pmatrix}$$

To connect the reduced parameterization eq. B2 to the general eq. B1 it is sufficient to diagonalize the hermitian bath-matrix \mathbf{E}_B^α via a unitary transformation⁴³:

$$\mathbf{E}_B^\alpha \mathbf{B}1 = \mathbf{S}_\alpha^\dagger \mathbf{E}_B^\alpha \mathbf{B}2 \mathbf{S}_\alpha \quad (\text{B5})$$

and $\mathbf{S}_\alpha^\dagger \mathbf{S}_\alpha = \mathbf{1}$. This is in fact the requirement needed to have a canonical transformation which preserves the fermionic commutation-relations. In fact if we apply the transformation to the vectors:

$$\begin{cases} \Phi_\alpha^{\mathbf{B}2} = \mathbf{S}_\alpha \Phi_\alpha^{\mathbf{B}1} \\ \Phi_\alpha^{\dagger \mathbf{B}2} = \Phi_\alpha^{\dagger \mathbf{B}1} \mathbf{S}_\alpha^\dagger \end{cases} \quad (\text{B6})$$

and we have

$$\left\{ \Phi_\alpha^{\mathbf{B}2}, \Phi_\alpha^{\dagger \mathbf{B}2} \right\} = \mathbf{1} \quad (\text{B7})$$

it is

$$\left\{ \Phi_{q\alpha}^{\mathbf{B}2}, \Phi_{q\alpha}^{\dagger \mathbf{B}2} \right\} = \quad (\text{B8})$$

$$\sum_{kk'} S_{qk}^\dagger S_{k'q} \left\{ \Phi_{k\alpha}^{\mathbf{B}2}, \Phi_{k'\alpha}^{\dagger \mathbf{B}2} \right\} = (\text{B9})$$

$$\sum_k S_{qk}^\dagger S_{kq} = 1 \quad (\text{B10})$$

Finally \mathbf{V}_α is subjected to the same transformation:

$$\mathbf{V}_\alpha^{\mathbf{B}1} = \mathbf{S}_\alpha^\dagger \mathbf{V}_\alpha^{\mathbf{B}2} \quad (\text{B11})$$

ACKNOWLEDGMENTS

We thank G. Kotliar, who inspired many of the ideas in this work. We thank O. Parcollet and K. Haule for sharing their QMC results. We also acknowledge the fruitful discussion with A. Georges, M. Capone and T. D. Stanescu. We enjoyed the exchange of ideas and the hospitality of A. Sacuto and the SQUAP group at the University of Paris 7. We acknowledge A.-M. S. Tremblay, S. S. Kancharla, B. Kyung, I. Paul, A. Cano, E. Kats and P. Nozières for their useful comments.

-
- ¹ J. G. Bednorz and K. A. Muller, Z. Phys. B **64** 189 (1986).
 - ² Y. Kamihara, T. Watanabe, M. Hirano and H. Hosono, J. Am. Chem. Soc. **130** 3296 (2008).
 - ³ C. Day, Physics Today **61** 11-12 (2008).
 - ⁴ P. W. Anderson, Science **235** 1196 (1987).
 - ⁵ A. Georges, G. Kotliar, W. Krauth and M. J. Rozenberg, Rev. Mod. Phys. **68** 13 (1996).
 - ⁶ N. E. Zein, S. Y. Savrasov and G. Kotliar, Phys. Rev. Lett. **96** 226403 (2006).
 - ⁷ "Ruthenate and Rutheno-Cuprate Materials: Unconventional Superconductivity, Magnetism and Quantum Phase Transitions" A. Lichtenstein and A. Liebsch, Springer-Verlag, Berlin, Germany (2002).
 - ⁸ K. Held, A. K. McMahan and R. T. Scalettar, Phys. Rev. Lett. **87** 276404 (2001).
 - ⁹ K. Haule, V. Oudovenko, S. Y. Savrasov and G. Kotliar, Phys. Rev. Lett. **94** 036401 (2005).
 - ¹⁰ S. Savrasov, G. Kotliar and E. Abrahams, Nature **410** 793 (2001).
 - ¹¹ G. Kotliar, S. Savrasov, K. Haule, V. Oudovenko, O. Parcollet and C. Marianetti, Rev. Mod. Phys. **78** 000865 (2006).
 - ¹² A. Damascelli, Z. X. Shen and Z. Hussain, Rev. Mod. Phys. **75** 473 (2003).
 - ¹³ "Physics of Superconductors II" J. C. Campuzano, M. R. Norman and M. Randeria, K. H. Bennemann and J. B.

- Ketterson (2004) 167-273.
- ¹⁴ Th. Maier, M. Jarrell, Th. Pruschke and M. Hettler, Rev. Mod. Phys. **77** 1027-1080 (2005).
- ¹⁵ G. Biroli, O. Parcollet and G. Kotliar, Phys. Rev. B **69** 205108 (2004).
- ¹⁶ A. I. Lichtenstein and M. I. Katsnelson, Phys. Rev. B **62** R9283 (2000).
- ¹⁷ Th. Maier, M. Jarrell, Th. Pruschke and J. Keller, Phys. Rev. Lett. **85** 1524 (2000).
- ¹⁸ A.-M. S. Tremblay, B. Kyung and D. Sénéchal, Low Temperature Physics **32** 424 (2006).
- ¹⁹ G. Kotliar, S. Y. Savrasov, G. Palsson and G. Biroli, Phys. Rev. Lett. **87** 186401 (2001).
- ²⁰ R. M. Fye and J. E. Hirsch, Phys. Rev. Lett. **56** 2521 (1986).
- ²¹ R. M. Fye and J. E. Hirsch, Phys. Rev. B **40** 47804796 (1989).
- ²² T. A. Maier, M. Jarrell, T. C. Schulthess, P. R. C. Kent and J. B. White, Phys. Rev. Lett. **95** 237001 (2005).
- ²³ T. A. Maier, M. Jarrell and D. J. Scalapino, Phys. Rev. Lett. **96** 047005 (2006).
- ²⁴ D. Sénéchal and A.-M. S. Tremblay, Phys. Rev. Lett. **92** 126401 (2004).
- ²⁵ O. Parcollet, G. Biroli and G. Kotliar, Phys. Rev. Lett. **92** 226402 (2004).
- ²⁶ M. Civelli, M. Capone, S. S. Kancharla, O. Parcollet and G. Kotliar, Phys. Rev. Lett. **95** 106402 (2005).

- ²⁷ B. Kyung, S. S. Kancharla, D. Sénéchal, A.-M. S. Tremblay, M. Civelli and G. Kotliar, Phys. Rev. B **73** 165114 (2006).
- ²⁸ S. S. Kancharla, B. Kyung, D. Sénéchal, M. Civelli, M. Capone, G. Kotliar and A.-M. S. Tremblay, Phys. Rev. B **77** 184516 (2008).
- ²⁹ M. Capone and G. Kotliar, Phys. Rev. B **74** 054513 (2006).
- ³⁰ M. Aichhorn, E. Arrigoni, M. Potthoff and W. Hanke, Phys. Rev. B **74** 235117 (2006).
- ³¹ M. Aichhorn, E. Arrigoni, M. Potthoff and W. Hanke, Phys. Rev. B **74** 024508 (2006).
- ³² D. Sénéchal, P.-L. Lavertu, M.-A. Marois and A.-M. S. Tremblay, Phys. Rev. Lett. **94** 156404 (2005).
- ³³ C. Huscroft, M. Jarrell, Th. Maier, S. Moukouri and A. N. Tahvildarzadeh, Phys. Rev. Lett. **86** 139 (2001).
- ³⁴ T. D. Stanescu and P. Phillips, Phys. Rev. Lett. **91** 017002 (2003).
- ³⁵ F. H. L. Essler and A. M. Tsvelik, Phys. Rev. B **65** 115117 (2002).
- ³⁶ T. D. Stanescu and G. Kotliar, Phys. Rev. B **74** 125110 (2006).
- ³⁷ C. Berthod, T. Giamarchi, S. Biermann and A. Georges, Phys. Rev. Lett. **97** 136401 (2006).
- ³⁸ T. D. Stanescu, P. W. Phillips and T.-P. Choy, Phys. Rev. B **75** 104503 (2007).
- ³⁹ K. Haule and G. Kotliar, Phys. Rev. B **76** 092503 (2007).
- ⁴⁰ M. Caffarel and W. Krauth, Phys. Rev. Lett. **72** 1545 (1994).
- ⁴¹ K. Haule and G. Kotliar, Phys. Rev. B **76** 104509 (2007).
- ⁴² M. Capone, M. Civelli, S. S. Kancharla, C. Castellani and G. Kotliar, Phys. Rev. B **69** 195105 (2004).
- ⁴³ M. Civelli, PhD Thesis, arXiv.org:0710.2802 (2007).
- ⁴⁴ M. Civelli, M. Capone, A. Georges, K. Haule, O. Parcollet, T. D. Stanescu and G. Kotliar, Phys. Rev. Lett. **100** 046402 (2008).
- ⁴⁵ P. A. Lee, N. Nagaosa and X.-G. Wen, Rev. Mod. Phys. **78** 17 (2006).
- ⁴⁶ G. Biroli and G. Kotliar, Phys. Rev. B **65** 155112 (2002).
- ⁴⁷ T. D. Stanescu, M. Civelli, K. Haule and G. Kotliar, An. of Phys. **321** 1682 (2006).
- ⁴⁸ A. Perali, M. Sindel and G. Kotliar, Eur. Phys. J. B **24** 487 (2002).
- ⁴⁹ J. Hubbard, Proc. Roy. Soc. A **276** 238 (1963).
- ⁵⁰ C. J. Bolech, S. S. Kancharla and G. Kotliar, Phys. Rev. B **67** 075110 (2003).
- ⁵¹ K. Haule, Phys. Rev. B **75** 155113 (2007).
- ⁵² G. Kotliar and J. Liu, Phys. Rev. B **38** R5142 (1988).
- ⁵³ K. McElroy, D.-H. Lee, J. E. Hoffman, K. M. Lang, J. Lee, E. W. Hudson, H. Eisaki, S. Uchida and J. C. Davis, Phys. Rev. Lett. **94** 197005 (2005).
- ⁵⁴ M. Le Tacon, A. Sacuto, A. Georges, G. Kotliar, Y. Gallais, D. Colson and A. Forget, Natur. Phys. **2** 537 (2006).
- ⁵⁵ K. Tanaka, W. S. Lee, D. H. Lu, A. Fujimori, T. Fujii, Risdiana, I. Terasaki, D. J. Scalapino, T. P. Devereaux, Z. Hussain and Z.-X. Shen, Science **314** 1910 (2006).
- ⁵⁶ A. Cho, Science **314** 1072 (2006).
- ⁵⁷ A. J. Millis, Science **314** 1888 (2006).
- ⁵⁸ G. Deutscher, Nature **397** 410 (1999).
- ⁵⁹ S. Huefner, M. A. Hossain, A. Damascelli and G. A. Sawatzky, Rep. Prog. Phys. **71** 062501 (2008).
- ⁶⁰ T. Kondo, T. Takeuchi, A. Kaminski, S. Tsuda and S. Shin, Phys. Rev. Lett. **98** 267004 (2007).
- ⁶¹ K. K. Gomes, A. N. Pasupathy, A. Pushp, S. Ono, Y. Ando and A. Yazdani, Nature **447** 569 (2007).
- ⁶² L. B. Ioffe and A. J. Millis, Phys. Rev. B **58** 11631 (1998).
- ⁶³ A. T. Zheleznyak, V. M. Yakovenko, H. D. Drew and I. I. Mazin, Phys. Rev. B **57** 3089 (1998).
- ⁶⁴ R. Hlubina and T. M. Rice, Phys. Rev. B **51** 9253 (1995).
- ⁶⁵ O. Parcollet, private communication.
- ⁶⁶ H. Matsui, T. Sato, T. Takahashi, S.-C. Wang, H.-B. Yang, H. Ding, T. Fujii, T. Watanabe and A. Matsuda, Phys. Rev. Lett. **90** 217002 (2003).
- ⁶⁷ J. M. Luttinger, Phys. Rev. **119** 1153 (1960).
- ⁶⁸ L. De Leo, M. Civelli and G. Kotliar, arXiv.org:0804.3314 (2008).
- ⁶⁹ M. Ferrero, F. Becca, M. Fabrizio and M. Capone, Phys. Rev. B **72** 205126 (2005).
- ⁷⁰ L. de' Medici, A. Georges and S. Biermann, Phys. Rev. B **72** 205124 (2005).
- ⁷¹ X. J. Zhou, T. Yoshida, A. Lanzara, P. V. Bogdanov, S. A. Kellar, K. M. Shen, W. L. Yang, F. Ronning, T. Sasagawa, T. Kakeshita, T. Noda, H. Eisaki, S. Uchida, C. T. Lin, F. Zhou, J. W. Xiong, W. X. Ti, Z. X. Zhao, A. Fujimori, Z. Hussain and Z.-X. Shen, Nature **423** 398 (2003).
- ⁷² D. A. Bonn, Czech. J. Phys. **46** 3195 (1996).
- ⁷³ C. Panagopoulos and T. Xiang, Phys. Rev. Lett. **81** 2336 (1998).
- ⁷⁴ B. Kyung and A.-M. S. Tremblay, cond-mat/0204500 (2002).
- ⁷⁵ Kai-Yu Yang, T. M. Rice and Fu-Chun Zhang, Phys. Rev. B **73** 174501 (2006).
- ⁷⁶ B. Valenzuela and E. Bascones, Phys. Rev. Lett. **98** 227002 (2007).
- ⁷⁷ M. Aichhorn, E. Arrigoni, Z. B. Huang and W. Hanke, Phys. Rev. Lett. **99** 257002 (2007).
- ⁷⁸ W. Guyard, A. Sacuto, M. Cazayous, Y. Gallais, M. Le Tacon, D. Colson and A. Forget, arXiv.org:0802.3166 (2008).
- ⁷⁹ N. Doiron-Leyraud, C. Proust, D. LeBoeuf, J. Levallois, J.-B. Bonnemaison, R. Liang, D.A. Bonn, W.N. Hardy and L. Taillefer, Nature **447** 565 (2007).
- ⁸⁰ R. Daou, D. LeBoeuf, N. Doiron-Leyraud, S. Y. Li, F. Laliberte, O. Cyr-Choiniere, Y. J. Jo, L. Balicas, J. -Q. Yan, J. -S. Zhou, J. B. Goodenough and L. Taillefer, arXiv.org:0806.2881 (2008).
- ⁸¹ F. F. Balakirev, J. B. Betts, A. Migliori, I. Tsukada, Yoichi Ando and G. S. Boebinger, arXiv.org:0710.4612 (2007).
- ⁸² F. F. Balakirev, J. B. Betts, A. Migliori, S. Ono, Yoichi Ando and G. S. Boebinger, Nature **424** 912 (2003).
- ⁸³ N. M. Plakida and V. S. Oudovenko, JETP **104** 230 (2007).
- ⁸⁴ A. Avella and F. Mancini, Phys. Rev. B **75** 134518 (2007).
- ⁸⁵ I. E. Dzyaloshinskii, Phys. Rev. B **68** 085113 (2003).
- ⁸⁶ F. H. L. Essler and A. M. Tsvelik, Phys. Rev. Lett. **90** 126401 (2003).
- ⁸⁷ R. M. Konik, T. M. Rice and A. M. Tsvelik, arXiv.org:cond-mat/0511268 (2005).
- ⁸⁸ A. Rosch, Eur. Phys. Jour. B **59** 495 (2007).
- ⁸⁹ A. Lanzara, P. V. Bogdanov, X. J. Zhou, S. A. Kellar, D. L. Feng, E. D. Lu, T. Yoshida, H. Eisaki, A. Fujimori, K. Kishio, J.-I. Shimoyama, T. Noda, S. Uchida, Z. Hussain and Z.-X. Shen, Nature **412** 510 (2001).
- ⁹⁰ Z.-X. Shen, A. Lanzara, S. Ishihara and N. Nagaosa, Phi-

- los. Mag. B **82** 1349 (2002).
- ⁹¹ H. He, Y. Sidis, P. Bourges, G. D. Gu, A. Ivanov, N. Koshizuka, B. Liang, C. T. Lin, L. P. Regnault, E. Schoenher and B. Keimer, Phys. Rev. Lett. **86** 1610 (2001).
 - ⁹² J. Hwang, T. Timusk and G. D. Gu, Nature **427** 714 (2004).
 - ⁹³ T. Cuk, F. Baumberger, D. H. Lu, N. Ingle, X. J. Zhou, H. Eisaki, N. Kaneko, Z. Hussain, T. P. Devereaux, N. Nagaosa and Z.-X. Shen, Phys. Rev. Lett. **94** 117003 (2004).
 - ⁹⁴ A. Kaminski, M. Randeira, J. C. Campuzano, M. R. Norman, H. Fretwell, J. Mesot, T. Sato, T. Takahashi and K. Kadowaki, Phys. Rev. Lett. **86** 1070 (2001).
 - ⁹⁵ K. Byczuk, M. Kollar, K. Held, Y. -F. Yang, I. A. Nekrasov, Th. Pruschke and D. Vollhardt, Nature Physics **3** 168 (2007).
 - ⁹⁶ S. Chakraborty, D. Galanakis and P. Phillips, arXiv.org:0712.2838 (2007).
 - ⁹⁷ J. Graf, G.-H. Gweon, K. McElroy, S. Y. Zhou, C. Jozwiak, E. Rotenberg, A. Bill, T. Sasagawa, H. Eisaki, S. Uchida, H. Takagi, D.-H. Lee and A. Lanzara, Phys. Rev. Lett. **98** 067004 (2007).
 - ⁹⁸ T. Valla, T. E. Kidd, Z.-H. Pan, A. V. Fedorov, W.-G. Yin, G. D. Gu and P. D. Johnson, Phys. Rev. Lett. **98** 167003 (2007).
 - ⁹⁹ M. Z. Cieplak, A. Abal'oshev, I. Zaytseva, M. Berkowski, S. Guha and Q. Wu, Acta Physica Polonica A **109** 573 (2006).
 - ¹⁰⁰ G. Baskaran, Z. Zou and P. W. Anderson, Solid State Com. **63** 973 (1987).
 - ¹⁰¹ A. E. Ruckenstein, P. J. Hirschfeld and J. Appel, Phys. Rev. B **36** 857 (1987).
 - ¹⁰² T. D. Stanescu and G. Kotliar, Phys. Rev. B **70** 205112 (2004).
 - ¹⁰³ M. Shi, J. Chang, S. Pailh  s, M. R. Norman, J. C. Campuzano, M. Mansson, T. Claesson, O. Tjernberg, A. Bendounan, L. Patthey, N. Momono, M. Oda, M. Ido, C. Mudry and J. Mesot, Phys. Rev. Lett. **101** 047002 (2007).
 - ¹⁰⁴ A. Kanigel, U. Chatterjee, M. Randeria, M. R. Norman, S. Souma, M. Shi, Z. Z. Li, H. Raffy and J. C. Campuzano, Phys. Rev. Lett. **99** 157001 (2007).
 - ¹⁰⁵ A. Kanigel, U. Chatterjee, M. Randeria, M. R. Norman, G. Koren, K. Kadowaki and J. C. Campuzano, arXiv:0803.3052v1 (2008).
 - ¹⁰⁶ S. Sachdev and J. Ye, Phys. Rev. Lett. **69** 2411 (1992).
 - ¹⁰⁷ A. Perali, C. Castellani, C. Di Castro and M. Grilli, Phys. Rev. B **54** 16216–16225 (1996).
 - ¹⁰⁸ S. A. Kivelson, E. Fradkin and V. J. Emery, Nature **393** 550 (1998).
 - ¹⁰⁹ C. M. Varma, Phys. Rev. Lett. **83** 3538 (1999).
 - ¹¹⁰ Yoichi Ando, G. S. Boebinger, A. Passner, T. Kimura and K. Kishio, Phys. Rev. Lett. **75** 4662–4665 (1995).
 - ¹¹¹ G. S. Boebinger, Yoichi Ando, A. Passner, T. Kimura, M. Okuya, J. Shimoyama, K. Kishio, K. Tamasaku, N. Ichikawa and S. Uchida, Phys. Rev. Lett. **77** 5417–5420 (1996).
 - ¹¹² M. Ferrero, P. S. Cornaglia, L. De Leo, O. Parcollet, G. Kotliar and A. Georges, arXiv.org:0806.4383 (2008).
 - ¹¹³ R. Haydock, V. Heine and M. J. Kelly, J. Phys. C **8** 2591 (1975).
 - ¹¹⁴ D. Poilblanc and D. J. Scalapino, Phys. Rev. B **66** 052513 (2002).